

*Observation, Simulation, and Evaluation
of Snow Dynamics in the Transitional Snow Zone*

Nicholas E. Wayand

A dissertation
submitted in partial fulfillment of the
requirements for the degree of

Doctor of Philosophy

University of Washington

2016

Reading Committee:

Jessica D. Lundquist (Chair)

Bart Nijssen

Martyn P. Clark

Program Authorized to Offer Degree:

Department of Civil and Environmental Engineering

©Copyright 2016

Nicholas E. Wayand

University of Washington

Abstract

Observation, Simulation, and Evaluation of Snow Dynamics in the Transitional Snow Zone

Nicholas E. Wayand

Chair of the Supervisory Committee:

Associate Professor Jessica D. Lundquist

Department of Civil and Environmental Engineering

The frequent mid-winter accumulation and ablation cycles of snowpack within the rain-snow transitional zone play an important role for the maritime basins along the western U.S. mountain ranges. Representation of transitional snowpack within hydrological models has remained a challenge, largely because surface and meteorological conditions frequently remain near the freezing point, which allows large errors in modeled accumulation or ablation to result from small forcing or structural errors. This research aims to improve model representation of accumulation and ablation processes by utilizing new observations within the transitional snow zone combined with novel methods of model evaluation.

The importance of mid-winter snowmelt during historical flooding events was assessed over three maritime basins in the western US. A physically-based snow model was coupled with an idealized basin representation to quantify how the characteristics of each basin combined with storm strength to control the distribution of snowmelt over a basin. Snowmelt contributions to total basin runoff ranged from 7-29% during historic flooding events between 1980 and 2008.

However, poor meteorological forcing data were found to be a major limitation in model evaluation.

In response to this limitation, a historical snow study site at Snoqualmie Pass within the Washington Cascades was updated in October 2012 with meteorological, soil, and snow observations to provide an ideal site for model evaluation within the transitional snow zone where existing observations are extremely sparse. The data set includes complete meteorological forcing required for snow models: air temperature, total precipitation, wind speed, specific humidity, air pressure, short- and longwave irradiance. Historical (1980-2015) observations include snow board new snow accumulation, multiple measurements of total snow depth, and manual snow pits, while more recent years (2012-2015) include sub-daily surface temperature, snowpack drainage, soil moisture and temperature profiles, and eddy co-variance derived turbulent heat flux; in short an ideal site to test different hypothesis about snow processes.

This unique observational data set was used to illustrate how a novel process-based approach can diagnose model errors in snow accumulation processes (precipitation partitioning, new snow density, and compaction). The main source of model error on each day was identified by comparing observed snow board measurements to a “modeled snow board.” Results found that even after in-situ calibration, new snow density errors were the most common, occurring 53% of available days, followed by precipitation partition errors (43%) and compaction errors (18%). Daily errors canceled out on annual time scales during all years except the anomalously warm winter of 2014-2015.

The partitioning of precipitation into rain or snow during water year 2015 was further examined by evaluating surface-based and mesoscale-model-based predictions. Observations of

precipitation phase from a disdrometer at Snoqualmie Pass and nearby snow depth sensors were used to evaluate both methods. With calibration, the skill of surface-based methods was greatly improved by using air temperature from a nearby higher-elevation station, which was less impacted by surface inversions at the pass. Without any form of a prior calibration, we found a hybrid method that combines surface-based predictions with output from the Weather Research and Forecasting mesoscale model, to have comparable skill to calibrated surface-based methods. These results suggest that phase prediction in mountain passes can be improved by incorporating observations or models of the atmosphere aloft.

Dedication

To my wife Vidya and our daughter Alarie

“It is a fortunate chance that the triple point of H₂O is common on Earth, because it has resulted in a beautifully complex Cryosphere”

Acknowledgements

I would like to thank my academic advisor, Jessica Lundquist, for providing excellent mentorship over the past 6 years and always encouraging me to “do first the research that is most interesting.” Jessica has always led by example, showing how curiosity about the natural world can be combined with the scientific method to make research fun and rewarding. I am greatly indebted to her for her patience through the years as my advisor.

I also thank my dissertation committee members, Martyn Clark, Bart Nijssen, and Chris Bretherton for their time spent discussing research, fielding my modeling issues and providing feedback that greatly improved this dissertation. In addition, I would like to thank the many professors at UW that have provided guidance over the years, including Justin Minder, Steve Burges, LuAnne Thompson, Faisal Hossain, and Alan Hamlet.

Outside UW, I was lucky to meet and work with an interesting range of researchers. The Valle scholarship allowed me to visit the Bjerknes Centre for Climate Research in Bergen, Norway, where I was able to work with Idar Barstad on a linear precipitation model. Nick Pepin graciously let me visit their subarctic research station in northern Finland. The National Center for Atmospheric Research Advanced Study Program allowed me to visit Boulder, CO to work with Martyn Clark to aid the development of a hydrological model that was used in this research. Finally, I thank John Stimberis of the Northwest Avalanche Center for sharing Snoqualmie Pass data and for time spent discussing snow in the mountains.

Financial support for my first quarter of graduate education was provided by the University of Washington’s Graduate Student Panel on Climate Change Fellowship. I was also supported by the University of Washington’s Valle scholarship during my first year. Finally, the remainder of my research was funded by a National Science Foundation Grant (EAR-704 1215771) and a NASA Earth and Space Science Fellowship (NNX12AN53H). I am extremely thankful to all of these contributors for making my graduate education possible.

My colleagues in the Mountain Hydrology Research Group have played a large role in shaping my graduate education and providing continuous feedback to this dissertation. I would like to thank Mark Raleigh, Courtney Moore, Pablo Carrasco, Nicoleta Cristea, and Jenna Forsyth for their patience answering my never-ending questions during my first year. Adam Massmann, Colin Butler, and Eric Keenan for their field work that made this research possible. And finally, I am extremely thankful for the lively research discussion over daily coffee breaks with Susan Dickerson-Lange, Brian Henn, Karl Lapo, and Ryan Currier.

I would not have made it this far in life without my family. I am exceptionally grateful to my parents, Dona and John, for their continuous love and support that has allowed me to focus on research; and to my wife Vidya for listening to every presentation 10 times and pushing me to go further each time.

At the time of writing, two of the following chapters have been published in a peer-reviewed journal, and I would like to acknowledge John Wiley and Sons, publisher of *Water Resources Research*, for granting permission to reproduce the article in this dissertation. The citations are:

Chapter 2:

Wayand, N. E., J. D. Lundquist, and M. P. Clark (2015), Modeling the influence of hypsometry, vegetation, and storm energy on snowmelt contributions to basins during rain-on-snow floods, *Water Resour. Res.*, 51, 8551–8569, doi:10.1002/2014WR016576.

Chapter 3:

Wayand, N. E., A. Massmann, C. Butler, E. Keenan, and J. D. Lundquist (2015), A Meteorological and Snow observational data set from Snoqualmie Pass (921 m), Washington Cascades, U.S., *Water Resour. Res.*, doi:10.1002/2015WR017773.

Table of Contents

Chapter 1. Introduction	18
Chapter 2. Modeling the influence of hypsometry, vegetation, and storm energy on snowmelt contributions to basins during rain-on-snow floods.....	20
2.1 Introduction	21
2.2 Background	23
2.3 Data	25
2.3.1 Intensive observational study sites	26
2.3.2 Study basins with limited observations	27
2.4 Methods	28
2.4.1. Snow Model.....	29
2.4.2. Forcing data	30
2.4.3. Selection of rain-on-snow events	32
2.4.4. Evaluation of point DHSVM simulations of snowmelt	33
2.4.5. Idealized representation of basin snowmelt	34
2.5 Results	35
2.5.1. Evaluation of DHSVM at point snow study sites (Question 1)	35
2.5.2. Quantifying Basin Snowmelt during rain-on-snow events within an idealized framework (Question 2)	36
2.5.3 Basin and Storm controls on snowmelt (Question 3).....	37
2.6 Discussion	39
2.6.1. Uncertainties in modeling snowmelt during ROS events.....	39
2.6.2. Importance of snowmelt volume towards flooding.....	42
2.7 Conclusions	45
2.8 Tables	45
2.9. Figures	50
2.10. Appendix A	56
2.11. Appendix B	58
2.12. Appendix C	59
Chapter 3. A Meteorological and Snow observational data set from Snoqualmie Pass (921 m), Washington Cascades, U.S.	61
3.1. Introduction	62
3.2. Snoqualmie Pass site description	63
3.3. Data Descriptions	64
3.3.1. Meteorological measurements.....	65
3.3.2. Snow and soil measurements.....	68
3.4. Quality Control.....	72
3.5. Meteorological forcing data sets	73
3.5.1. Recent: 10/1/2012 – 5/11/2015	74
3.5.2. Historic: 10/1/1989 – 9/30/2012.....	75
3.6. Snow and soil measurements	76
3.7. Conclusions	76
3.8. Tables	77
3.9. Figures	85

Chapter 4. Diagnosing Snow Accumulation Errors in a Rain-Snow Transitional Environment with Snow Board Observations	89
4.1 Introduction	89
4.2 Background	91
4.2.1. Sources of snow model uncertainty.....	91
4.2.2. Process observations.....	91
4.2.3. Isolated processes	92
4.3. Study Site and Data	95
4.3.1. Snow observations.....	95
4.3.2. Meteorological forcing data	97
4.4. Methods.....	97
4.4.1. Snow model (SUMMA)	97
4.4.2. Simulating snow board measurements with SUMMA.....	98
4.4.3. Lumped calibration method.....	98
4.4.4. Process-based calibration	99
4.4.5. Diagnosing daily snow accumulation errors	102
4.4.6. Case study of water year 2015.....	102
4.5. Results	103
4.5.1. Lumped method results	103
4.5.2. Process-based method results	103
4.5.3. Bulk snow depth.....	105
4.5.4. Diagnosis of bulk snow accumulation errors	106
4.6. Discussion	107
4.6.1. Robustness of simulations of bulk snow accumulation.....	107
4.6.2. Uncertainty in diagnosis of daily model error source	108
4.6.3. Applicability of process-based method	110
4.7. Summary	110
4.8. Tables	111
4.9. Figures	116
Chapter 5. Impacts of Cold Air Intrusions on Snoqualmie Pass Snow	126
5.1. Introduction	126
5.2. Study domain and data	129
5.2.1. Snoqualmie Pass.....	129
5.2.2. Observations of phase at surface	130
5.2.2. Meteorological Observations.....	130
5.3. Methods.....	131
5.3.1. Observations of precipitation phase	131
5.3.2. Precipitation phase methods.....	132
5.3.3. Storm selection and case studies	135
5.4. Results	135
5.4.1. Phase predictability using near-surface T_{air}	135
5.4.2. Evaluation of phase prediction methods at SNQ station.....	136
5.4.3. Case study, 4-5 January, 2015.....	137
5.5. Discussion	139
5.5.1. Recommendation for best rain-snow partitioning method at Snoqualmie Pass	139

5.5.2. Frequency of inversions during precipitation at SNQ.....	140
5.6. Conclusion.....	141
5.7. Tables	142
5.8. Figures	142
5.9. Appendix A	153
References.....	159
Curriculum Vitae	171

List of Figures

- Figure 2-1. Conceptual illustration of the two fundamental controls on snowmelt during a rain-on-snow event: 1) the initial SWE and 2) the energy available for melt (in terms of equivalent melt). The impact of two different initial SWE distributions (a) prior to a ROS storm with, the same available energy for melt (b), and the resulting snowmelt given unit-area basin (c) or realistic basin hypsometry (d). Given the same initial SWE distribution (e), the impact of two different available energy distributions (f), and the resulting snowmelt given two different basin shapes (f and h). The take away hypothesis is that the elevations with the largest snowmelt volumes are produced where the available SWE intersects the potential melt energy and the largest area. 50
- Figure 2-2. Insert (a) shows domain of study along the Cascade and Sierra Nevada ranges. (b) Outlines of westward draining HUC-8 basins categorized by their elevation where 50% of the basin area lies. Bold outlines show selected basins (SQ, ENFF and USJ) from each category used in this study. (c) Cumulative basin area with increasing elevation as a fraction of each basin. Black circles show elevations of stations with snowpillows within each basin (Listed in Table 1). 51
- Figure 2-3. Idealized representation of study basins. Boxes indicate 100 meter elevation bins, simulated for all Forest and all Grass vegetation. Vegetation-weighted is represented as a linear combination of the model results based on observed vegetation fractions. Hypsometry is included by multiplying the model output by the area over the basin at each elevation bin to estimate the volume input. 52
- Figure 2-4. Observed and modeled (Sim 1) seasonal SWE at Col de Porte, France. 52
- Figure 2-5. (left) Observed and modeled snowmelt total during each 3-day storm. (right) Vertical bars show the observed rain fall total during each 3-day storm that resulted in flooding (filled gray) and non-flooding (filled white), for SNQ sites only (c,d,e). Storms are ranked by storm rainfall separately at (a) CDP and (b) UNF, and by the mean storm rainfall of all three Snoqualmie basin stations: ALP, OLI, and SKU, in (c,d,e). Storm total rainfall is approximated from observed precipitation minus observed snowpillow increases, which may underestimate rainfall due to retention of liquid water in the snowpack. Note: different y-axis scales for snowmelt and rainfall. Grayed box highlights the January 19 2005 storm examined in Section 2.6.2. 53
- Figure 2-6. Simulated basin-average inputs of snowmelt and rainfall during all study storms (listed in Table A1 and Table S1). 54
- Figure 2-7. (a) Simulated basin-wide snowmelt assuming all basins have unit-weighted area and have no forest. (b) Simulated storm-total snowmelt at each basin's elevational range during each storm (1 ranked by total basin-wide snowmelt total for each basin (shown in (a))). Impacts on simulated basin-wide snowmelt in (a) from inclusion of basin hypsometry (d) are shown in (c), and forest cover (f) are shown in (e). Ratios in (c,e) are defined in text. Open circles represent ROS events without observed flooding while filled circles indicate some level of flooding was

observed. Open and filled circles are offset for readability. Box plots show median, 25th and 75th percentiles, and 1.5 times the inter-quartile range. X-axis abbreviations refer to SNQ (Snoqualmie), ENFF (East North Fork Feather), and USJ (Upper San Joaquin) basins. 55

Figure 2-8. DHSVM simulation (Sim 9.1a) during the January 2005 flood of (a) hourly change in SWE, (b) hourly rainfall, and (c) basin averaged input over the SNQ basin with area- and vegetation-weighted simulations (Sim 9.1a and 9.2a). *Blue (red) triangles* pointing up (down) indicate an observed net increase (decrease) in SWE (note: triangles are placed at midnight and represent change in SWE over previous 24 hours). *Dashed and solid lines* in (a) and (b) show elevations of snowfall-level (i.e., the atmospheric rain/snow transition) and snowcover-extent (on the ground). In (a), *grey* colors show less than 0.1 mm simulated SWE change while *white* colors indicate no snow present. *Vertical red lines* show the time of peak observed stage height. 56

Figure 3-1. (a,b) The Snoqualmie (SNQ) pass snow study site located within the Washington Cascades, U.S, at 917 meters a.s.l. (+47.424883, -121.413893). (c) Airborne photo looking northwest towards the SNQ site with Interstate 90 at center. 85

Figure 3-2. Observed variables from tower A and B, located within the study site area shown in insert. *White arrows* within the insert represent approximate viewing angle of towers A and B. 86

Figure 3-3. Availability of observed forcing data during (a) historic and (b) recent periods. *Dark gray lines* show observations that passed quality control or were filled with duplicate in-situ observations, while *light gray lines* indicate missing observations that were filled from alternative sources as described in Section 3.4. *Black dashed lines* show installation of instruments. Column variables are air temperature (T), total precipitation (P), relative humidity (RH), wind speed (WS), pressure (PR), shortwave irradiance (SW), and longwave irradiance (LW). Years on y-axis refer to January 1st. 87

Figure 3-4. (a) New snow density from past 24 hour accumulation as measured by snow boards between 1974 and 2014 (N=2582 snow accumulation days) binned by daily average air temperature. Three common parameterizations of new snow density are shown for comparison. (b) Measured new SWE versus daily air temperature. Note: Some scatter in the observed new snow density may be due to compaction or melting occurring in between the time snow fell and the snow board measurement was made. 88

Figure 4-1. Example of isolating new snow accumulation processes. All fluxes into *dashed boxes* were taken directly from observations when possible. Variable abbreviations are defined in Table 1. 116

Figure 4-2. (a) Images show available measurements of new SWE, new snow depth, and bulk snow depth. *Horizontal black lines* show modeled snow layers (accumulation, compaction and merging) that are representative of observed layers shown in right image. *Note: the right image shows a snow pit for illustration only, bulk snow depth was read from off a 4 m snow stake (see Figure 2 of Wayand *et al.* 2015). (b) Example of the “modeled snowboard” simulations, which were compared to observations in (a). Note: the *red line* shows modeled snow depth at the *end* of modeled hourly time step, thus first step is non-zero. 117

Figure 4-3. Methodology for both (a) Typical and (b) Processed based methods. The typical method uses a lumped calibration approach by running all model option/parameter configurations. In contrast, the processed based method evaluates one process at a time, passing on the selected option/parameters to the next process evaluation. Selected model option/parameters are defined in Table 3..... 118

Figure 4-4. Example of model ensemble of (a) accumulated SWE, and (b) accumulated snow depth, compared to independent snow board measurements of 24 hour accumulated SWE and snow depth. Observed wet-bulb (T_{wet}) and air (T_{air}) temperatures are also shown because modeled partition depended on T_{wet} and new snow density on T_{air} 119

Figure 4-5. Modeled and observed daily accumulated new SWE (a), new snow depth (b), and compaction (c), shown for each day. *Gray circles* show all ensemble simulations. *Blue and red filled circles* show ensemble member selected from the highest KGE value. 120

Figure 4-6. Daily fraction of precipitation (a) observed and (b) modeled as ice. Observed fraction was calculated from the ratio of snow board SWE to total gauge precipitation. Modeled fraction was calculated from the ratio of simulated new SWE (restart simulations) to the observed total gauge precipitation..... 121

Figure 4-7. (a) Calibration results for each new snow density function, showing near-equal performance given the right parameter values. A KGE value of unity is best. (b) Observed newly fallen snow density compared to the daily average air temperature during water years 1980-2015. Overlaid lines, show each function in (a) with the highest KGE value (*red circles*). 122

Figure 4-8. (a) Modeled and observed bulk snow depth during the calibration period (water years 2004-2009). Vertical white periods represent missing snow stake measurements. Scatter plots of modeled and observed *total accumulated* new SWE (b), new snow (c), and compaction of old snow during accumulation days (d) for each water year. Symbol type indicates each water year while color refers to model simulations defined in legend (a)..... 123

Figure 4-9. Same as Figure 8, but for the evaluation period (water years 2010-2015). 124

Figure 4-10. Frequency of each source of model daily error (*solid bars*) out of available days where cascading errors were removed (*outline bars*), for each water year. 124

Figure 4-11. Time series of observed and modeled total snow depth for water year 2015. Colors for each day show the identification of the dominate source of model error using the process-based model configuration (without cascading errors). *White* areas show non-accumulation periods that not included in analysis. 125

Figure 5-1. (a) Public roads (red) through major mountain pass of the Washington Cascades. (b) Locations of available meteorological stations measuring at least air temperature at a hourly resolution as of February 2016. (c) Regional map..... 143

Figure 5-2. (a) Washington Cascades and Snoqualmie Pass study domain (b) False color MODIS image on January 10 2009 showing extent of low clouds east of passes during a period of high

pressure over Washington State in between storm systems. (c) Snoqualmie Pass study domain (White boxes in (a) and (b)), showing the locations of stations used in analysis. *Black dots* show the center of 4/3 km WRF grid cells, which marginally resolve the pass valley. Precipitation phase was mainly evaluated at the SNQ station (*red circle*) using disdrometer observations. .. 144

Figure 5-3. Climatological wind roses during winter (DJF) at the Dodge Ridge station located at the summit (1146 m) of Snoqualmie Pass (a), and hourly averaged air temperature during DJF as a function of wind direction (b). For each 1° wind direction bin, white circles show the median DJF air temperature, dark blue lines show the 25th and 75th percentiles, and line blue lines the max and min temperatures. 145

Figure 5-4. Observations from Snoqualmie Pass during water year 2015. Grey boxes highlight largest 10 storms by precipitation totals. (a) Air temperature from SNQ and cross-pass pressure gradient between KSEA to KELN, (b) Wind direction at the Dodge Ridge station, (c) Daily accumulated total gauge precipitation and measured SWE accumulation (via manual snow board measurements) at SNQ. 146

Figure 5-5. (a) Fraction of precipitation observed as ice (snow, graupel, hail etc.) within 10 min period by disdrometer observations compare to 10 minute air temperature averages. (b) Same observational data binned by 0.5°C x 0.1 snow-fraction bins, showing likelihood of snow/rain at each temperature range. (c) Total precipitation observed at SNQ during as a function of air temperature. 147

Figure 5-6. Observed fraction ice at SNQ versus observed 1 hour average air temperature at nearby pass stations and the nearest WRF grid cell. Solid line shows best fit linear model and vertical dashed line shows the un-calibrated model with an assumed threshold of 0°C. 148

Figure 5-7. Coefficients of determination (r^2) between hourly distrometer observations of snow-fraction and model predicted snow-fraction. Subplots separate water year 2015 into (a) all available hours (N=576), (b) the 10 wettest storms (highlighted in Figure 5-4), and (c,d) by wind directions as observed at the Dodge Ridge station. Below the x-axis shows the percentage of time and total precipitation observed during each period at the SNQ station when disdrometer observations were available 149

Figure 5-8. Total winter accumulation of snow water equivalent (SWE) observed and modeled at SNQ. Observed values are the product of disdrometer hourly snow-fraction and gauge observed precipitation. Modeled values are the product of predicted snow-fraction and gauge observed precipitation (solid lines) or WRF modeled precipitation (dashed lines). 150

Figure 5-9. 4-5 January 2015 case study. Observed and modeled (a) snow-fraction, (b) total precipitation rate, (c) cumulative frozen and liquid precipitation, (d) 2-m air temperature, (e) wind direction. *Disdrometer error codes prevented quality data but in-situ snow depth, lysimeter, and snow board observations indicate rainfall (not shown). 151

Figure 5-10. (a) Observed air temperature at Snoqualmie Pass during the 4-5 January 2015 event. Black horizontal lines show elevations and abbreviations of surface stations used (Alpental

Summit (AS), Dodge Ridge (DR), Alpental Middle (AM), and Snoqualmie Pass (SNQ)). (b) WRF modeled air temperature at near surface layers. Temperatures have been linearly interpolated between stations and WRF layers. 152

Figure 5-11. 4-5 January 2015 case study. (a) Domain of Snoqualmie Pass (shown in insert of Figure 1a) with locations of stations observing precipitation phase. (b-g) Background color shows WRF predicted fraction of 6 hour precipitation as ice. The annotated circle in (a) shows SNQ disdrometer observations of precipitation phase. *Blue (red) circles* indicate snowfall (rainfall), as derived from the 6 hour change in SNOTEL snowdepth. The Stampede Pass (SPP) station is annotated because it is located in the next pass to the south, where snowfall lasts longer during this event. 153

List of Tables

Table 2-1. Observations stations used within study basins.....	45
Table 2-2. Characteristics of selected study basins.	48
Table 2-3. DHSVM simulations.	49
Table 3-1. Meteorological observations.	78
Table 3-2. Snow and soil observations.	81
Table 4-1. Definitions of abbreviations used.....	111
Table 4-2. Model options and parameter values.....	113
Table 4-3. Number of days attributed to each source of modeled ¹ error.....	115
Table 5-1. Stations used in study.....	142

Chapter 1. Introduction

The winter hydrology of the western United States is largely driven by extra-tropical cyclones interacting with mountain ranges. The variability of storms' freezing levels and the phase of precipitation reaching the surface create a unique region defined as the transitional snow zone, which can be defined as receiving 10-50% of precipitation as snowfall (90-50% as rainfall). This mixed phase region covers a large area of the western US [Elsner *et al.*, 2010; Klos *et al.*, 2014], is prone to rain-on-snow floods [Harr, 1981; Kattelman *et al.*, 1997; McCabe *et al.*, 2007], and is most sensitive to projected climate warming [Mote *et al.*, 2005; Nolin and Daly, 2006]. Numerical simulations of transitional snow are critical for aiding flood forecasts during snowmelt floods [Rössler *et al.*, 2014] and providing boundary conditions for land surface models [Letcher and Minder, 2015].

Yet, simulating snow accumulation and ablation in the transitional zone remains a challenge for a number of reasons. There is a lack of high quality meteorological and snow observations required for model evaluation within the transitional zone compared to colder seasonal cover snow climates. This is mainly as a result of the need to sample areas where the bulk of the water supply is stored, but also due to difficulties in taking observations in transitional zones where mixed precipitation hampers measurement efforts. In addition, due to the typically shallow snowpack and low cold content (near isothermal snow) of the transitional snowpack, models are more sensitive to meteorological forcing [Wayand *et al.*, 2013] and structural errors [Lapo *et al.*, 2015], than colder seasonal snowpacks. Finally, traditional methods of partitioning precipitation into rain and snow [USACE, 1956; Auer, 1974] have the most uncertainty within the transitional snow zone, where near-surface air temperatures fluctuate

around the freezing point. Overall, there is a need for new observations and model evaluation within this snow climate.

This dissertation aims to improve understanding and model representation of transitional snow. Specially, I focus on processes that control snowmelt during rain-on-snow floods (distributions of snowpack mass and turbulent heat fluxes), annual snow depth accumulation (precipitation partitioning, snowfall density, and compaction), and local topographical impacts on snow accumulation within mountain passes (precipitation partitioning). Model evaluations were performed against observations at a recently instrumented snow study site. These three research areas and the observational data sets are addressed within four chapters as described below.

Chapter 2 examines the importance of snowmelt during the largest floods occurring in three basins along the West Coast of the United States [Wayand *et al.*, 2015b]. The paper quantifies how three factors (snow-level timing, vegetation, and basin hypsometry) combine to control the contributions of snowmelt versus rainfall in basin water input. Chapter 3 details a meteorological and snow data set that compiles historical and intensive recent observations at the Snoqualmie Pass snow study site (SNQ) in the Washington Cascades [Wayand *et al.*, 2015a]. Chapter 4 utilizes observations at the SNQ site to put forward a novel method of identifying the most common source of modeled snow accumulation errors in this challenging snow environment [Wayand *et al.* in review]. Finally, Chapter 5 focuses on evaluating two common methods of partitioning precipitation across the Snoqualmie Pass during water year 2015, which was identified in Chapter 4 as being unusually difficult to model.

Chapter 2. Modeling the influence of hypsometry, vegetation, and storm energy on snowmelt contributions to basins during rain-on-snow floods

Note: This chapter has been published in its current form as an article in *Water Resources Research* [Wayand et al. 2015]; the only differences are in section numbering and some reference information. It is used here by permission of John Wiley and Sons.

Abstract: Point observations and previous basin modeling efforts have suggested that snowmelt may be a significant input of water for runoff during extreme rain-on-snow floods within Western U.S. basins. Quantifying snowmelt input over entire basins is difficult given sparse observations of snowmelt. In order to provide a range of snowmelt contributions for water managers, a physically-based snow model coupled with an idealized basin representation was evaluated in point simulations and used to quantify the maximum basin-wide input from snowmelt volume during flood events. Maximum snowmelt basin contributions and uncertainty ranges were estimated as 29% (11-47%), 29% (8-37%), and 7% (2-24%) of total rain plus snowmelt input, within the Snoqualmie, East North Fork Feather, and Upper San Joaquin basins, respectively, during historic flooding events between 1980 and 2008. The idealized basin representation revealed that both hypsometry and forest cover of a basin had similar magnitude of impacts on the basin-wide snowmelt totals. However, the characteristics of a given storm (antecedent SWE and available energy for melt) controlled how much hypsometry and forest cover impacted basin-wide snowmelt. These results indicate that for watershed managers, flood forecasting efforts should prioritize rainfall prediction first, but cannot neglect snowmelt contributions in some cases. Efforts to reduce the uncertainty in the above snowmelt simulations

should focus on improving the meteorological forcing data (especially air temperature and wind speed) in complex terrain.

2.1 Introduction

The largest historical flood events over the Western U.S. have occurred under the influence of atmospheric rivers, which transport warm moisture-laden air from over the Pacific Ocean into the mountains [Ralph *et al.*, 2005; Neiman *et al.*, 2010]. These conditions cause heavy precipitation rates and high snowfall-levels (where rain transitions to snow at the surface), resulting in a larger basin fraction experiencing rainfall instead of snow. They also expose the existing snowpack to warm, humid, and windy atmospheric conditions that drive high melt rates [Marks *et al.*, 1998].

Quantifying the contribution of runoff from snowmelt versus rainfall during rain-on-snow (ROS) conditions is challenging because sparse observations of snowmelt (e.g. snow pillows) cannot capture basin-wide variability. Available observations at point locations in non-forested areas suggest that snowmelt represents 4% to 72% of total water input during ROS events [Harr, 1981; Singh *et al.*, 1997; Marks *et al.*, 1998, 2001; Sui and Koehler, 2001; Garvelmann *et al.*, 2015] with melt rates up to 30-65 mm day⁻¹ [Kattelmann, 1997; Marks *et al.*, 2001; Cooley and Palmer, 1997]. During cloudy ROS conditions, the fluxes into the snow surface from turbulent heat [Harr, 1981; Storck, 2000; Marks *et al.*, 2001; Garvelmann *et al.*, 2014] and long-wave irradiance [Mazurkiewicz *et al.*, 2008] have been shown to become more important for melting snow than net irradiance alone. However, these point observations cannot be easily extrapolated across complex terrain and vegetation to calculate total basin contributions from snowmelt without the availability of high density observations [Garvelmann *et al.*, 2015].

In lieu of ideal snow observations, hydrological models are commonly used as a tool to explore the controls on distributed snowmelt across heterogeneous basins given accurate forcing data [Clark *et al.*, 2011, Rössler *et al.* 2014, Wever *et al.* 2014b]. In particular, the impact of forest harvesting to increase turbulent heat fluxes and snowmelt rates in clearings during well-studied ROS storms has frequently been quantified through modeling [Berris and Harr, 1987; Harr and Coffin, 1992; Heeswijk *et al.*, 1996; Marks *et al.*, 1998; Storck and Bowling, 1998; Jones and Perkins, 2010; Varhola *et al.*, 2010]. However, to fully understand the role of changes in snow water equivalent (SWE) across a range of locations and ROS events, one must both quantify the skill of the energy balance snow model and perform a wide range of both idealized and realistic simulations. Case studies using the SNOBAL model [Marks *et al.*, 1998] to simulate the 5 February 1996 event reported the model under-predicted the observed melt rates and magnitudes [Heeswijk *et al.*, 1996; Marks *et al.*, 1998; Mazurkiewicz *et al.*, 2008], while other ROS studies did not report model performance of individual events [Biggs and Whitaker, 2012]. More recently, Rössler *et al.* [2014] found that either meteorological forcing or snow model parameters required adjustment in order to match model results with point observed decreases in snow depth and basin runoff. Hence, this study attempts to both 1) quantify how well a snow model can capture observed changes in SWE during ROS events given varied sources of forcing data and 2) provide realistic ranges of total basin snowmelt contributions during flooding for different basin hypsometries and forest cover given these uncertainty bounds from point simulations.

We examine the importance of snowmelt input to basin runoff during ROS events by focusing on three maritime basins along the west coast of the U.S., where ROS events occur

frequently [Kattelman, 1997; McCabe et al., 2007]. A simplified basin representation is employed to allow the separation of basin scale controls (i.e. forest distribution and hypsometry) from storm controls (i.e. initial snowpack and energy available for melt) in order to provide bounds on when/where volumetric snowmelt matters for flood forecasting. Because most operational forecasts involve ensembles of atmospheric predictions (rain rates and air temperatures) but less information about surface hydrology, local reservoir operators are often using knowledge of specific basin hypsometry and pre-storm snow cover to estimate ad hoc how much snowmelt might contribute to total predicted rainfall amounts for their target basin(s). A better understanding of the realistic ranges of snowmelt contributions to streamflow runoff during major winter storms increases our confidence when operating large dams and reservoirs for flood risk management (Personal communication, Larry Schick, USACE).

2.2 Background

The two major physical limitations of basin snowmelt contributions are the available mass of snow and the energy available to melt, as conceptualized by *Biggs and Whitaker* [see their Figure 1, 2012]. We expand on this understanding by including the elevational distribution of forest cover and basin area (hypsometry). Figure 2-1a illustrates two possible distributions of SWE with increasing elevation prior to a ROS event with the same potential energy for melt (Figure 2-1b). “Initial condition #1” exemplifies a SWE distribution where the snow cover extent (lowest elevation with snowcover) is located at the climatological transition of rainfall to snowfall. In contrast, the SWE distribution in “initial condition #2” represents a recent snowfall at lower elevations, where there is greater energy available for melt due to higher air temperatures. Figure 2-1c,d shows how the resulting total storm snowmelt is limited by the initial

conditions, depending upon the hypsometry of the basin (uniform area with elevation in c and greater area at lower elevations in d). In contrast, given a fixed amount of initial SWE (Figure 2-1e), the energy during storms may vary due to increased air temperatures, stronger winds, or forest cover (Figure 2-1f), which will shift and/or increase the distribution and quantity of snowmelt depending on basin hypsometry (Figure 2-1g,h).

Both distributions of mass and energy are, to a first order, controlled by the snowfall-level, defined here as the surface elevation where 50% liquid and 50% solid precipitation occur, generally coincident with near-surface air temperatures of about 1°C. On average, the winter snowfall-level decreases with increasing latitude [-41.4 m^{-1} in the Sierra Nevada, *Lundquist et al.* 2008]. However, on the time scales of hours to days that ROS events occur on, the snowfall-level over a given basin is controlled by the passage of fronts, diurnal fluctuations and by orographic effects [*Lundquist et al.*, 2008a; *Minder et al.*, 2010; *Minder and Kingsmill*, 2013].

For snowmelt to contribute significantly to runoff, the hypsometry of the basin must have a large fraction of total area coincident with those elevations where snowmelt is maximized [*Biggs and Whitaker*, 2012]. For example, a basin may have high melt rates between 500 to 1500 m, but if this elevation range only represents 5% of basin area, then the snowmelt contribution to total basin input and outflow will not be significant. A similar process has been shown for rainfall, where *White and Gottas* [2002] found a strong relationship between the melting level and the peak flow rate depending on the basin hypsometry.

In summary, it has been well established that vegetation, hypsometry, antecedent snow conditions and storm energy are related to the magnitude of snowmelt during ROS conditions [*Kattelman et al.*, 1997; *Marks et al.*, 2001; *McCabe et al.*, 2007; *Rössler et al.*, 2014]. However,

quantifying basin snowmelt magnitudes over multiple basins and a range of ROS events has yet to be done. Further, it remains to be shown if storm variability outweighs basin characteristics for controlling basin snowmelt. This paper seeks to contribute to the understanding of the role of snowmelt during ROS floods by answering the following questions:

1. How well can the magnitude of observed mid-winter snowmelt during ROS conditions at points be consistently captured by a physically based snowmodel?
2. How much does simulated snowmelt contribute to volumetric basin input during floods over three Western US basins?
3. How much does a basin's specific hypsometry and forest cover control ROS basin snowmelt compared to individual storm characteristics, such as antecedent SWE distribution and energy for melt?

We answer question 1 through model testing at both points with intensive observations (to quantify model uncertainty) and at points with less certain site meteorology (to quantify additional uncertainty due to model forcing). We answer questions 2 and 3 by modeling snowmelt volume input to basin-wide runoff during ROS storms within three basins with different distributions of basin area and forest cover. Sources of data from the intensive observational snow study sites and the study basins along the Western U.S. coast are described in section 2.3. The snow model and idealized basin framework are described in section 2.4, and results reported in section 2.5. A discussion of simulated results is given in section 2.6, and a summary of the main findings in section 2.7.

2.3 Data

2.3.1 Intensive observational study sites

Two snow study sites were selected to validate the model's ability to simulate snowmelt during ROS events: the Col de Porte (CDP) site, located in the Chartreuse range in southeast France [Morin *et al.*, 2012], and the Umpqua National Forest (UNF) site in the Oregon Cascades, USA [Andreadis *et al.*, 2009] (Table 2-1). These sites were chosen because they measured all meteorological data required to force an energy balance snow model, thus termed “near-perfect” forcing here on. Although other snow study sites with intensive observations exist [Essery *et al.*, 2009], only CDP and UNF experience multiple mid-winter melt events per water year, providing ideal sites to test the ability of a physically-based snow model to simulate snowmelt during ROS events given high quality forcing data. Model skill from these two sites was used to quantify the model error to capture ROS storm snowmelt given “near-perfect” forcing. This model error is used to better inform our uncertainty of basin scale simulated snowmelt totals within the three Western U.S. basins that are the main focus of this study. However, we do not explore the full range of model uncertainty here as it is outside the scope of this paper. Finally, despite the large geographical distance of the CDP site from the Western U.S., it is suitable for inclusion in this study because of the similar maritime snow classification [Sturm *et al.*, 1995] and impact of atmospheric rivers upon Western Europe as the Western U.S. [Newell *et al.*, 1992].

Meteorological forcing data used for point snow model simulations were taken directly from the published data sets at CDP [Morin *et al.*, 2012] and UNF [Andreadis *et al.*, 2009]. Ten water years (2002-2011) at CDP and two water years (1997-1998) at UNF of both meteorological forcing (air temperature, precipitation, wind speed, relative humidity, and short- and long-wave irradiance) and observed daily SWE for model validation were available.

2.3.2 Study basins with limited observations

The mountain ranges along the Western U.S. coast (Washington and Oregon Cascades, and Sierra Nevada) include ephemeral, maritime and alpine snow climates [Sturm *et al.*, 1995] and contain elevations from sea-level to 3500 m (Figure 2-2). Three example basins (1797 - 4244 km², Figure 2-2a) were arbitrarily chosen where frequent ROS events were documented to have occurred [see Figure 6, McCabe *et al.* 2007]. Each basin is affected by synoptic systems with different mean snowfall-levels, variable distributions of forest cover, and unique basin hypsometry (Table 2-2). Figure 2-2c shows hypsometric curves for each of the three study basins in context with curves for all basins along the U.S. west coast. The largest fraction of basin area occurs within the Snoqualmie (SNQ) basin at low-elevations, in the East branch of the North Fork Feather (ENFF) basin at middle-elevations, and over the Upper San Joaquin (USJ) basin at high-elevations. Forest cover in each basin is a function of both climatology and deforestation. The elevations of observational stations used for validation of modeled SWE within each basin are shown in Figure 2-2c and further detailed in Table 2-1.

The regulation of streamflow within each basin varies. The ENFF basin has no flood protection or power generating dams but only five small minor diversions for water supply to Quincy (0.16% area), while the SNQ basin has one hydropower dam (South Fork Tolt Dam) that represents only 3% of the SNQ basin drainage. In contrast, the SJ basin has six large reservoirs designed to maximize water retention and hydropower generation.

In order to represent a range of ROS meteorological storms at different latitudes, we used a 12 km gridded observational data set over the study domain from 1980 to 2008 [Maurer *et al.*,

2002]. Grid cells within each of the three selected basins (Figure 2-2a) were extracted, and daily values were disaggregated to hourly using the Mountain Climate Simulator (MTCLIM) [Hungerford *et al.*, 1989; Thornton and Running, 1999]. Daily precipitation was uniformly distributed throughout the day. Air temperature at two meters above ground was disaggregated to hourly values using a spline fit to daily maximum and minimum temperature following the implementation in the Variable Infiltration Capacity model [Liang *et al.*, 1994; Maurer *et al.*, 2002]. Daily shortwave irradiance was disaggregated to hourly based on the solar zenith angle, and longwave irradiance based on the hourly air temperature and assuming a constant vapor pressure during the day [Tennessee Valley Authority, 1972]. Air pressure and windspeed were assumed uniform throughout the day. Wind speeds in the Maurer *et al.* [2002] data set were created by interpolation from the NCEP–NCAR reanalysis [Kalnay *et al.*, 1996] lowest model level to 10 m above the surface. Biases and uncertainty in this gridded data set were quantified and corrected before input to snow model simulations (See section 2.4.2).

Daily observations of SWE from the U.S. Natural Resources Conservation Service’s SNOTEL network, the California Department of Water Resources (CDWR), and the U.S. Bureau of Reclamation (USBR) were obtained within each study basin (Table 2-1) to select ROS events and were used for evaluation of modeled SWE in the SNQ basin.

2.4 Methods

First, the physical snow model used in this study was tested to capture the observed snowmelt magnitudes during ROS events at point sites with both “near-perfect” and estimated sources of forcing data (Question 1). Bias-corrected gridded data over each study basin were then used to drive snowmodel simulations during multiple ROS events to estimate volumetric contributions

of snowmelt to basin input (Question 2). Finally, we compare the controls of basin characteristics to individual storms on basin total snowmelt (Question 3).

2.4.1. Snow Model

Snow simulations (Table 2-3) at point locations within each basin were performed using the Distributed Hydrology Soil and Vegetation Model (DHSVM), which is a physically-based hydrological model that simulates the surface energy and water balances and the transport of water as a function of meteorological forcing, topography, soil drainage characteristics, and vegetation cover [Wigmosta *et al.*, 1994; Waichler and Wigmosta, 2003]. This model was selected because it explicitly includes a forest canopy, which exerts a large control over the energy and mass fluxes into the snowpack during ROS events [Marks *et al.*, 1998]. We only used the vegetation and snow model components of DHSVM run in *point mode*, as the scope of this paper is on snowmelt water available for runoff. Although more physically based spatial distributions are commonly used, running in point mode allows the clean separation of impacts of vegetation and basin hypsometry on the snowmelt basin input. We leave interactions between snowmelt, soil moisture, and runoff generation as subjects for future research.

DHSVM's snowpack is represented by two snow layers; a surface layer and pack layer. Liquid water in the snowpack is held until a predefined saturation level (3.3% of SWE) is reached, where upon additional rainfall or snowmelt is routed to the upper soil layer. Turbulent heat fluxes are calculated based on bulk transfer theory and stability corrections using the bulk Richardson number (See *Andreadis et al.* (2009) for full details). At every time step, DHSVM requires the following meteorological forcing data: precipitation, 2 m air temperature, relative humidity, wind speed above canopy, and downward short- and long-wave irradiance.

Precipitation was partitioned into liquid when local air temperatures were above 3°C, a linear

mix of liquid and ice between -1°C and 3°C , and ice below -1°C [USACE, 1956]. Additional model parameter values were taken from previous studies when available, or their default values were used.

Vegetation classification for each basin was obtained from the National Land Classification Database [Fry, Joyce A and Coauthors, 2011] at a 30 m resolution. Over all study basins in Figure 2-2a, evergreen forests were the most prevalent (49%), followed by shrub-land (18%) and grass-land (10%). As a first order approximation, all categories were reclassified as either an evergreen forest or as short grass. All deciduous or mixed forest cells were assigned to evergreen forest. All remaining cells, including barren rock, shrub and grassland, were assigned to grass vegetation without any overstory. Vegetation parameters for all point simulations (Section 2.4.3) used a grass classification, as this matches the majority of vegetation immediately surrounding each study site.

2.4.2. Forcing data

Downscaling 12 km gridded data

The meteorological forcing required by DHSVM was prepared using the hourly variables derived from the Maurer *et al.* [2002] 12 km gridded data set described in section 2.3.2. For point simulations (Section 2.4.3), the nearest grid cell was selected. For elevation bin simulations (Section 2.4.4), all grid cells with average elevations within each 100 m elevation bin were combined by averaging their forcing data to provide one point forcing representative of the average elevation range. Elevation corrections between Maurer *et al.* [2002] 12 km grid cells and elevation bins were made for air temperature and longwave irradiance: Annual temperature lapse

rates used in each basin were taken based on previous studies when available: SNQ $5^{\circ}\text{C km}^{-1}$ [Minder *et al.*, 2010], ENFF $6.5^{\circ}\text{C km}^{-1}$ [Lundquist *et al.*, 2010], and USJ $6.8^{\circ}\text{C km}^{-1}$. Longwave irradiance was adjusted using a constant lapse rate of $-29\text{ W m}^{-2}\text{ km}^{-1}$ derived from three years of data in the Swiss Alps [Marty *et al.*, 2002] and since applied in the Western U.S. [Hinkelman *et al.*, 2015].

Bias correction of gridded data forcing

Due to known limitations of reanalysis gridded data sets [Mizukami *et al.*, 2014; Newman *et al.* 2015; Lundquist *et al.* 2015] and disaggregation methods [Bohn *et al.*, 2013], available observations of air temperature and precipitation were used to bias correct Maurer *et al.* [2002] grid cells in each basin. Within the SNQ basin, the average October to March air temperature (after correcting for elevation differences between grid cells and stations) was biased on average -0.6°C , and accumulated total precipitation was biased on average -32% of observations. Within the ENFF and USJ basins where only reliable historical precipitation (but not temperature) records exist, the Maurer *et al.* [2002] grid cell precipitation values were biased by -2% and -0.8% , respectively.

Uncertainty in gridded forcing

Given that the accuracy of the meteorological forcing is critical for modeling ROS event snowmelt [Rössler *et al.*, 2014], an ensemble of forcing data perturbations were estimated (Table 2-1). In the absence of measurements, values from the literature were used [see Table 3, Raleigh *et al.*, 2014]. Random errors and diurnal errors from sub-daily interpolations were not addressed. For air temperature, uncertainties were estimated from both the RMSE and mean differences

between the three SNQ stations and their nearest grid-cells, which resulted in values of ± 3.3 °C and ± 0.8 °C, respectively. Uncertainty in total precipitation was quantified as $\pm 19\%$ based on the mean difference at all 13 sites observing precipitation (Table 2-1). All remaining forcing uncertainty ranges were estimated from *Raleigh et al.* [2014] and citations therein; wind speed ± 3 m s⁻¹, relative humidity $\pm 25\%$, longwave irradiance ± 25 W m⁻², and shortwave irradiance $\pm 20\%$.

2.4.3. Selection of rain-on-snow events

Point sites

ROS events were defined at point sites if they met the following criteria, 1) they occurred between October and February (when most ROS events occur [*McCabe et al.*, 2007]), 2) observed SWE decreased, and 3) greater than 5 mm of rain fell (roughly twice the precipitation gauge accuracy) over three days. A 3-day (72 hour) event period was identified as the average length of time required to capture the majority of rainfall and snowmelt at all sites and has been used previously for defining storm length [*Serreze et al.*, 1999]. Using the 3-day period, 8 to 56 events were identified at each station (see Table A1 and Table S1 of *Wayand et al.*, 2015b), depending on station records and the frequency of mid-winter melt. Maximum 3-day snowmelt totals ranged from 35 mm at CDP to 124 mm at the SKU station within the SNQ basin. In contrast, maximum rainfall ranged from 75 mm at CDP to 357 mm at SKU, over a 3-day period.

Study basins

ROS events at each study basin were defined if any of the available stations within each basin (Table 2-1) met the same three criteria as above. Of these selected events we also identified ROS

events that resulted in flooding or not (see Table S1 in *Wayand et al.*, 2015b). Three United States Geological Survey (USGS) discharge gauges nearest to each basin outlet were used to identify flooding events (Table 2-1). Within the SNQ basin, the Snoqualmie River near Carnation Gauge (#12149000) drains 87% of the study basin and has a USGS rated flood stage of 54 ft, or 546 cms, resulting in 49 selected flood events. The nearest gauge to the ENFF outlet was discontinued in 1982, thus two gauges were used instead (Spanish Creek #11402000 and Indian Creek #11401500), which drain 18% and 72% of the ENFF study basin, respectively. No flood rating is available for these gauges, so historical [*Roos*, 2007] accounts of flooding on the Feather River were used to select a threshold of 260 cms for the Spanish Creek gauge that identified four flooding events between 1980 and 2008. In the USJ, we selected the San Joaquin river gauge below the Friant dam as it drains the entire USJ basin. Releases from the dam are restricted to 226.5 cms to prevent downstream flooding [*Bureau of Reclamation*, 2005], thus daily flows exceeding 226.5 cms were selected as flooding or high flow events. The resulting four selected floods agree with historical accounts of flooding [*Roos*, 2007; *Bureau of Reclamation*, 2005].

2.4.4. Evaluation of point DHSVM simulations of snowmelt

The ability of DHSVM simulations (Sims, 1-8, Table 2-3) to capture the seasonal pattern of SWE was assessed using the coefficient of determination, and percent bias of mean peak SWE. During study events, the model's ability to capture the observed storm melt (total over 72 hours) was assessed using the root mean squared error (RMSE). At the CDP and UNF sites, these RMSE values provide a quantification of DHSVM's model error when driven by "near-perfect"

forcing. At the remaining three SNQ basin sites, the RMSE values quantify the total error in simulated snowmelt as a result of the reduced quality of meteorological forcing data and inherent model error. Both point scale uncertainty estimates are used to inform our basin scale modeling analysis of snowmelt contributions during ROS flood events.

2.4.5. Idealized representation of basin snowmelt

An idealized framework was used to model basin snowmelt and rainfall available for runoff. This framework allowed the separation of influences from basin vegetation and hypsometry for controlling the total basin contribution from snowmelt during each study event. First, each basin was binned into 100 m elevation bands (Figure 2-3). Variations in slope and aspect were neglected in our idealized set up, as they are less important during ROS events [Kormos *et al.*, 2014]. Then, DHSVM was run in point mode at each elevation band with two vegetation settings: completely forested (Sims 9.1a-q, 10.1a-q, 10.1a-q) and completely grass (Sims 9.2a-q, 10.2 a-q, 11.2a-q), where sub-scripts a-q refer to variations in forcing data using uncertainties described in Section 2.4.2. The model outputs (i.e. snowmelt or rainfall) at each elevation band from the forest and grass simulations were then linearly combined based on the observed vegetation fraction at that elevation band (see Figure 2-3). These simulations assume a uniform area with elevation and are thus referred to as “unit-area.” Finally, basin hypsometry was included by multiplying the vegetation-weighted model output by the fraction of area at each elevation band (shown cumulatively in Figure 2-2b), which results in the most physical estimate of basin input of rain (Equation 1) and snowmelt (Equation 2).

$$Rain_{basin}(t) = \sum_{i=z_{min}}^{z_{max}} [Rain(i,t) \times Area(i)] \quad (1)$$

$$Melt_{basin}(t) = \sum_{i=z_{min}}^{z_{max}} \left[Melt_{Grass}(i,t) \times (1 - f_{forest}(i)) + Melt_{Forest}(i,t) \times (f_{forest}(i)) \right] \times Area(i) \quad (2)$$

where *Melt* and *Rain* are the DHSVM point simulated snowmelt and rainfall at each elevation band *i* over each hourly timestep *t*, and *f_{forest}* and *Area* are the fraction of forest and area at each elevation band that spans each basin's elevational range (*z_{min}* to *z_{max}*). Here we make the assumption that the snowpack reaches saturation quickly and therefore the majority of rain falling on the snowpack reaches the soil within the 3-day extreme rainfall events examined here.

2.5 Results

2.5.1. Evaluation of DHSVM at point snow study sites (Question 1)

“Near-Perfect” Forcing: Col de Porte and Umpqua National Forest

Simulations (Sims 1 and 2) at the two intensively observed study sites provided a benchmark for the skill of DHSVM to capture seasonal and ROS event snowmelt by nearly eliminating meteorological forcing error. At the Col de Porte (CDP) site, DHSVM captured the observed seasonal cycle of SWE with a mean peak SWE bias of -12% and a coefficient of determination of 0.9 (10 years) (Figure 2-4). At the Umpqua National Forest (UNF) site, DHSVM had a mean peak SWE bias of -26% and a coefficient of determination of 0.6 (2 years). Additional statistics are given in Table 2-B1. The decent representation of seasonal SWE was not unexpected given the high quality winter forcing data measured at each site; however, it provides confidence in the use of DHSVM in this study.

During 3-day ROS storms at CDP and UNF, simulations by DHSVM captured the observed snowmelt magnitudes (Figure 2-5), with RMSEs of 8 mm and 17 mm, at CDP and UNF respectively (Table 2-B1). To put these errors in perspective, they were 40% (21%) and

80% (27%) of the average (maximum) observed snowmelt over each 3-day event at CDP and UNF, respectively. Because the model was forced with “near-perfect” meteorological forcing at these sites, we make the assumption that the above errors at both sites are the result of DHSVM model error, which is on average 12 mm, including storms from both CDP and UNF.

Gridded Forcing: Snoqualmie Basin Snotel stations

Observed snowmelt magnitudes at SNQ stations during observed flooding events were larger than those values at CDP or UNF (Figure 2-5). Although observed and modeled snowmelt totals were higher during the larger rainfall events, neither were correlated with the rainfall magnitude, supporting the conceptual understanding that advected heat from rainfall is not providing the majority of energy for melt. Model simulations forced with available in-situ observations of air temperature and precipitation (Sims 3, 4 and 5) and only bias-corrected nearest grid cell data (Sims 5, 6 and 7), captured the range of observed snowmelt event totals, but had difficulty capturing some events. RMSEs for each station ranged between 19 mm to 28 mm per 3-day event (98-152% of average observed snowmelt, or 19-27% of maximum observed snowmelt), which were higher than normalized RMSEs at CDP or UNF. These increased errors represent the combination of DHSVM model error (12 mm from the CDP and UNF sites) plus the additional uncertainty of the lower-quality forcing data available at these locations.

2.5.2. Quantifying Basin Snowmelt during rain-on-snow events within an idealized framework (Question 2)

Simulated basined average inputs during all 3-day events, sorted by the sum of rainfall during each event, are shown in Figure 2-6. Overall, the SNQ and ENFF basins generated larger

snowmelt totals than the USJ basin, which we attribute to the relatively higher-elevation, and less variant, snowfall-levels during events at USJ basin. Interestingly, snowmelt magnitude appears to be invariant during flooding events within the SNQ basin, which led to snowmelt being a larger fraction of total basin input during the smaller rainfall events. This simulated basin-wide result is in agreement with point observations in Figure 2-5.

The basin-wide average (maximum) snowmelt storm-totals during flooding events, were 13 mm (35 mm), 36 mm (47 mm), and 3 mm (5 mm), for the SNQ, ENFF, and USJ basins, respectively. In terms of a percentage of total basin input (snowmelt and rainfall), basin-wide snowmelt had average (maximum) values of 10% (29%), 21% (29%) and 5% (7%) of water available for runoff for each basin, respectively, indicating that rainfall was the primary contributor to volumetric basin input during flooding events examined here. Sensitivity of the above results to model and meteorological forcing uncertainties is discussed in Section 2.6.

2.5.3 Basin and Storm controls on snowmelt (Question 3)

The snowmelt contributions presented above varied between basins. To understand the controls on basin-integrated snowmelt, we separated out the impacts of basin characteristics (hypsometry and forest distribution) from the storm characteristics (antecedent SWE and available energy for melt) using our conceptual understanding of the controls on snowmelt included in our idealized framework defined in Section 2.4.5.

The impacts of storm characteristics were isolated by comparing basin-wide simulated snowmelt under the assumptions that all basins had a unit-weighted area and were entirely

covered in grass (i.e. no forest). The SNQ basin had the highest median and maximum snowmelt values during all study storms, followed by the ENFF and USJ basins (Figure 2-7a). The larger snowmelt totals within the SNQ basin compared to the USJ basin were driven by both higher magnitude melt rates and greater elevation ranges exposed to melt (Figure 2-7b). The lack of antecedent SWE was a more important limitation within the USJ basin than within the SNQ basin, where the available energy for melt was the largest limiting factor for maximizing basin-wide snowmelt totals.

The impacts of basin hypsometry (Figure 2-7d) on the basin averaged snowmelt totals are illustrated in Figure 2-7c. We defined the hypsometry impact ratio as the total snowmelt occurring when actual basin areas were used, divided by total snowmelt originating when each elevation was assigned equal area (i.e. uniform in Figure 2-7d). Within a given basin, the ratio varied depending on the elevation where snowmelt was maximized. For example, in the USJ basin, snowmelt predominantly occurred above 2000 m (Figure 2-7b), where the actual basin area is greater than a unit-weighted distribution (Figure 2-7d). Across all basins, the median ratios for each basin were positive (1.05 to 1.3), indicating that the impact of the actual hypsometry increased basin-wide snowmelt contributions.

The impact of forest cover distribution (Figure 2-7f) on basin-wide snowmelt is illustrated in Figure 2-7e. We defined the forested impact ratio as the basin-wide snowmelt total using the observed forest cover, divided by the snowmelt total when assuming an entire basin of grass (forest fraction = 0). Across all basins the median ratios were less than one (0.5 to 0.8), indicating the presence of forest canopy reduced basin-wide snowmelt contributions. However, the magnitude of the snowmelt reduction depended on the given storm.

The above results of the basin scale controls on simulated snowmelt agree with the existing conceptual understanding (Figure 2-1); namely that forest canopy reduces turbulent heat fluxes and melt rates (Figure 2-7e), and basins such as ENFF with a large fraction of basin area coincident with elevations of maximum snowmelt increase total basin snowmelt contribution (Figure 2-7c). What was not known before and has emerged from this idealized representation, was that the range of different storm characteristics (including both antecedent SWE and available energy for melt) have a large influence on the magnitude and sign of how basin characteristics (hypsometry and forest cover) impact basin-wide snowmelt (the dots and inter-quartile ranges in Fig. 7 span a wider range than the different medians between the three basins).

2.6 Discussion

2.6.1. Uncertainties in modeling snowmelt during ROS events

Changes in SWE during extreme rainfall events are difficult to consistently simulate accurately [Heeswijk *et al.*, 1996; Marks *et al.*, 1998; Westrick, 2001; Mazurkiewicz *et al.*, 2008; Rössler *et al.*, 2014], which is supported by the results of point simulations in this study (Figure 2-5, Table 2-B1). Simulations of individual events were not consistent enough to warrant use in an operational mode if the forcing uncertainty of weather forecasting models is of similar magnitude to the Maurer *et al.* (2002) gridded data set errors found here (Section 2.4.2). Efforts to further reduce modeled snowmelt errors should be focused on improving forcing variables that matter most, as well as adding additional observations of internal snowpack states and fluxes, as discussed below.

Uncertainties in point simulations

The quality of metrological forcing data used for simulations of point ROS event snowmelt was shown to impact model accuracy (Table 2-B1). DHSVM performed the best when given in-situ forcing at the CDP and UNF intensive observational point sites, but did not perform perfectly, allowing the estimation of DHSVM model RMSE error at ± 12 mm. At the three SNQ sites, DHSVM captured the median and range of snowmelt (Figure 2-5) well, but had higher RMSEs than the CDP or UNF sites. However, model errors were not significantly higher at SNQ sites when in-situ air temperature and precipitation (Sims 3-5) were replaced with gridded values (Sims 6-8), suggesting that random errors remaining in the bias corrected *Maurer et al.* [2002] air temperature and precipitation had small impacts on results. The impact of errors within other *Maurer et al.* [2002] forcing variables such as longwave and shortwave irradiance, relative humidity and especially windspeed, on simulated snowmelt could not be quantified given the lack of direct observations within study basins examined here. In order to improve model performance, effort should be put toward adding and maintaining existing observations of these less common variables across elevational transects, which will help aid predictions of snowmelt and efforts to diagnose sources of error during extreme ROS events.

Uncertainties in basin simulations

Uncertainties in the default basin simulations (Sims 9-11a, Figure 2-6) due to the meteorological forcing data [*Maurer et al.*, 2002] were quantified through a sensitivity analysis described in section 2.4.2. The average (maximum) basin-wide snowmelt contributions during flooding events varied between 10-14 mm (30-42 mm), 9-38 mm (17-53 mm), and 2-4 mm (4-6

mm) within each basin given forcing perturbations (Table 2-C1). Results were most sensitive to biases in air temperature ($\pm 3.3^{\circ}\text{C}$) and wind speed ($\pm 3 \text{ m s}^{-1}$).

Uncertainties in basin snowmelt simulations due to DHSVM model error were also assessed. DHSVM model error of ± 12 mm per 3-day event was derived from the RMSE of point simulations at CDP and UNF. This model error was applied to basin simulations by adding and subtracting 12 mm of snowmelt from the storm simulated snowmelt at each elevation bin where snow was present. Including both sources of uncertainty (forcing and model), our estimates of the average (maximum) snowmelt basin contribution were 5-25 mm (21-54 mm), 6-51 mm (9-65 mm), and 1-13 mm (1-17 mm) within the SNQ, ENFF, and USJ basins, respectively. In terms of a percentage of total basin input (snowmelt and rainfall), basin-wide snowmelt had maximum values of 11-47%, 8-37%, and 2-24% of water available for runoff for each basin, respectively. At point SNQ stations, the total estimated uncertainty above encompasses the observed snowmelt during 87% of the 168 station/storm events shown in Figure 2-5, giving confidence that the true basin value lies within our uncertainty range for the SNQ basin.

Uncertainties in observations of snowmelt

Although snowpillows were designed and sited to be proxies for basin water supply, they are commonly used to validate snow models because they are the best spatial and temporal snow observation in Western U.S. mountainous terrain. A confounding issue with using snowpillows to validate modeled snowmelt is that decreased mass measurements by snowpillows are a combination of snowmelt and rainfall draining from the snowpack [Marks *et al.*, 1998; Engeset

et al., 2000]. In a homogeneous snowpack, liquid saturation should not exceed ~10% [Boone and Etchevers, 2001; Essery *et al.*, 2013] of bulk SWE, which can be assumed as an upper bound on the percent of the measured SWE loss that is rainfall draining from the snowpack. However, observations support the idea that preferential flow paths [Gerdel, 1948; Marsh and Woo, 1984; Williams *et al.*, 2010; Wever *et al.* 2014a] and lateral water channels form during ROS events [Eiriksson *et al.*, 2013], allowing water to collect on or diverge from a snowpillow. Penalizing snow models using incorrect snowmelt observations could lead to tuning of model parameterizations that would later impact model fidelity. To overcome this obstacle, more alternative observations of snowpack states and fluxes are needed. For example, the CDP site measures SWE with a cosmic ray counter that impacts the ground heat flux less than snowpillows [Morin *et al.*, 2012], while a recently developed system for acoustic sensing of snow [Kinar and Pomeroy, 2015] is non-invasive and portable. Finally, upward pointing radar has been used to detect and quantify the vertical propagation of liquid water in snow [Schmid *et al.*, 2014; Wever *et al.*, 2015]

2.6.2. Importance of snowmelt volume towards flooding

Volumetric basin input of snowmelt

Rainfall, and not snowmelt, was the dominant volumetric contributor at both point sites and over study basins (Figure 2-7) during flooding events examined here. We estimated that snowmelt contributions (and uncertainty ranges) to each basin were as high as 29% (11-47%), 29% (8-37%), and 8% (2-24%) within the SNQ, ENFF, and USJ basins, respectively. The maximum value of 29% (11-47%), in the SNQ basin is consistent with an in-house study by the USACE

that reported 20-24% over the nearby Green River basin using DHSVM in fully distributed mode (Personal communication, Larry Schick, USACE). Within the ENFF basin, our estimate of 29% (8-37%), includes the reported value of 20% by *Riesboll et al.* [1965] during the 1955 flood (not within our study period). Finally, our estimated snowmelt magnitudes and percent contributions within the USJ were much less than other basins, because a small fraction of the basin had snow cover prior to ROS events. These results suggest that while the volume of snowmelt is not the dominate source of basin input, it should not be neglected within flood forecasting ensembles.

Timing of simulated snowmelt and rainfall during example storm in the SNQ basin

To elucidate the timing of basin inputs, we examine the 19 January 2005 flood event because it had the maximum snowmelt contribution (29%) within the SNQ basin. Simulated snowmelt and accumulation (Sim 9.1a) at all elevation bins are shown in Figure 2-8a. The dashed black line shows the snowfall-level, defined here as the lowest elevation where 50% rain and 50% snow are falling, as partitioned by air temperature. Simulated rainfall inputs (Sim 9.1a) to the basin are shown in Figure 2-8b. Rainfall (snowfall) occurred above (below) the snowfall-level because a linear fraction of rain vs. snow is assumed between -1°C to 3°C [USACE, 1956].

This storm follows the classic pattern of a ROS storm [Kattelman *et al.*, 1997]. On 17 January, the snowfall-level dropped to 100 m a.s.l., bringing the snowcover-extent, defined as the lowest elevation with snow cover, down to 100 m. From 17 to 18 January the snowfall-level and snowcover-extent rapidly increased as the storm system advected warmer air from the southwest. The diurnal fluctuation of the snowfall-level and the snow cover extent controlled the elevational range where simulated snowmelt occurred. The observed snowpillow SWE response

(daily gain or loss) generally agreed with the modeled timing of SWE change throughout the 16 to 18 January period. Snowmelt magnitudes for this storm are compared in Figure 2-5. Point simulations captured snowmelt at the ALP site well, but over- and under estimate snowmelt at OLI and SKU stations, respectively. The timing of the area- and vegetation weighted basin inputs (Sims 9.1a and 9.2a) over the SNQ elevation range are shown in (Figure 2-8c). They illustrate that the peak rainfall input (17 January) did not occur simultaneously with peak snowmelt input (18 January). Despite a moderate snowfall-level on the 17 January (~1000 m), basin rainfall input peaked because 80% of the SNQ basin area lies below 1000 m (Figure 2-2).

Connection of basin volumetric input to peak discharge

Although we did not explicitly test if the volume of snowmelt during the 3-day period before a flood controlled the flood peak, it is a prerequisite to test if snowmelt volume is a large fraction of total input before the impact on peak discharge can be assessed. Our estimated ranges of 11-47%, 8-37%, and 2-24% suggest snowmelt volume matters sometimes. Given the meteorological uncertainties over study basins and impacts upon simulated snowmelt shown here, we argue that efforts should be focused on improving the forcing data by adding more observations and/or through the use of regionally-vetted numerical weather prediction models, followed by further point model evaluation, before addressing the question of snowmelt volume controls on peak discharge during floods. Previous studies using DHSVM have found it can capture peak flow but only given the correct meteorological forcing [Westrick, 2001; Westrick and Storck, 2002].

2.7 Conclusions

A physically-based snowmodel coupled with an idealized basin representation was used to quantify the range of volumetric contributions to basin input from snowmelt during flood events. Maximum snowmelt basin contributions and uncertainty ranges were estimated as 29% (11-47%), 29% (8-37%), and 7% (2-24%) for the Snoqualmie Basin, East North Fork Feather, and Upper San Joaquin basins, respectively, during floods. Rainfall input dominated during all flood events; however, snowmelt should not be neglected, especially during events with moderate rainfall totals. Capturing the variations in observed snowmelt between different ROS events was a challenge given uncertainties within the meteorological forcing data available in complex terrain. Finally, deconstructing the idealized basin representation revealed that both the hypsometry and forest cover of a basin had a similar, but opposite sign, impact on the basin-wide snowmelt totals. However, the characteristics of a given storm (antecedent SWE and available energy for melt) controlled the magnitude of how hypsometry and forest cover impacted basin-wide snowmelt. These results estimate the bounds of historical snowmelt contributions, which will aid reservoir water management to prioritize future flood risk management efforts and researchers to prioritize areas for observational and model development.

2.8 Tables

Table 2-1. Observations stations used within study basins.

Basin	Variable(s) Observed	Name	Network ^a	Lat	Lon	Elevation (m)
-------	-------------------------	------	----------------------	-----	-----	------------------

-	Hourly T, P, RH, U, SW, LW. Daily SWE.	Col de Porte (CDP)	Meteo-France	45.3	5.77	1325
-	Hourly T, P, RH, U, SW, LW. Daily SWE.	Umpqua National Forest (UNF)	[Andreadis et al., 2009]	43.26	-122.24	1200
SQ	Daily SWE, Daily P, Hourly T.	Alpine Meadows (ALP)	SNOTEL	47.78	-121.70	1066
	Daily SWE, Daily P, Hourly T.	Olallie Meadows (OLI)	SNOTEL	47.37	-121.45	1228
	Daily SWE, Daily P, Hourly T.	Skookum Creek (SKC)	SNOTEL	47.68	-121.62	1088
	Daily mean discharge	SQ R. near Carnation, 12149000	USGS	47.66	-121.92	41
ENFF	Daily SWE, Daily Precipitation	Kettle Rock	CDWR	40.14	-120.72	2225
	Daily SWE, Daily Precipitation	Rattlesnake	CDWR	40.13	-121.04	1859
	Daily SWE, Daily Precipitation	Grizzly Ridge	CDWR	39.92	-120.65	2103
	Daily mean discharge	Spanish Creek, 11402000	USGS	40.00	-120.95	1219

	Daily mean discharge	Indian Creek,	USGS	40.07	-120.92	1066.8
USJ	Daily SWE / Daily P	Poison Ridge	CDWR / USBR	37.40	-119.52	2103
	Daily SWE / Daily P	Chilkoot Meadow	CDWR / USBR	37.41	-119.49	2179
	Daily SWE / Daily P	Graveyard Meadow	CDWR / USBR	37.47	-119.29	2103
	Daily SWE / Daily P	Green Mountain	CDWR / USBR	37.56	-119.24	2408
	Daily SWE / Daily P	Huntington Lake	USBR	37.23	-119.22	2134
	Daily SWE / Daily P	Tamarack Summit	CDWR / USBR	37.16	-119.20	2301
	Daily SWE / Daily P	Kaiser Point	CDWR / USBR	37.30	-119.10	2804
	Daily SWE	Volcanic Knob	CDWR	37.39	-118.90	3063
	Daily SWE	Agnew Pass	CDWR	37.73	-119.14	2880
	Daily mean discharge	SJ R. below Friant Dam, 11251000	USGS	36.98	-119.72	90

^a Data was obtained from the U.S. Natural Resources Conservation Service's (SNOTEL) network, the U.S. Geological Survey (USGS), the California Department of Water Resources (CDWR), the U.S. Bureau of Reclamation (USBR), and the Metro-France Center. Observed variables are air temperature (T), total precipitation (P), relative humidity (RH), wind speed (U), shortwave irradiance (SW), longwave irradiance (LW), and snow water equivalent (SWE).

Table 2-2. Characteristics of selected study basins.

Name	Center Lat (°)	Center Lon (°)	Area (km ²)	Elevation Range (m)	Elevation of top 30% Area ^b (m)	Average DJF Snow-level (m)	% of Basin Forested	HUC-8 ID ^a
Snoqualmie (SNQ)	47.56	-121.72	1797	0-2000	0-500	~1000	70	17110010
East Branch North Fork Feather (ENFF)	40.09	-120.73	2661	700-2400	1400-2000	~1500	71	18020122
Upper San Joaquin (USJ)	37.36	-119.22	4244	100-3500	2000-2700	~2000	55	18040006

^a HUC-8 ID refers to the Hydrological Unit Codes defined by the National Ocean and Atmospheric Administration.

^b This metric indicates at what elevation range the largest fraction of basin area occurs

Table 2-3. DHSVM simulations.

Simulation (Sim) identifier ^a	Site (Basin)	Met. Forcing source	Variable perturbation	Vegetation setting in DHSVM
1	CDP	All observed	-	grass
2	UNF	All observed	-	grass
3	ALP (SNQ)	T, P observed. Other Gridded	-	grass
4	OLI (SNQ)	T, P observed. Other Gridded	-	grass
5	SKU (SNQ)	T, P observed. Other Gridded	-	grass
6	ALP (SNQ)	Bias corrected nearest grid cell	-	grass
7	OLI (SNQ)	Bias corrected nearest grid cell	-	grass
8	SKU (SNQ)	Bias corrected nearest grid cell	-	grass
9.1 a-q	(SNQ)	Bias corrected gridded data	Perturbed	grass
9.2 a-q	(SNQ)	Bias corrected gridded data	Perturbed	forest
10.1 a-q	(EBNFF)	Bias corrected gridded data	Perturbed	grass
10.2 a-q	(EBNFF)	Bias corrected gridded data	Perturbed	forest
11.1 a-q	(USJ)	Bias corrected gridded data	Perturbed	grass
11.2 a-q	(USJ)	Bias corrected gridded data	Perturbed	forest

^a Syntax for simulation (Sim) identifiers X.1 have grass and X.2 forest vegetation. For simulations 9 through 11, subscripts *a* refers to the default forcing while *b-q* refers to perturbations of air temperature ± 0.8 °C, ± 3.3 °C, precipitation $\pm 19\%$, windspeed ± 3 m s⁻¹, relative humidity $\pm 25\%$, longwave irradiance ± 25 W m⁻², and shortwave irradiance ± 20 %, respectively (see Section 2.4.2).

2.9. Figures

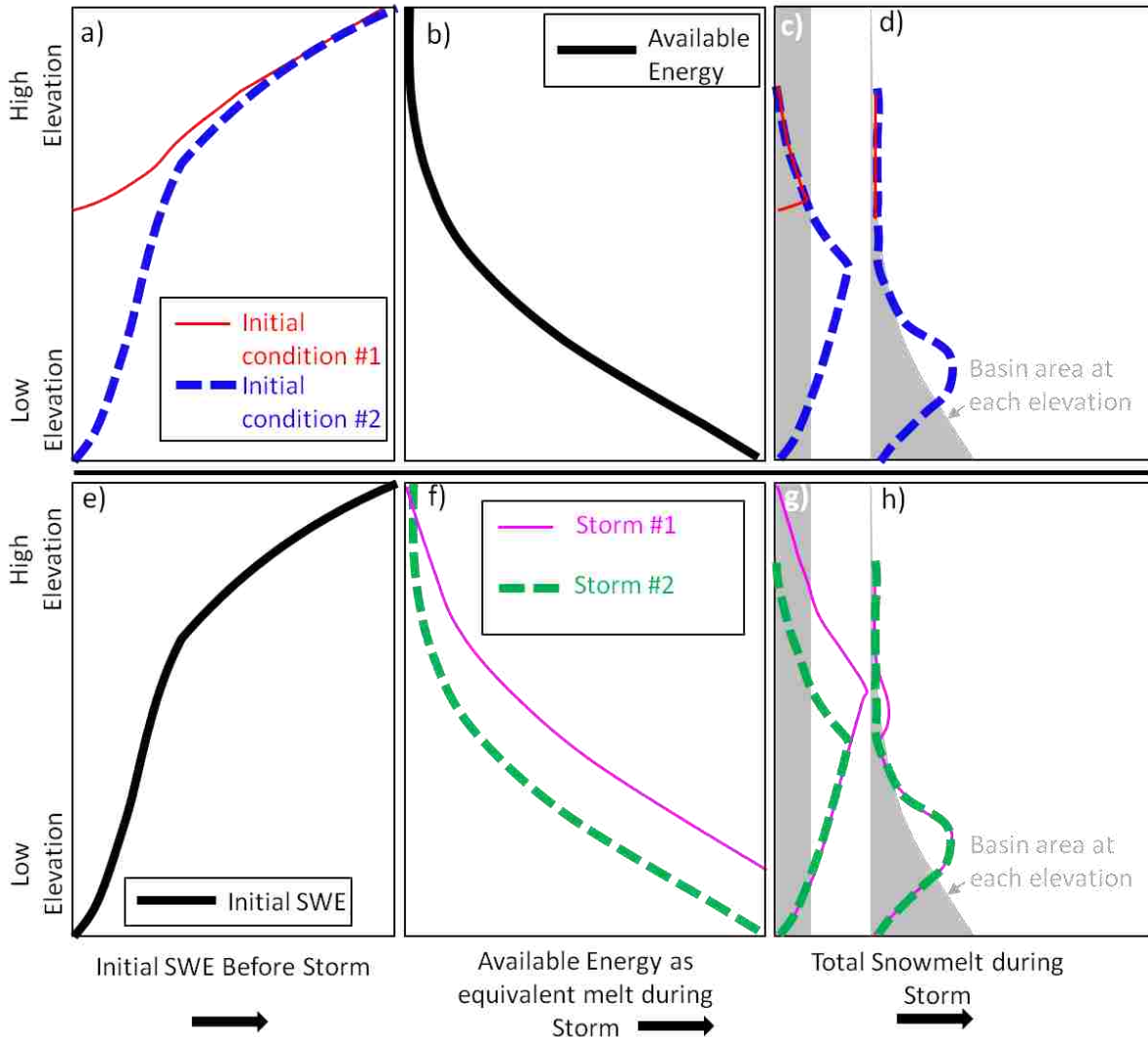


Figure 2-1. Conceptual illustration of the two fundamental controls on snowmelt during a rain-on-snow event: 1) the initial SWE and 2) the energy available for melt (in terms of equivalent melt). The impact of two different initial SWE distributions (a) prior to a ROS storm with, the same available energy for melt (b), and the resulting snowmelt given unit-area basin (c) or realistic basin hypsometry (d). Given the same initial SWE distribution (e), the impact of two different available energy distributions (f), and the resulting snowmelt given two different basin shapes (f and h). The take away hypothesis is that the elevations with the largest snowmelt volumes are produced where the available SWE intersects the potential melt energy and the largest area.

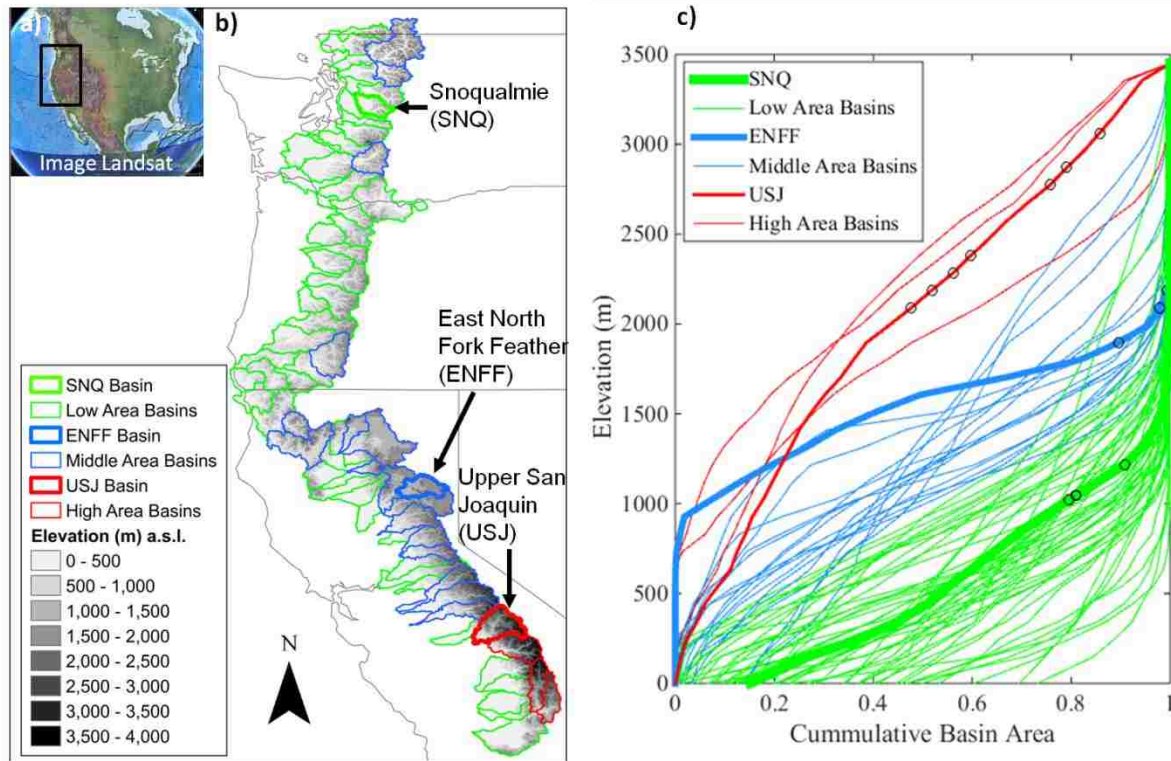


Figure 2-2. Insert (a) shows domain of study along the Cascade and Sierra Nevada ranges. (b) Outlines of westward draining HUC-8 basins categorized by their elevation where 50% of the basin area lies. Bold outlines show selected basins (SQ, ENFF and USJ) from each category used in this study. (c) Cumulative basin area with increasing elevation as a fraction of each basin. Black circles show elevations of stations with snowpillows within each basin (Listed in Table 1).

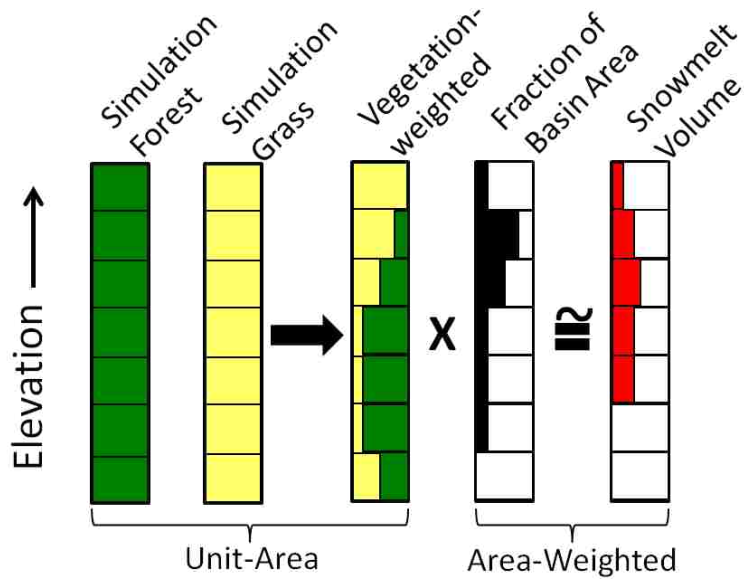


Figure 2-3. Idealized representation of study basins. Boxes indicate 100 meter elevation bins, simulated for all Forest and all Grass vegetation. Vegetation-weighted is represented as a linear combination of the model results based on observed vegetation fractions. Hypsometry is included by multiplying the model output by the area over the basin at each elevation bin to estimate the volume input.

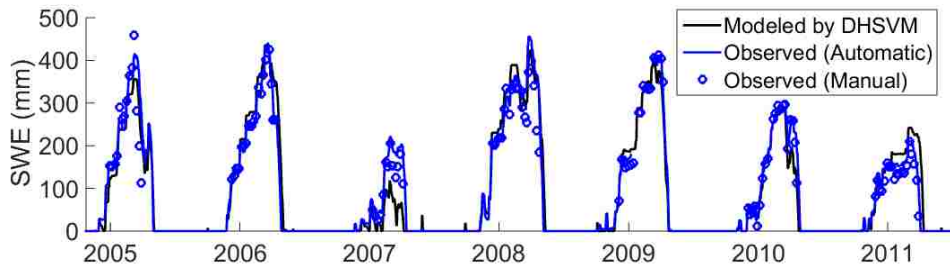


Figure 2-4. Observed and modeled (Sim 1) seasonal SWE at Col de Porte, France.

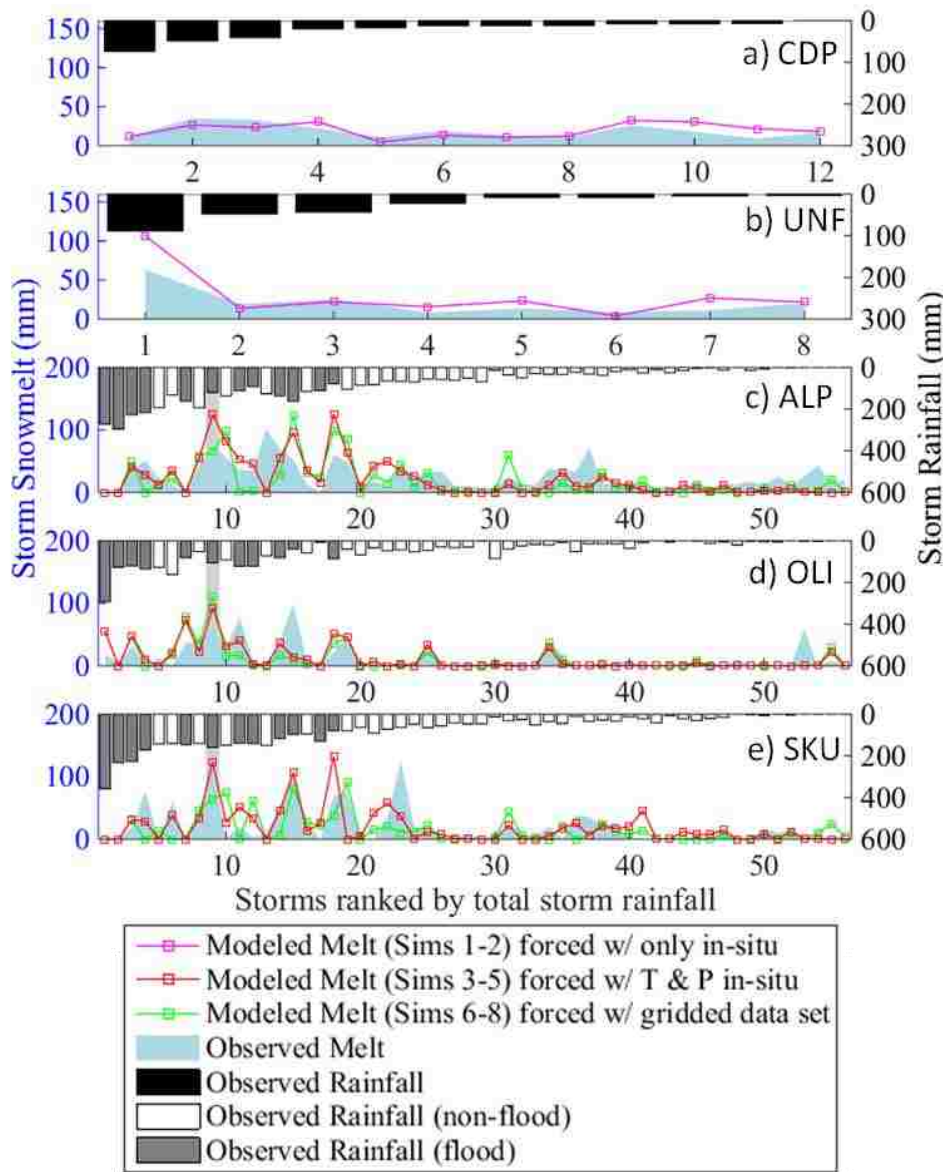


Figure 2-5. (left) Observed and modeled snowmelt total during each 3-day storm. (right) Vertical bars show the observed rain fall total during each 3-day storm that resulted in flooding (filled gray) and non-flooding (filled white), for SNQ sites only (c,d,e). Storms are ranked by storm rainfall separately at (a) CDP and (b) UNF, and by the mean storm rainfall of all three Snoqualmie basin stations: ALP, OLI, and SKU, in (c,d,e). Storm total rainfall is approximated from observed precipitation minus observed snowpillow increases, which may underestimate rainfall due to retention of liquid water in the snowpack. Note: different y-axis scales for snowmelt and rainfall. Grayed box highlights the January 19 2005 storm examined in Section 2.6.2.

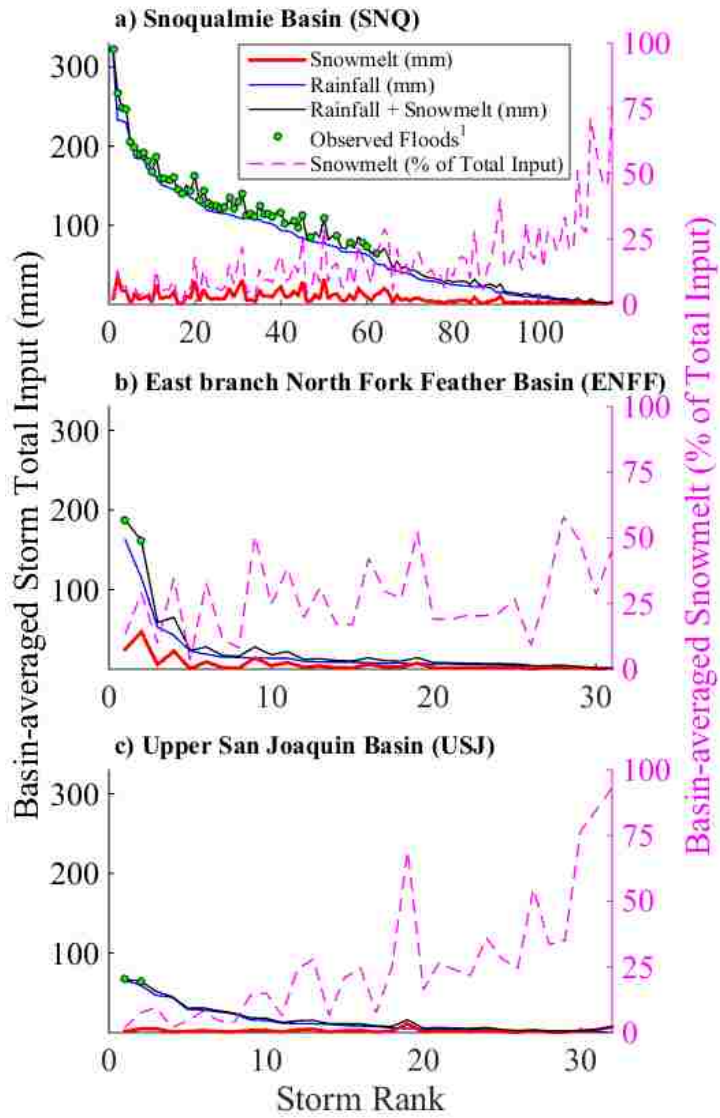


Figure 2-6. Simulated basin-average inputs of snowmelt and rainfall during all study storms (listed in Table A1 and Table S1).

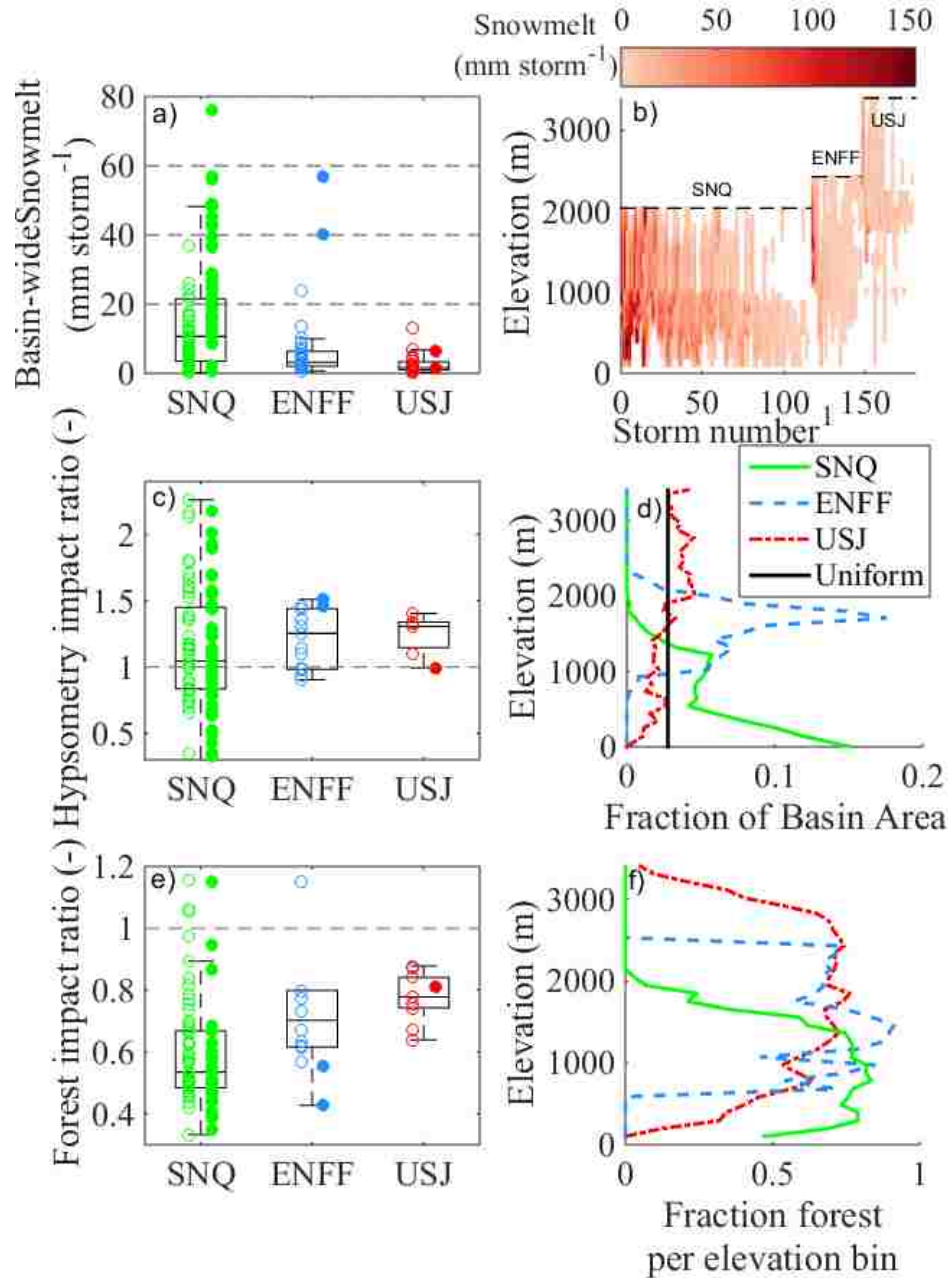


Figure 2-7. (a) Simulated basin-wide snowmelt assuming all basins have unit-weighted area and have no forest. (b) Simulated storm-total snowmelt at each basin's elevational range during each storm (1 ranked by total basin-wide snowmelt total for each basin (shown in (a))). Impacts on simulated basin-wide snowmelt in (a) from inclusion of basin hypsometry (d) are shown in (c), and forest cover (f) are shown in (e). Ratios in (c,e) are defined in text. Open circles represent ROS events without observed flooding while filled circles indicate some level of flooding was observed. Open and filled circles are offset for readability. Box plots show median, 25th and 75th percentiles, and 1.5 times the inter-quartile range. X-axis abbreviations refer to SNQ (Snoqualmie), ENFF (East North Fork Feather), and USJ (Upper San Joaquin) basins.

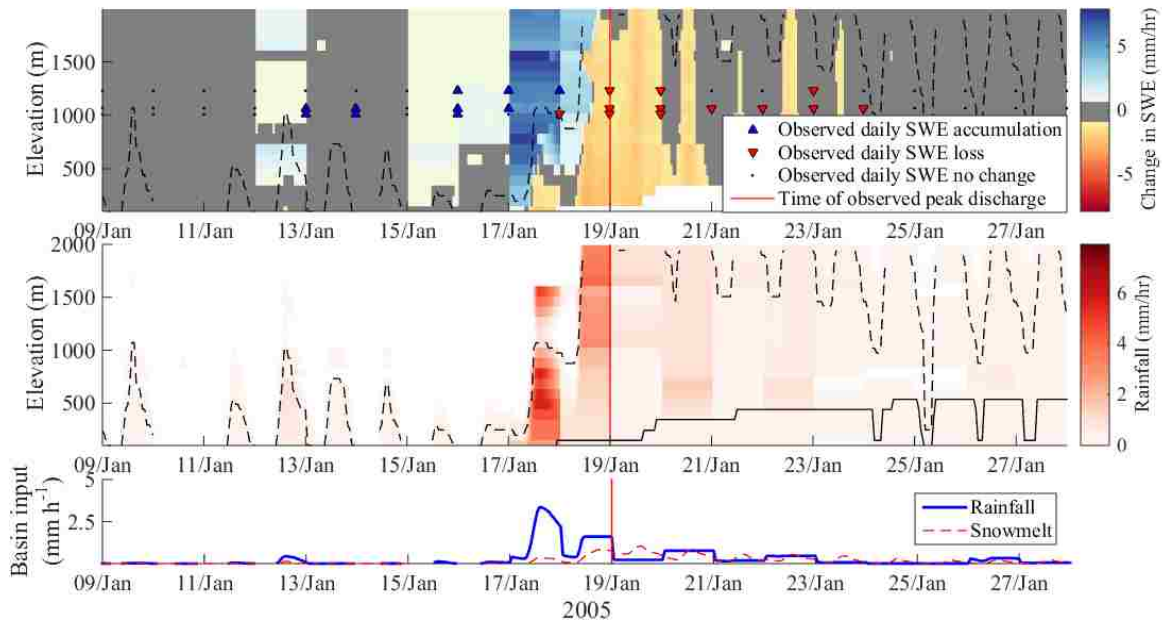


Figure 2-8. DHSVM simulation (Sim 9.1a) during the January 2005 flood of (a) hourly change in SWE, (b) hourly rainfall, and (c) basin averaged input over the SNQ basin with area- and vegetation-weighted simulations (Sim 9.1a and 9.2a). *Blue (red) triangles* pointing up (down) indicate an observed net increase (decrease) in SWE (note: triangles are placed at midnight and represent change in SWE over previous 24 hours). *Dashed and solid lines* in (a) and (b) show elevations of snowfall-level (i.e., the atmospheric rain/snow transition) and snowcover-extent (on the ground). In (a), *grey* colors show less than 0.1 mm simulated SWE change while *white* colors indicate no snow present. *Vertical red lines* show the time of peak observed stage height.

2.10. Appendix A

TABLE 2-A1. Select study storms^a

<i>Basin</i>	<i>Storm # Ranked by Rainfall</i>	<i>Storm Start^b</i>	<i>Storm End^b</i>	<i>Rain (mm)</i>	<i>Snowmelt (mm)</i>	<i>Rain + Snowmelt (mm)</i>	<i>Peak Daily discharge observed (cms)</i>	<i>Flood (Y/N)</i>
SNQ	1	11/5/2006	11/8/2006	315	7	322	1897	Y
	2	2/6/1996	2/9/1996	233	35	268	1501	Y
	3	11/27/1995	11/30/1995	232	17	249	1543	Y
	4	11/23/1990	11/26/1990	229	17	246	1504	Y
	5	10/19/2003	10/22/2003	206	0	206	708	Y
	6	11/8/1990	11/11/1990	185	13	198	1280	Y
	7	11/13/2001	11/16/2001	184	6	190	629	Y
	8	11/22/1986	11/25/1986	184	8	192	1345	Y
	9	12/3/1989	12/6/1989	171	11	181	923	Y

	10	11/11/1999	11/14/1999	165	3	168	646	Y
ENFF	1	2/16/1986	2/19/1986	163	25	187	402	Y
	2	12/31/1996	1/3/1997	115	47	162	510	Y
	3	1/11/1995	1/14/1995	53	6	59	208	N
	4	12/22/2005	12/25/2005	43	23	65	78	N
	5	11/12/2001	11/15/2001	23	1	24	3	N
	6	1/30/1995	2/2/1995	19	9	28	50	N
	7	12/27/1981	12/30/1981	15	2	17	50	N
	8	12/16/2005	12/19/2005	15	1	16	30	N
	9	2/15/1996	2/18/1996	14	14	28	40	N
	10	2/1/1991	2/4/1991	14	4	18	2	N
USJ	1	2/17/1986	2/20/1986	66	1	67	422	Y
	2	12/30/1996	1/2/1997	60	5	65	222	Y
	3	2/15/1982	2/18/1982	47	5	52	5	N
	4	1/16/2000	1/19/2000	45	1	45	3	N
	5	1/12/1995	1/15/1995	29	1	31	3	N
	6	1/14/1996	1/17/1996	28	3	31	2	N
	7	1/4/1986	1/7/1986	26	1	27	2	N
	8	2/12/2003	2/15/2003	23	1	24	3	N
	9	1/16/1999	1/19/1999	16	3	19	7	N
	10	11/18/1996	11/21/1996	15	3	18	3	N

^a Only the largest 10 storms shown here. Complete list of all storm used in this study are provided in Table S1.

^b Storm Start and End dates refer to the 3-day (72 hour) period used for analysis of basin inputs.

2.11. Appendix B

TABLE 2-B1 Statistics of SWE from point simulations.

Simulation (Sim) identifier	<i>Seasonal (Oct.-Sept)</i>					<i>ROS event (72 hours)</i>						
	Site	# Years	R ²	Mean peak bias (mm)	Mean Peak Bias (%)	# Storms	R ²	Melt RMSE (mm)	Mean Observed melt (mm)	Max Observed melt (mm)	RMSE Normalized by mean Observed melt (%)	RMSE Normalized by max of Observed melt (%)
1	CDP	10	0.9	-43	-12	12	0.4	8	19	35	40	21
2	UNF	2	0.62	-72	-25	8	0.9	17	21	63	80	27
3	ALP	15	0.6	-471	-34	56	0.3	26	26	102	98	25
4	OLI	27	0.9	175	12	56	0.4	19	14	99	137	19
5	SKU	15	0.69	-34	-4	56	0.4	24	20	124	117	19
6	ALP	15	0.67	-646	-47	56	0.2	28	26	102	106	27
7	OLI	27	0.85	341	24	56	0.3	21	14	99	152	21
8	SKU	15	0.78	234	28	56	0.2	28	20	124	137	22

2.12. Appendix C

TABLE 2-C1. Statistics of DHSVM basin snowmelt and rainfall during study events when flooding was observed.

<i>Basin (# of events)</i>	<i>Perturbation^a</i>	<i>Mean Snowmelt (mm)</i>	<i>Max Snowmelt (mm)</i>	<i>Std Snowmelt (mm)</i>	<i>Mean Snowmelt (%)</i>	<i>Max^b Snowmelt (%)</i>	<i>Mean Rainfall (mm)</i>	<i>Max^b Rainfall (mm)</i>
SNQ (N=49 events)	Default	13	35	8	10	29	130	315
	T -3.3°C	12	37	7	14	37	87	299
	T -0.8°C	13	34	8	11	32	120	315
	T +0.8°C	12	37	9	9	26	138	315
	T +3.3°C	10	41	9	7	23	155	315
	P -19%	11	30	8	10	32	105	255
	P +19%	14	39	9	9	27	154	375
	RH -25%	12	34	7	9	27	130	315
	RH +25%	14	36	9	10	30	130	315
	SW -20%	12	34	8	10	29	130	315
	SW +20%	13	36	9	10	29	130	315
	LW -25 W m-2	13	36	8	10	28	130	315
	LW +25 W m-2	12	35	9	10	30	130	315
	W -3 m s-1	11	31	7	9	21	130	315
	W -1.5 m s-1	12	33	7	9	25	130	315
	W +1.5 m s-1	13	37	9	10	32	130	315
	W +3 m s-1	14	42	10	11	35	130	315
ENFF (N=2 events)	Default	36	47	16	21	29	139	163
	T -3.3°C	12	19	10	12	18	78	84
	T -0.8°C	33	44	16	21	29	126	142
	T +0.8°C	32	46	19	19	28	150	181
	T +3.3°C	9	17	11	7	12	166	210
	P -19%	31	43	17	22	32	112	132
	P +19%	39	50	16	20	27	165	194
	RH -25%	30	39	14	18	26	139	163
	RH +25%	38	51	17	22	31	139	163
	SW -20%	35	46	15	21	29	139	163
	SW +20%	35	47	18	21	29	139	163
	LW -25 W m-2	35	43	12	21	27	139	163
	LW +25 W m-2	33	49	23	20	30	139	163
	W -3 m s-1	27	33	9	17	22	139	163
	W -1.5 m s-1	34	41	11	20	26	139	163
	W +1.5 m s-1	36	52	22	21	31	139	163

	W +3 m s-1	38	53	22	22	32	139	163
USJ	Default	3	5	3	5	7	63	66
(N=2	T -3.3°C	3	4	2	7	11	39	42
events)	T -0.8°C	3	5	3	5	9	56	58
	T +0.8°C	3	4	2	4	6	70	74
	T +3.3°C	4	6	4	4	7	96	110
	P -19%	2	4	2	5	7	51	53
	P +19%	3	6	3	4	7	75	78
	RH -25%	3	5	3	4	8	63	66
	RH +25%	3	4	2	4	7	63	66
	SW -20%	3	5	3	4	7	63	66
	SW +20%	3	5	2	5	7	63	66
	LW -25 W m-2	3	5	3	4	7	63	66
	LW +25 W m-2	3	5	2	5	7	63	66
	W -3 m s-1	3	4	2	4	7	63	66
	W -1.5 m s-1	3	4	2	4	7	63	66
	W +1.5 m s-1	3	5	2	5	7	63	66
	W +3 m s-1	3	5	3	5	8	63	66

^a Variable abbreviations defined in Table 1. Selection of meteorological uncertainty values described in Section 2.4.2.

^b Note that maximum values of snowmelt and rainfall may not refer to the same storm.

Chapter 3. A Meteorological and Snow observational data set from Snoqualmie Pass (921 m), Washington Cascades, U.S.

Note: This chapter has been published in its current form as an article in *Water Resources Research* [Wayand *et al.*, 2015a]; the only differences are in section numbering and some reference information. It is used here by permission of John Wiley and Sons.

Abstract

We introduce a quality controlled observational atmospheric, snow, and soil data set from Snoqualmie Pass, Washington, U.S.A., to enable testing of hydrometeorological and snow process representations within a rain-snow transitional climate where existing observations are sparse and limited. Continuous meteorological forcing (including air temperature, total precipitation, wind speed, specific humidity, air pressure, short- and longwave irradiance) are provided at hourly intervals for a 24-year historical period (water years 1989-2012) and at half-hourly intervals for a more-recent period (water years 2013-2015), separated based on the availability of observations. The majority of missing data were filled with biased-corrected reanalysis model values (using NLDAS). Additional observations include 40-years of snow board new snow accumulation, multiple measurements of total snow depth, and manual snow pits, while more recent years include sub-daily surface temperature, snowpack drainage, soil moisture and temperature profiles, and eddy co-variance derived turbulent heat flux. This data set is ideal for testing hypotheses about energy balance, soil and snow processes in the rain-snow transition zone. All raw, quality controlled, and filled data described in this paper is available at

the University of Washington's Research Works Archive

(<http://dx.doi.org/10.6069/H57P8W91>).

3.1. Introduction

Snow observatories [e.g., *Andreadis et al.*, 2009; *Reba et al.*, 2011; *Morin et al.*, 2012; *Landry et al.*, 2014] provide important constraints on multiple hypotheses about how snow processes can be best represented [*Clark et al.*, 2011a; *Essery et al.*, 2013]. However, existing sites that provide all required forcing and evaluation data are geographically sparse and do not equally sample the full range of snow climates, driving efforts to connect available data [*Pomeroy et al.* 2015]. In particular, the rain-snow transition zone is under-sampled, given the predominant focus on seasonal snowpacks where the majority of water supply is stored. However, the rain-snow transition zone is important hydrologically (e.g. in the W. Sierra Nevada, [*Rice et al.* 2011; *Biggs and Whitaker*, 2012]) and climatologically [*Mote et al.*, 2005; *Nolin and Daly*, 2006; *Vano*, 2015], and likely provides an ideal climate for model evaluation, given that the typically warmer and shallower snowpack is highly sensitive to errors in meteorological forcing [*Wayand et al.*, 2013; *Lapo et al.*, 2015].

We present an atmospheric, snow, and soil data set measured at the Snoqualmie Pass (SNQ) snow study site, located at 921 m a.s.l. within the rain-snow transitional climate of the Central Washington Cascades at N 47.424883, W 121.413893 (Figure 3-1). Snoqualmie Pass is part of the larger Stampede Gap in the Cascade range, resulting in the SNQ site being influenced by both maritime air masses from the west and dry continental cold air intrusions from Eastern Washington [*Steenburgh et al.*, 1997]. This unique environment makes observation and

simulation of snow pack dynamics challenging. A time-lapse video is provided in Movie S1 to visualize the site and snow climate during the 2014 water year.

This data set is introduced by first describing the Snoqualmie pass region and study site in Section 3.2. All observations of atmospheric, snow and soil data are discussed in Section 3.3. Quality control methods are defined in Section 3.4, and methods used to fill missing data for the continuous snow model forcing are defined in Section 3.5. An example of using historical snow board data to constrain parameterizations of new-snow density is provided in Section 3.6, and study conclusions are summarized in Section 3.7.

3.2. Snoqualmie Pass site description

Snoqualmie Pass has been a critical transportation corridor to Washington State commerce from before the westward expansion of settlers [*Prater*, 1981] until present day. For example, a four day road closure in January 2008 cost an estimated \$27.89 million to the state economy [*Barbara et al.*, 2008]. Peak annual snow depths average 2.6 m at pass level, and frequent avalanche cycles [*Stimberis and Rubin*, 2011b] necessitate the need for snowpack observations and avalanche control work.

In 1931, manual snow observations were begun by the Washington Department of Transportation (WSDOT) at the study site (Figure 3-2) to provide daily avalanche information for managing the highway, share data with the North West Avalanche Center (NWAC, established in 1976), and to support nearby ski operations. Of great importance are the daily snow board measurements of accumulated SWE, which provide a daily proxy for partition phase. A weather station (Tower A, Figure 3-2) was installed in 1980 to monitor the pass conditions, with frequent updates and additions over the years. Most notably, the switch to hourly data in

1988 provided the basic observations required to drive a temperature index snow model (i.e. air temperature and precipitation), with relative humidity and wind speed measurements added in November 2002. In October 2012, intensive meteorological and snow observations were installed on the existing NOAA tower (Tower B, Figure 3-2) and maintained by the University of Washington to provide a comprehensive data set to test snow models (water years 2013 to 2015).

The site consists of an approximately 900 m² grass clearing bordered by coniferous forest to the northwest, northeast and southeast, with 20 m of open buffer space to the southwest (insert, Figure 3-2). A parking lot and building to the southwest of the buffer space are downwind of the site (under prevailing wind conditions from the northeast) insuring a minimal impact on measurements. Site vegetation consists of approximately 5 cm tall grass, which is trimmed annually at the end of the growing season (late September). Despite being located 100 m from the highway (Figure 3-1c), the heavily forested area in between buffers any impact from the road. Finally, the accessibility of the site increases observation breadth and quality (i.e. daily snow observations, AC power for turbulent heat flux measurements, an internet connection for monitoring instruments, etc.).

3.3. Data Descriptions

All levels of data (raw, quality controlled, and filled) are made available so that users may select which level of processing is most appropriate for their needs. Table 3-1 details atmospheric measurements, and Table 3-2 describes all snow and soil measurements. We separated the data sets into two periods: a historical data set from water years 1989 to 2012, and a shorter, but more complete data set, from water years 2013 to 2015. Availability of data for both periods is illustrated in Figure 3-3, where missing data were filled from alternative sources, in particular,

bias-corrected values from the nearest National Land Data Assimilation Systems (NLDAS) [Cosgrove, 2003] model grid cell, as described in Section 3.5. While a complete history of instrument metadata are not available for the historical period, WSDOT employees monitored instruments daily for issues and replaced sensors when values deviated substantially from nearby stations. Known replacements and lengths of record for each instrument are detailed in Tables 1 and 2. Each measured variable is described below.

3.3.1. Meteorological measurements

Air temperature and relative/specific humidity

Air temperature and relative humidity sensors within naturally aspirated radiation shields were installed at 4 m above ground level during the historic period and at 3.8 m and 6.4 m during the more recent period (See Table 3-1 for exact dates). Specific humidity was derived from the equation as defined in *Glickman* (2000), with saturated vapor pressure estimated from the Magnus Teten equation [Murray, 1967] using in-situ observations of air temperature, relative humidity, and air pressure.

Precipitation

Total precipitation (including solid and liquid phases) was measured with a heated rain gauge with a single Alter windshield. Undercatch of snowfall was quantified at -14%, by comparing the daily accumulated gauge precipitation to the daily accumulated SWE (snow board measurements described in section 3.3.2), for days when only snowfall occurred (maximum air temperature was below -1°C , $N=863$). However, the majority of observed SWE (86%) accumulates on days with maximum air temperatures *above* -1°C , where undercatch errors are expected to be less, thus the

annual undercatch error is likely lower than -14%. A correction for missed snowfall was made for the *filled* data set as described in section 3.5, but no direct correction for rainfall undercatch was made.

Wind speed

Wind speed was measured at 7.15 m using an un-heated cup anemometer with an instrument accuracy of 2%. Observed wind speeds were relatively low at the site, averaging 0.34 m s^{-1} , and may not represent higher wind speeds or wind directions at other locations throughout the pass. At the site, a strong diurnal cycle in wind speed was observed, likely driven by non-uniform solar heating/cooling of the adjacent valleys. The dominant wind speed direction was from the north-east (~ 55 degrees true north) as measured by the sonic anemometer (Table 3-1).

Air pressure

A barometer was installed in 2008 to provide 15 min measurements of air pressure with an instrument accuracy of $\pm 4 \text{ mb}$.

Short- and longwave irradiance

Shortwave ($0.3\text{-}2.8 \text{ }\mu\text{m}$) and longwave ($4.5 \text{ to } 42 \text{ }\mu\text{m}$) irradiance (incoming and outgoing) were measured with a 4-component radiometer, at a height of 6.6 m on tower B, situated in the center of the approximately 900 m^2 grass clearing. Calibration has been performed annually to insure values remain within instrument uncertainty bounds. This calibration, and additional modeling experiments, resulted in the identification of critical errors in a Campbell Scientific program that calculated longwave values [Lundquist et al., 2015a]. The longwave measurements presented

here are critically important because no other longwave observations are currently available within Washington State, to the authors' knowledge.

Accumulation of ice, snow and liquid on the sensor domes was dealt with in two ways. A heater/ventilator provided moderate energy to remove condensation, deposition or light snow. However, the heater/ventilator was found to be incapable of keeping the sensor domes clear in the heavy snow events of the Pacific Northwest maritime climate. The majority of the heavy accumulated snowfall was removed by WSDOT employees, who cleared the dome at 6:00 am PST using a broom. Remaining periods when sensors remained covered were flagged using time lapse cameras pointing at the radiometer's upper sensors (described in Section 3.4).

Hemispherical photos taken from ground level indicate that terrain to the south and fir trees to the south-east shade the snow surface (also see time lapse photos), yet have only minor impact on the incoming solar radiation at the instrument's height.

Sensible and latent heat fluxes

Sensible and latent heat fluxes were measured using the eddy covariance (EC) method. 20 Hz measurements of wind speed, air temperature and direction were made with a sonic anemometer, and H₂O concentrations were measured with a gas analyzer. Both instruments were mounted on a horizontal boom, with height on the tower manually adjusted through the winter to remain approximately 2 meters above the snow surface. Fluxes were calculated following methods by *Thomas et al.* [2009] using an averaging period of 10 min, which was then aggregated to 30 min. Processing and quality control are further detailed in section 3.4.

3.3.2. Snow and soil measurements

Total snow depth

Total snow depth was measured by both an automated acoustic sensor and manually from a snow stake. The acoustic sensor measured values were corrected for changes in the speed of sound using air temperature observed by the internal Judd temperature sensor, following the Judd Communications manual, and smoothed to remove inherent noise with a 24 hour sliding window. Accuracy of the automated total snowdepth is reported as ± 26 mm, but experience has shown the range could likely be ± 60 mm. Uncertainty of manual observations every 6:00 am PST was estimated at ± 25 mm, as the snow stake has increments of 50 mm.

New 24-hour snow depth and SWE accumulation

Throughout winter months (typically November to May) since 1974, WSDOT avalanche crew measure and then clear, a 0.22 m^2 (45 cm x 48 cm) snow board (see Figure 3-2) daily at approximately 6:00 am PST. Accumulated snow depth is measured from the graduated snow board stake. SWE is sampled with snow cutter (289.51 cm^2 area) and weighed with a scale. Additional measurements relevant for monitoring of avalanche conditions are also performed. Prior to 2000, historical records were transcribed from paper copies by hand twice for quality-control checks. It should be pointed out that snow board data should not be used to diagnose partitioning trends, as observations prior to 2000 predominantly sampled snowier days, while more continuous records exists after 2000. Starting in October 2004, an automated snow depth sensor was installed over a secondary snow board, providing hourly observations of snow accumulation between each 6:00 am clearing of the snow boards. The availability of these

observations is only possible through the dedicated work by many avalanche crews and represents an impressive continuous record of new snow fall.

Snow water equivalent

Total snow water equivalent was measured manually during site visits throughout the 2014-2015 winter from full profile snow pits (detailed below). No automated observations of total SWE (i.e. a snow pillow) were available in-situ, with the nearest measurement being at the Olallie Meadows NRCS SnoTel station, located 6 km to the southwest at a higher elevation (1228 m).

Snowpit profiles (Layer height, density, and temperature)

Full profile snowpits were performed throughout the winter months at the south-east corner of the study area (Figure 3-2). A 250 cc density cutter and handheld thermometers, were used to measure layered snow density and temperature. Four full snowpits were taken during the 2015 water year.

Surface (snow and soil) temperature

Surface (snow or soil) temperature was measured with an infrared radiometer fixed to tower B, providing a view of the surface under the radiometer (without any of the tower or surrounding trees within the footprint). A second identical instrument was installed on the northeast side of tower B for the 2014 water year. Instruments were mounted at a height of 6.5 m, which provided sampling areas of approximately 36 m² when no snow was present. The instrument accuracy of both sensors was $\pm 0.5^{\circ}\text{C}$ across the full range of surface temperatures at SNQ (-30 to 45 °C).

However, values up to 1.5°C above 0°C during complete snow covered periods were observed

during melt conditions. These values had no physical explanation, thus we suggest the total accuracy of the sensors is more likely $\pm 1.5^{\circ}\text{C}$.

Surface (snow and soil) albedo

The surface albedo was calculated from observations of upward and downward fluxes of shortwave (0.3-2.8 μm) irradiance. Shading of the snow surface from trees to the south-east and terrain to the south had the largest impact on calculated albedo during November to January months and during sunrise and sunset. Time-lapse images (see Section 3.3.2) indicated that 14:00 PST (GMT -8) was the optimal hour for calculating a representative albedo because it had the highest azimuth angle and minimum surface shading.

Time-lapse photography

Four time-lapse cameras that include views of the tower, selected instruments, and surrounding snowpack were installed starting in March of 2013 (subsequent installations in November 2013, November 2014, and January 2014). Three-hourly and hourly images during daylight hours provided a qualitative record of storm and snowpack events that were useful for quality controlling observations. In particular, the time-lapse camera facing the top of the radiometer was instrumental in detecting periods when snow fully or partially covered the measurement dome. In addition, the cameras facing below the radiometer, provided a qualitative measure of snow surface roughness, the formation of preferential flow paths of liquid water at the surface, and quantified snowcover fraction of viewable areas. Camera views also included adjacent forest canopies, which provide a measure of snow interception and unloading timing [*i.e. Parajka et al., 2011*] for second-growth Mountain Hemlock and Sliver Fir.

Snowpack outflow

Snowpack outflow (including percolating rainfall and snowmelt) was measured using a lysimeter located on level ground in the northwest corner of the study plot (insert, Figure 3-2). The lysimeter consists of a 9.29 m² (10 ft by 10 ft) concrete pad sloped toward a central drainage tube to a tipping bucket. The lysimeter provides an accurate measure of the timing of liquid water exiting the snowpack, but magnitudes of outflow should be used with caution as lateral flow within the snowpack may introduce biases.

Soil pit (ground heat flux, soil temperature, and soil moisture)

In July of 2013, a 0.5 m deep soil pit was installed 5.3 m northeast of tower B (Figure 3-2). Soils at the site consist of poorly sorted gravely-silt down to 0.8 m, where a layer of broken concrete exists that prevented a deeper soil pit. Soil samples removed at depths of 0-9.5 cm and 20-27 cm had bulk densities of 1.18 g cm⁻³ and 1.55 g cm⁻³, respectively. Soil temperature probes were placed at 3, 11, 21, and 41 cm below the surface (although the sensor at 11 cm failed shortly after installation). Soil moisture probes were placed at 3, 11, 21, and 37 cm.

Three self-calibrating ground heat flux plates were installed 7 cm below the surface. The sensors execute a self-calibration procedure daily to account for temporal changes in the heat capacity of the soil. All observations biased by the heating elements during self-calibration procedure were removed. For the self-calibration procedure to be successful, the sensors must be located in homogenous media which precluded their installation at or just below the ground surface. Heat flux at the ground surface was then estimated using the heat flux at a 7 cm depth in conjunction with changes in the internal heat of the top layer of the soil, which is calculated from

the 3 cm depth soil temperature and water content observations along with the bulk density of the soil. The estimated surface heat fluxes had a low signal-to-noise ratio during snow covered periods, thus use of the heat flux at 7 cm depth is recommended when snow is present.

3.4. Quality Control

All observed data were automatically quality controlled for unrealistic outliers, constant values, and extreme jumps following *Meek and Hatfield* (1994). All values were carefully inspected for erroneous data by visually examining each variable record. Additional manual quality control was performed for individual observations as needed.

Radiation observations are subject to errors when the radiometer is covered by snow or ice. Hourly images from timelapse cameras installed March 2013, which include views of the radiometer dome, were examined manually to remove periods where snow accumulation would bias measured downward fluxes. Prior to this date, values were removed when the incoming shortwave radiation was less than the outgoing shortwave radiation, and during periods of heavy precipitation in sub-freezing conditions.

Timesteps when the radiometer or snow surface was shaded by terrain or canopy were not removed, as the focus of this data set is to provide forcing for simulation of local snowpack conditions that are impacted by minimal shading. However, we strongly recommend shaded time steps be removed before extrapolating radiation values to other nearby locations, in order to prevent propagation of shading errors.

The best method to measure and quality control turbulent heat fluxes over snow in complex terrain (i.e. a forest gap within a mountain pass) is an active area of research [*Reba et*

al., 2009], thus the quality control methods applied here erred on the side of caution by applying high thresholds for quality. We followed methods by *Thomas et al.* [see their Figure A1, 2009]. First, all 20 Hz EC measurements were screened for plausible limits and then de-spiked using a 300 s moving window [Vickers and Mahrt, 1997]. Lags between H₂O and wind speed due to the 15 cm distance between sensors were corrected for using the mean correlated lag. The EC instrument boom was oriented into the prevailing wind direction at 55°, thus all wind speeds originating behind the tower (212.5° to 257.5°) were removed. Observed wind speeds were then rotated to minimize the mean vertical velocity using 3D-coordinate rotation. Finally all periods with observed precipitation were removed because accumulating rain and ice on the acoustic anemometer sensor heads biased wind speed and temperature measurements. To facilitate future processing techniques, the raw 20 Hz measurements are also provided.

3.5. Meteorological forcing data sets

Both historical (hourly) and recent (half-hourly) data sets contained missing values due to the availability of observations or removal of erroneous data (Figure 3-3). In order to provide a continuous meteorological forcing time series as required by hydrological models, missing values were filled using the best available data source. When duplicate in-situ observations existed (air temperature or relative humidity during the Recent period), the 6.35 m (Tower B) sensors were used as the primary data source, otherwise the 4 m (Tower A) sensors were used. Remaining missing time steps were filled using the following sources: interpolation of 1-24 hour gaps [Liston and Elder, 2006], then bias-corrected values from the nearest National Land Data Assimilation Systems (NLDAS) [Cosgrove, 2003] model grid cell center (47.4380, -121.4380, 1126 m). All NLDAS surface output were bias corrected using the monthly mean difference, or

ratio, between NLDAS values and observations at SNQ, except for shortwave irradiance. Monthly adjustments were calculated separately for each historic and more recent period (see Table S1 in *Wayand et al.*, 2015a), and incorporate both the elevational difference between the NLDAS grid cell and the SNQ site (921 m) as well as monthly biases in NLDAS model values. Correlations between hourly NLDAS values and surface observations were generally high (0.86-0.97), except for precipitation (0.4), wind speed (0.21), and long-wave irradiance (0.65). A full analysis of NLDAS values compared to surface observations at SNQ is provided in Figure S1 of *Wayand et al.*, 2015a. We acknowledge the limitations of using a large ($1/8^{\text{th}}$ degree) atmospheric model to fill missing surface observations in complex terrain, but it was the best available source for this location of the historical period. Further, we provide both the raw and quality controlled data sets in the likely event that more accurate reanalysis products become available in the future.

3.5.1. Recent: 10/1/2012 – 5/11/2015

Within the more recent period, the radiation variables contained the most missing time steps (29%) due to snow or ice accumulation on the radiometer dome. Data losses consistent across all variables are typically due to power outages that persisted longer than the in-situ battery capacity. Short 1-24 hour missing periods of short- and longwave irradiance data were first interpolated following [*Liston and Elder*, 2006]. Periods of missing shortwave data longer than 24 hours were filled from instantaneous hourly NLDAS model values, which were disaggregated to 30 min time steps using estimated transmissivity. Although NLDAS longwave values have been found to be biased [*Mitchell*, 2004], they were better correlated to SNQ observations ($R^2 = 0.65$) than existing empirical methods ($R^2 = 0.24$) [e.g. *Prata*, 1996; *Dilley and O'Brien*, 1998;

Flerchinger et al., 2009], and therefore NLDAS values were used here. All remaining missing periods for air temperature (1.1%), relative humidity (1.1%), precipitation (1.3%), wind speed (1.2%), and air pressure (1.3%), were filled using NLDAS values that were corrected using monthly biases calculated by comparing NLDAS values with observations (see Table S1a in *Wayand et al.*, 2015a). A full analysis of NLDAS values compared to surface observations at SNQ is provided in Figure S1. An additional correction was made to the daily observed precipitation totals: if the accumulated 24 hour SWE on the snow board exceeded the 24 hour accumulation in the heated rain gauge, the difference was added to the daily precipitation by distributing it uniformly over timesteps when precipitation occurred. This resulted in the addition of an average of 80 mm per water year between the period of 2012 to 2015.

3.5.2. Historic: 10/1/1989 – 9/30/2012

No observations of radiation were available during this period, thus these two variables were taken directly from NLDAS model values. For longwave irradiance, the same monthly bias corrections from the recent period were applied to the historical period. NLDAS shortwave values were not bias corrected or adjusted to include local shading. For the remaining forcing variables, missing observed values were filled with NLDAS values; bias corrected using the difference or ratio between NLDAS values and observations during the historical period (see Table S1b in *Wayand et al.*, 2015a). Additional analysis of NLDAS values compared to available surface observations at SNQ is provided in Figure S1. Daily precipitation totals were adjusted using the daily observations of accumulated SWE as described above, which resulted in the addition of approximately 148 mm per water year over the 1989 to 2012 period. Daily errors

were not distributed uniformly, but were larger during water years 1990 and 1997 through 2000. The reason(s) for these larger errors during select years is not known.

3.6. Snow and soil measurements

The relationship between average daily air temperature and the accumulated snow density over the previous 24 hour period is shown in Figure 3-4. Although some minor compaction of snow depth occurs since the last time the board was cleared (i.e. from metamorphism, overburden, or melting), these snow board observations provide the best available measurements of new snow density during this time period. Over 40 years (N = 2582 days), the observed density at SNQ averaged 130 kg m^{-3} , which is similar to reported values from previous studies [*Potter*, 1965; *Currie* 1947; *LaChapelle* 1962; *Judson and Doesken*, 2002] and common rules of thumb used in operations [i.e. 100 kg m^{-3} , *Roebber et al.*, 2003]. Existing forms of parameterizations [*Anderson*, 1976; *Hedstrom and Pomeroy*, 1998; *Boone*, 2002; *Oleson et al.*, 2010] capture the general observed relationship of higher densities with warmer air temperatures but fail to explain the large scatter of observed new snow density. Some of the observed scatter may be due to the 24-hr sampling intervals and surface compaction occurring in the time elapsed between snowfall and snow board measurement. Nonetheless, the choice of parameterization, and resulting errors, will have the largest impact on water resources during temperatures near 0°C , when the bulk of new SWE accumulates at this site (Figure 3-4b).

3.7. Conclusions

We introduced a point atmospheric and hydrologic data set that is composed of 40 years of historical and 3 years of intensive recent observations. The location of the Snoqualmie pass site within the rain-snow transitional zone poses a challenge to automated measurements, yet,

through a partnership with WSDOT and dedicated University of Washington students, we maintained good quality measurements. In particular, the historical observations of 24-hour new snowfall and recent observations of turbulent heat fluxes have not been previously made available to the snow modeling community within this snow climate. In addition, we have installed and maintained the only longwave irradiance observations within the state of Washington since September 2013. Finally, we provided an example of how historical observations could help constrain parameterizations of new snowfall density. Although we provided forcing and evaluation data with water resource questions in mind, the uses of this data set extend beyond the water resources community to avalanche [*Stimberis and Rubin, 2011b*] and mountain meteorological research [*Lundquist et al., 2015b*].

3.8. Tables

Table 3-1. Meteorological observations.

<u>Variable</u>	<u>Tower/Location</u>	<u>Make/Model</u>	<u>Temporal average</u> [instantaneous] (sample rate)	<u>Spatial sample area</u>	<u>Instrument accuracy</u> (estimated accuracy)	<u>Instrument height above ground</u>	<u>Date Range</u>
Air Temperature	A	Vaisala HMP w/ naturally aspirated Gill radiation shield	(15 min) (60 min) before 2006	point	$\pm 0.45^{\circ}\text{C}$ (-40° to +60°C) $\pm 1^{\circ}\text{C}$ before 2003	4 m	1989-2015
-	B	Vaisala HMP60 w/ naturally aspirated Gill radiation shield	10 min (10 s)	point	$\pm 0.6^{\circ}\text{C}$ (-40° to +60°C)	6.35 m	2012-2015
-	B	Campbell, T107 w/ naturally aspirated Gill radiation shield	10 min (10 s)	point	$\pm 0.4^{\circ}\text{C}$ (-24° to 48°C) $\pm 0.9^{\circ}\text{C}$ (-35° to 50°C)	3.82 m	2013-2015
Relative Humidity	A	Vaisala HMP w/ naturally aspirated Gill radiation shield	(15 min) (60 min) before 2006	point	$\pm 5\%$ (0 to 90%) $\pm 7\%$ (90 to 100%) @ -	4 m	2003-2015

					40° to +40°C		
Relative Humidity	B	Vaisala HMP 60 w/ naturally aspirated Gill radiation shield	10 min (10 s)	point	±5% (0 to 90%) ±7% (90 to 100%) @ -40° to +40°C	6.35 m	2012-2015
Precipitation	A	Met One 385, heated rain gauge w/ single Alter windshield	15 min (tip)	12 in diameter	±0.5% (<1.27 cm hr ⁻¹) ±2.0% (<7.62 cm hr ⁻¹)	6.5 m	2010-2015
	A	Qualimetrics 6018, heated rain gauge w/ single Alter windshield	1 hour (tip)	12 in diameter	±0.5% (<12.7 cm hr ⁻¹)	6.5 m	1993-2010
	A	Sierra Misco tipping bucket, heated rain gauge w/ single Alter windshield	1 hour (tip)	12 in diameter	±4.0% (<15.2 cm hr ⁻¹)	6.5 m	1989-1993

Wind speed	A	Electric Speed Indicator co. 3-cup anemometer F420C	15 min (10 s). 60 min (60 min) before 2006.	point	2%	7.15 m	2003-2015
Air Pressure	A	Campbell Scientific barometer 105	(15 min).	point	±4 mb @ -20° to 45°C	4 m	2008-2015
Shortwave irradiance (incoming and outgoing)	B	Kipp and Zonen CNR4	10 min (10 s)	Incoming (180° view angle) Outgoing (150° view angle)	± 10% for daily totals	6.6 m	2013-2015
Longwave irradiance (incoming and outgoing)	B	Kipp and Zonen CNR4	10 min (10 s)	Incoming (point @ 180° view angle). Outgoing (24.6 m radius @150° view angle)	< 10% for daily totals	6.6 m	2013-2015
Sensible	B	Campbell	30 min (20	variable	Accuracy of	Variable	2013-2015

Heat Flux		Scientific Sonic anemometer CSAT3	Hz)	foot print	flux processing	(~ 2 m above snow surface)	
Latent Heat Flux	B	Li-Cor CO ₂ /H ₂ O Gas analyzer Li-7200	30 min (20 Hz)	variable foot print	(1-2%) Accuracy of flux processing	Variable (~ 2 m above snow surface)	2013-2015

Table 3-2. Snow and soil observations.

<u>Variable</u>	<u>Tower/Location</u>	<u>Make/Model</u>	<u>Temporal average</u> <u>[instantaneous]</u> <u>(sample rate)</u>	<u>Spatial sample area</u>	<u>Instrument accuracy</u> <u>(estimated accuracy)</u>	<u>Instrument height above ground</u>	<u>Date Range</u>
Total Snow Depth	A	Acoustic sensor Judd Ultrasonic	15 min (1 min)	16 m ² (22° view angle, no snow)	±26 mm (±60 mm)	5.5 m	1989-2015
Total Snow Depth	Center of clearing	Manual Snow Stake	Daily	point	(±25 mm)	N/A	1975-2015
New (24 hr) Snow Depth	Near A	Manual Snow Board	Daily	point	(10 mm)	N/A	1975-2015

New (24 hr) Snow Depth	Near A	Acoustic sensor Judd Ultrasonic	15 min (1 min)	0.22 m ²	±10 mm	1.1 m	2004-2015
New (24 hr) Snow SWE	Near A	Manual Snow Board	Daily	0.22 m ²	Unknown	N/A	1975-2015
Snow profile (Depth, Density, SWE)	Southern corner of clearing (See insert Figure 3-2)	Snow metrics Ruler, snow cutter, scale	~monthly	250 cc	(± 10%)	~5 cm layers	2015
Surface Temperature	B	Infrared Radiometer (8-14 μm). Campbell Scientific- Apogee SI-111	10 min (10 sec)	~36 m ² (44° view angle, 30° off nadir, at 6.5 m, no snow)	±0.2°C @ -10° to 65°C ±0.5°C @ -40° to 70°C (±1.5°C)	6.5 m	2013-2015
Surface Temperature	B	Infrared Radiometer (8-14 μm). Campbell Scientific - Apogee SI-111	10 min (10 sec)	~36 m ² (44° view angle, 30° off nadir, at 6.5 m, no snow)	±0.2°C @ -10° to 65°C ±0.5°C @ -40° to 70°C (±1.5°C)	6.5 m	2014
Snow Temperature	Southern corner of clearing (See insert Figure 3-	Hand held thermometer probe. Cooper	~monthly	point	±1°C (-40° to 232°C),	~10 cm layers	2015

profile	2)	DFP450W (digital), Tel-Tru (analog)			±1% (-50° to 25°C)		
Pack total Outflow	Northwest corner of clearing (See insert Figure 3-2)	Lysimeter. Unidata tipping bucket 6506	5 min (tip)	9.29 m ² (10 ft by 10 ft)	^a	0 m	2001-2015
Soil Temperature profile	Center of clearing (See insert Figure 3-2)	Temperature probes. Campbell Scientific, TCAV And T107	10 min (10 sec)	point	±0.4°C (-24° to 48°C) ±0.9°C (-35° to 50°C)	-3 cm, -21 cm, -41cm	2014-2015
Soil Moisture profile	Center of clearing (See insert Figure 3-2)	Water content reflectometers. Campbell Scientific, CS616	10 min (10 sec)	2 cm avg.	±2.5% VWC	-3 cm, -11 cm, -21 cm, -37 cm	2014-2015
Ground Heat Flux	Center of clearing (See insert Figure 3-2)	Self-Calibrating Soil Heat Flux Plates. Campbell Scientific, HFP01SC	10 min (10 sec)	Avg. of three 50 cm ² sensors	±3%	-7 cm	2014-2015
Albedo	B	4-component Radiometer.	10 min (10 sec)	24.6 m radius	±10 %	6.6 m	2013-2015

		Campbell Scientific, CRN4		around tower, no snow	incoming ±10 % outgoing (±20 % total)		
Snow covered Area	B and pole to south of Tower B	Four timelapse cameras. Wingscape	[1 hour and 3 hour]	Camera view dependent	N/A	6.7 m, 6.5 m, 5.5 m	2013-2015

^a Lysimeter magnitudes should be used with caution, as lateral flow within the snowpack can cause absolute value biases. Unidata tipping gauge did not specify an instrument uncertainty.

3.9. Figures

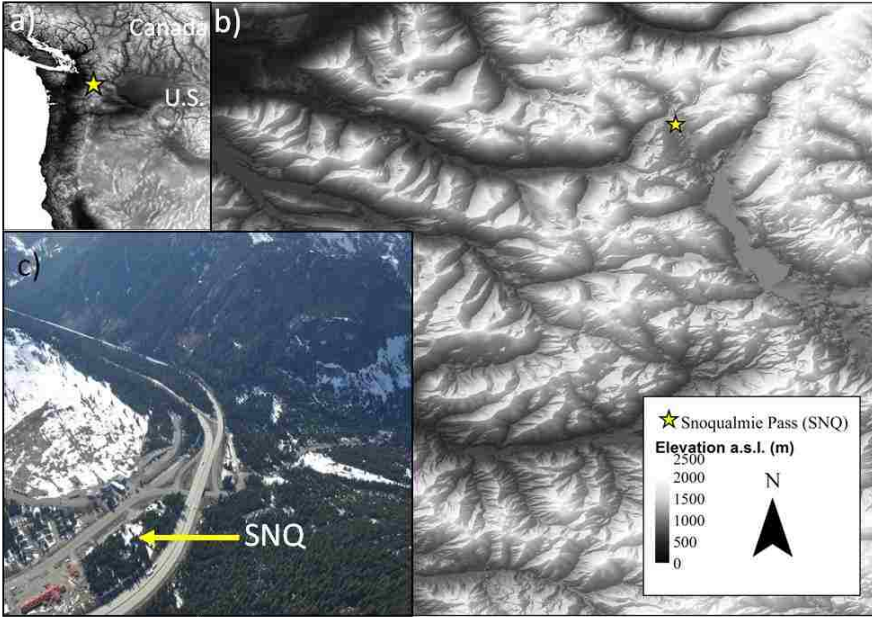


Figure 3-1. (a,b) The Snoqualmie (SNQ) pass snow study site located within the Washington Cascades, U.S, at 917 meters a.s.l. (+47.424883, -121.413893). (c) Airborne photo looking northwest towards the SNQ site with Interstate 90 at center.

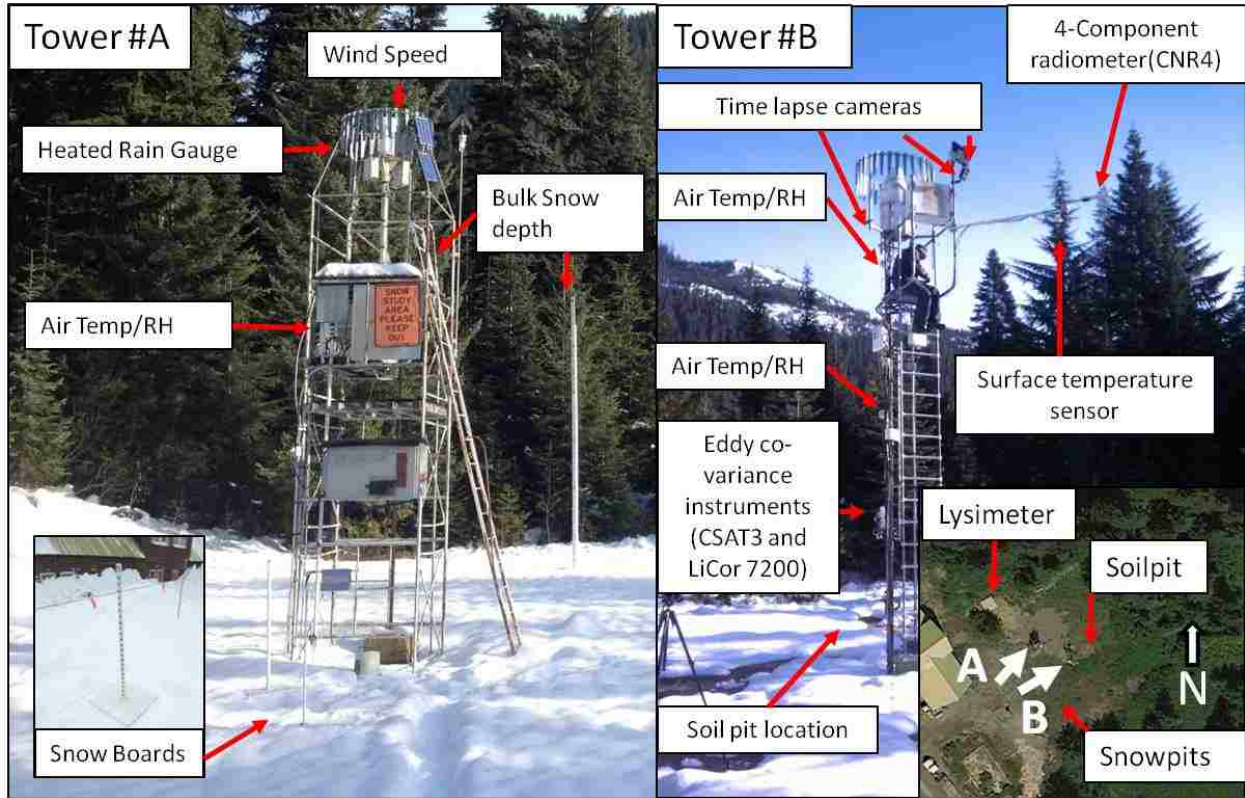


Figure 3-2. Observed variables from tower A and B, located within the study site area shown in insert. *White arrows* within the insert represent approximate viewing angle of towers A and B.

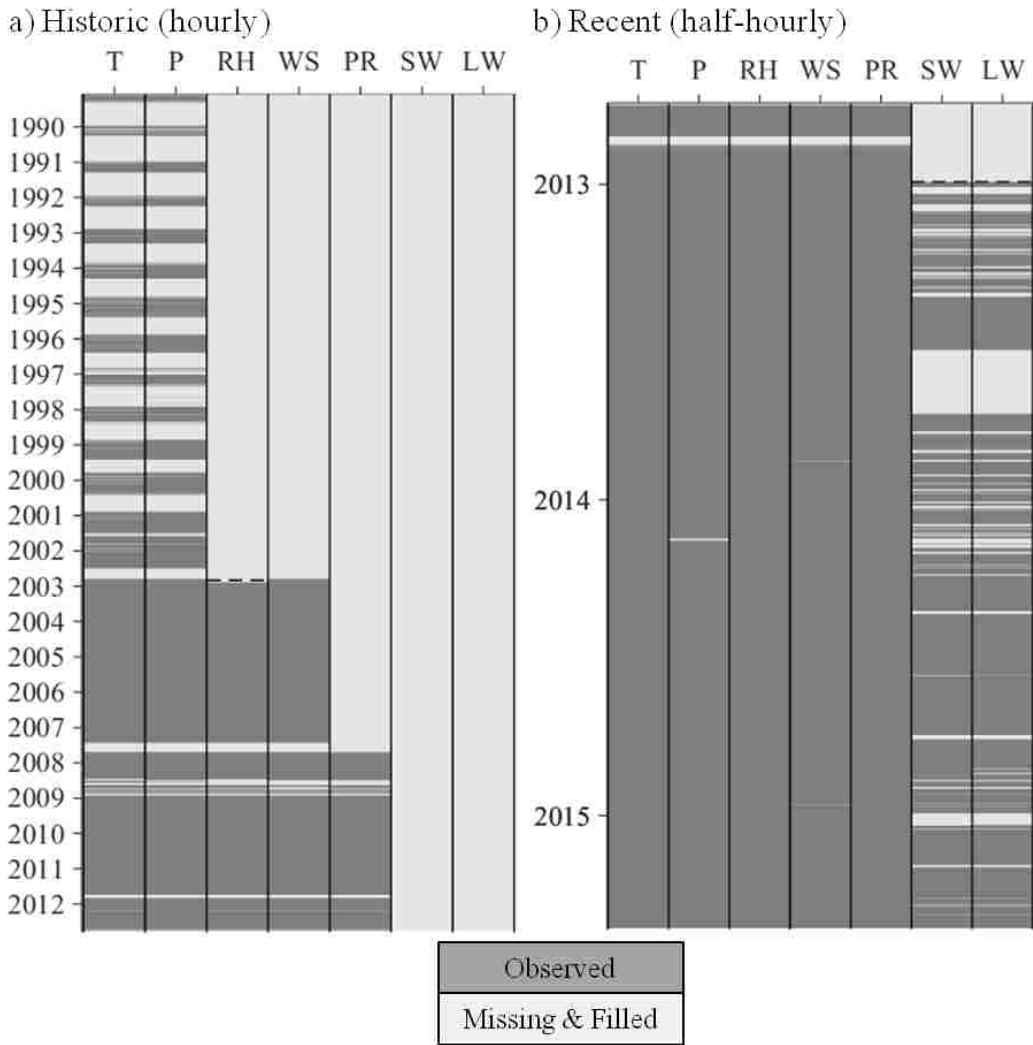


Figure 3-3. Availability of observed forcing data during (a) historic and (b) recent periods. *Dark gray lines* show observations that passed quality control or were filled with duplicate in-situ observations, while *light gray lines* indicate missing observations that were filled from alternative sources as described in Section 3.4. *Black dashed lines* show installation of instruments. Column variables are air temperature (T), total precipitation (P), relative humidity (RH), wind speed (WS), pressure (PR), shortwave irradiance (SW), and longwave irradiance (LW). Years on y-axis refer to January 1st.

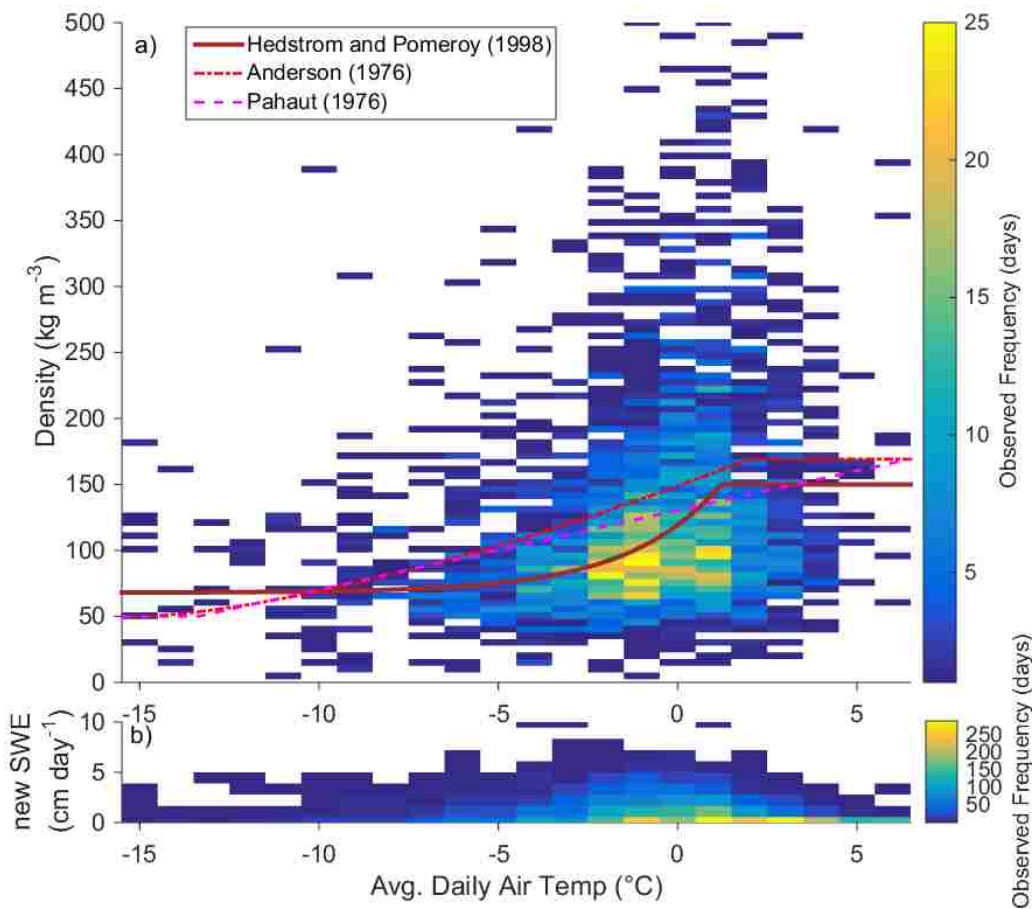


Figure 3-4. (a) New snow density from past 24 hour accumulation as measured by snow boards between 1974 and 2014 (N=2582 snow accumulation days) binned by daily average air temperature. Three common parameterizations of new snow density are shown for comparison. (b) Measured new SWE versus daily air temperature. Note: Some scatter in the observed new snow density may be due to compaction or melting occurring in between the time snow fell and the snow board measurement was made.

Chapter 4. Diagnosing Snow Accumulation Errors in a Rain-Snow Transitional Environment with Snow Board Observations

Note: This chapter is currently under review in the Journal of Hydrological Processes.

Abstract: Deficiencies in Earth System Models' representation of snow processes limits prediction of seasonal and altered climate sensitivity. Diagnosing the source of model errors requires intensive observations, a flexible model framework to test competing hypotheses, and a methodology to systematically test the involved snow processes. We present a novel process-based approach to diagnosing model errors through an example that focuses on snow accumulation processes (precipitation partitioning, new snow density, and compaction). Twelve years of meteorological and snow board measurements were used to identify the main source of model error on each snow accumulation day. Results found that with in-situ calibrated parameters, new snow density errors were the most common, occurring 53% of available days, followed by precipitation partition errors (43%) and compaction errors (18%). Precipitation partitioning errors mattered more for total winter accumulation during the anomalously warm winter of 2014-2015, when a higher fraction of precipitation fell within the temperature range where partition methods had the largest error. These results demonstrate how isolating individual model processes can identify the primary source(s) of model error, which helps prioritize future research.

4.1 Introduction

Physically-based models of the hydrological cycle are critical for testing our understanding of the natural world and enabling forecasting of extreme events. Previous intercomparison studies (i.e. SNOWMIP I & II, PILPS) of existing snow models that vary in complexity have been hampered by multiple differences in model structure [Essery *et al.*, 2009]. Recent efforts to encompass multiple model hypotheses into a single framework [Clark *et al.*, 2011a, 2015b; Essery *et al.*, 2013], have provided the tools necessary for a more rigorous validation of process representation in models. However, there exist few snow observatories that measure sufficient physical states and fluxes to fully constrain the possible combinations within these multiple model frameworks [Essery *et al.*, 2013; Landry *et al.*, 2014]. In practice, observations of bulk snow states, such as snow water equivalent (SWE) or snow depth, are most commonly available. Calibrating a snow model using a single bulk variable can lead to compensatory errors, which may hide model deficiencies that matter during extreme/unusual storms.

We present a novel process-based calibration method that takes advantage of multiple observations (including snow board measurements) at the Snoqualmie Pass (SNQ) snow study site, located in the maritime climate of the Washington Cascades, USA [Sturm *et al.*, 1995; Wayand *et al.*, 2015a]. As an example of this method, we focus on snow accumulation (or lack thereof) because of its importance for regional seasonal water storage and supply [Elsner *et al.*, 2010; Vano, 2015], its projected sensitivity to expected warming given the site's location in the rain-snow transition zone [Elsner *et al.*, 2010; Klos *et al.*, 2014], controlling runoff generation during flooding [White *et al.*, 2010; Wayand *et al.*, 2015b], and causing significant transportation delays through the Snoqualmie corridor [Barbara *et al.*, 2008]. Simulations of snow pack were performed using the Structure For Unifying Multiple Modeling Alternatives (SUMMA, Clark *et*

al., 2015a, 2015b, 2015c) model. Using historical snow board measurements of daily accumulated SWE and snow depth as proxies for daily precipitation partitioning and new snow density, respectively, we define a process-based calibration method to answer the following questions:

- 1) Which matters more, the functional form of a process (e.g., the choice of equation) or the parameters for that function?
- 2) What are the most common sources of errors in modeled snow depth accumulation at a maritime rain-snow transitional site?

4.2 Background

4.2.1. Sources of snow model uncertainty

Multiple sources of error affect Earth System Model predictions of observed states and fluxes. For snow models run uncoupled to an atmosphere, those sources include [Gupta *et al.*, 2012]: upper boundary conditions (meteorological forcing) [Raleigh *et al.*, 2014; Rössler *et al.*, 2014; Newman *et al.*, 2015], model structure (processes representation and parameter values) [Essery *et al.*, 2013; Clark *et al.*, 2015b], and numerical solver errors [Kavetski and Clark, 2011]. In order to isolate specific areas of model structure that are inadequate, which is the goal of this study, errors within the upper boundary condition must be minimized to prevent them from biasing model evaluations. Numerical errors are not addressed here, but left for future study.

4.2.2. Process observations

Unique observations are required to evaluate and improve existing snow model structure representation. While bulk snowpack states (e.g. SWE) are most relevant for streamflow predictions [Wood *et al.*, 2015], internal snowpack states (i.e. layered density, liquid water content, temperature) are critical to evaluate individual process representation [Clark *et al.*, 2011a; Wever *et al.*, 2015]. Recent advances in internal snowpack observations now provide information on individual snow processes. Likewise, historical data sets, such as snow board measurements, provide a widely observed but generally under-utilized source of information on individual processes. To improve seasonal snow simulations, we need to improve our *methods* of evaluating model structure to take advantage of multiple internal snow pack observations. In this study we present a novel methodology to evaluate individual processes that impact snow depth accumulation: partitioning of precipitation into ice or liquid, density of newly fallen snow, and the compaction of existing snow.

4.2.3. Isolated processes

Model process representations tested in this study are illustrated in Figure 4-1 and described below. For an in depth review of existing model parameterizations see *Essery et al.* (2013) and *Clark et al.* (2015c).

Precipitation phase at surface

The phase of a precipitation particle reaching the surface depends on the atmospheric conditions within the formation cloud as well the air mass it travels through during fallout to the ground [Lundquist *et al.*, 2008b]. The most reliable way of sampling the instantaneous particle type at the surface is still by human observation, followed by laser disdrometers, both of which are rare in mountainous terrain. On a daily time scale, partitioning type can be estimated from the ratio of

accumulated SWE on snow boards compared to total precipitation [Wayand *et al.*, 2015a]. Measuring precipitation in the form of snow is difficult and is the subject of intensive field campaigns [Yang and Goodison, 1998; Rasmussen *et al.*, 2012]. In contrast, observations of total precipitation (i.e. a tipping or weighing bucket) are more common and usually less biased if properly sited, heated, and shielded [Sevruk, 1983]. Thus, the partitioning phase determination is most often left to the hydrological or snow model [Harder and Pomeroy, 2013].

The most common method of predicting precipitation phase uses ground measurements of air temperature (T_a) (USACE, 1956; Auer 1974), dew point temperature (T_d) [Marks *et al.*, 2013], or wet bulb temperature (T_{wet}) [Harder and Pomeroy, 2013; Marks *et al.*, 2013], and sometimes upper-air observations [Sims and Liu, 2015], which are applied at sub-daily or daily time scales. See [Feiccabrino *et al.*, 2015] for an in depth review of existing methods. For this study, we use the wet-bulb temperature form based on the theory that it best represents the temperature of a falling hydrometer [Marks *et al.*, 2013]. T_{wet} was calculated iteratively using the psychrometric equation [Campbell and Norman, 1998] with saturated vapor pressure from [Buck, 1981], using in-situ observations of T_a , relative humidity, and surface pressure.

Density of newly fallen snow

Since the measurement of the density of *falling snow* is difficult, it is commonly measured as *newly fallen snow* on a surface over a period of 1 hour to 24 hours [USACE, 1956; Pfister and Schneebeli, 1999]. Most often the newly fallen snow is measured manually on a snow board, which is cleared periodically. The longer the period, the greater chance that other processes (i.e. wind redistribution, melting, settlement, etc.) may impact the measurement of newly fallen density, which complicates the evaluation of falling snow density parameterizations.

Methods used to predict falling snow density [Anderson, 1976; Hedstrom and Pomeroy, 1998; Boone, 2002; Oleson et al., 2010] have been fit to observational data measured as described above over a range of snow climates (maritime, continental, alpine). However, they all are based on surface air temperature [Anderson, 1976; Hedstrom and Pomeroy, 1998] and wind speed [Pahaut, 1976]. The predictability of these surface variables to characterize the variability of newly fallen snow density is known to be low [Roebber et al., 2003]. In operation, a common rule of thumb of $\sim 100 \text{ kg m}^{-3}$ is often simply used, which attempts to capture the mean density.

Compaction of accumulated snow

Compaction, or densification, of bulk snow is commonly measured by comparing the change in density measured from both bulk SWE and depth observations. The compaction of individual layers has also been measured using settling disks placed post-storm [USACE, 1956].

Compaction of the underlying snowpack (referred to here as “old” snow) during snow accumulation can be measured from the difference between newly accumulated snow depth (i.e. snow board) and the bulk snow depth change [USACE, 1956], assuming no loss of mass through melt. We used this latter method as illustrated in Figure 4-2a.

Parameterizations of model compaction vary from a simple constant rate to empirical functions that depend on snow viscosity, overburden pressure, metamorphism and liquid water. We use the commonly applied [Anderson, 1976] function, but only focus on parameters impacting compaction due to overburden (Table 4-2) as we show that this is the dominant process during snow accumulation events.

Summary

The above three processes are examined at the Snoqualmie Pass snow study site described in section 4.3. The snow model framework used here, and the process-based calibration method, are described in section 4.4. Selected model parameters and diagnosis of the sources of model errors are reported in section 4.5. The uncertainty and implications of error diagnosis and future uses of the methodology described here are then discussed in section 4.6, followed by a summary of the main conclusions in section 4.7. All abbreviations are defined in Table 4-1.

4.3. Study Site and Data

The Snoqualmie Snow study site is located within the upper rain-snow transition zone (921 m), receiving ~50% of October through June precipitation as snow. Despite mild temperatures, annual peak snow depths reach 2.6 m on average, accumulated by 12 storms per winter on average. The site is ideal for diagnosing modeled new snow accumulation errors because of its continuous record of snow board observations and meteorological forcing data. Site pictures, time-lapse movies, and a complete description of available data are provided by Wayand *et al.* (2015b, at <http://dx.doi.org/10.6069/H57P8W91>). Despite numerous snow observations, no bulk SWE measurements (e.g. a snow pillow) were available or used in this study. Below we detail all data used to drive and evaluate model simulations in this study.

4.3.1. Snow observations

Throughout winter months (typically November to May) since 1974, Washington Department of Transportation avalanche crew measured and then cleared, a 0.22 m² (45 cm x 48 cm) snow board (Figure 4-2a) daily at approximately 6:00 am PST. Accumulated snow depth was

measured from a graduated snow board stake. SWE was separately measured with a snow cutter (289.51 cm² area) and weighed with a scale. We refer to the 24-hr accumulations as *new* snow depth and *new* SWE. *Bulk* snow depth was manually read from a second 4 m snow stake each 6:00 am PST. Observational uncertainties were estimated as ± 25 mm for bulk snow stake readings of snow depth, ± 10 mm for new snow depth, and ± 1.3 mm for new SWE measurements (calculated from the new snow depth error of ± 10 mm and the average observed new snow density of 130 kg m⁻³). Additional uncertainty from horizontal transport of snow onto or off of the snow board was assumed negligible given the low mean wind speeds of 0.6 m s⁻¹ at the SNQ site, which were reduced by the surrounding forest (see Figure 3-2). Finally, we note that no automatic measurements of bulk SWE were available (e.g. a snow pillow), as is common at the majority of snow study sites worldwide.

The above daily snow observations were used as proxies for daily partitioning, new snow density and compaction of existing snow. The daily fraction of snowfall to total precipitation was calculated as the ratio of accumulated SWE on the snow board to the total precipitation measured by the heated and shielded tipping bucket. The density of the 24 hour accumulation of new snow was calculated directly as the ratio of measured SWE to measured snow depth on the snow board. Compaction of the existing snow pack (underlying the daily new snow accumulation) was estimated as the difference between the 24 hour change in bulk snow depth and the measured new snow depth accumulated on the snow board. This difference is illustrated in Figure 4-2a as the *green vertical bar*. All three daily proxies are used to evaluate process representation.

4.3.2. Meteorological forcing data

The meteorological data set used to drive snow model simulations was taken directly from Wayand *et al.* (2015b), except as follows. We restrict our study period to water years (Oct. – Sept.) 2004 through 2015, when all forcing variables critical for simulating snow accumulation (air temperature, relative humidity, wind speed, and precipitation) were measured in-situ (see Figure 3-3). Air pressure and incoming irradiance measurements were available only after 2008 and 2012, respectively. Missing forcing data were primarily filled from the National Land Data Assimilation Systems (NLDAS) data [Cosgrove, 2003], bias-corrected to available in-situ observations at SNQ as described in Wayand *et al.* (2015b). Precipitation gauge undercatch of snowfall was corrected using snow board SWE observations. Finally, half-hourly data for water years 2013 through 2015 were aggregated to hourly time steps to create a consistent meteorological forcing data set over water years 2004-2015.

4.4. Methods

We present a novel method for diagnosing sources of errors in modeled snow accumulation, which we refer to as the process-based method. This approach is contrasted with a more common method of calibrating a snow model using only observations of bulk snow depth. All simulations were performed using the Structure for Unifying Multiple Modeling Alternatives (SUMMA) model, with modifications as described below.

4.4.1. Snow model (SUMMA)

SUMMA is a physically-based hydrological model that simulates the energy balance and transport of water through the canopy, snowpack, soil and ground water [Clark *et al.*, 2015a,

2015b, 2015c]. For each physical process, the model includes multiple hypotheses of process representations that are currently used in existing snow and land surface models. Required meteorological forcing data include: air temperature, precipitation rate, wind speed, specific humidity, air pressure, and incoming short- and long-wave irradiance. Complete model configurations are provided in Table S1 of *Wayand et al.* (in press).

4.4.2. Simulating snow board measurements with SUMMA

SUMMA simulations were modified in order to allow a direct comparison to the snow board observations of 24 hour accumulated SWE and snow depth (Figure 4-2a). This was a critical step for a fair model evaluation. Because the snow board measurements were made daily at 6:00 am PST, and then the board was cleared of all snow, SUMMA simulations were restarted every 6:00 am PST with the previous accumulated snowpack removed (Figure 4-2b). Each daily restart simulation used initial soil conditions from a continuous SUMMA simulation with default parameter settings with two significant modifications: 1) the soil albedo was set at 0.8 to match the albedo of a snow board, and 2) the upper soil layer temperatures were set to the upper snow layer temperatures (if present in the continuous simulation) to match the surface temperature of the actual snowboard prior to snow fall. A sensitivity analysis found that the choice of plausible snow board albedo (0.6-0.9) or reasonable initial temperature values did not impact simulated daily SWE or snow depth accumulation significantly.

4.4.3. Lumped calibration method

A lumped calibration method (Figure 4-3a) was used to set an upper bound of SUMMA performance based on previous work that has showed that allowing free-ranging parameters will always identify the optimal fit to any designated criteria [*Gong et al.*, 2011; *Nearing and Gupta*,

2014]. A 5342 member ensemble of continuous SUMMA simulations were performed by varying function and parameter combinations for partitioning, new snow density, and compaction simultaneously, as described in section 4.2. Parameter values were selected through uniform random sampling through feasible parameter space as defined in Table 4-2.

We only used the bulk daily accumulation of snow depth for calibration to be representative of a typical observational snow site (i.e. without manual snow board or bulk SWE measurements). Simulated daily accumulation of bulk snow depth for each ensemble member was evaluated during the 2004 to 2009 water years using the modified Kling-Gupta efficiency (KGE) [Gupta *et al.*, 2009; Kling *et al.*, 2012],

$$KGE = 1 - \sqrt{(r - 1)^2 + (\alpha - 1)^2 + (\beta - 1)^2} \quad \text{Equation 1}$$

Where r is the correlation coefficient, α is the ratio of modeled to observed coefficient of variation, and β is the ratio of model mean to observed mean. This metric was chosen because it can be separated into a correlation term, a variance term, and a bias term [Magnusson and Wever, 2015]. We note that the variance term did not significantly impact results here, but keep the formula to remain consistent with previous snow model evaluation studies. A perfect simulation has a KGE value of one.

4.4.4. Process-based calibration

A process-based method to calibrate snow model options/parameters (referred to as “model configuration” from here on) relating to snow accumulation was designed to minimize the propagation of forcing and model errors that impact calibration (Figure 4-3b). We evaluated one

process at a time and attempted to remove cascading errors into the next process evaluation (*e.g.* Information pathways in Figure 4-1).

First, we minimized meteorological forcing errors by selecting the 2004 to 2015 water years where the majority (98%) of forcing data that impact new snow accumulation (air temperature, precipitation, wind speed, and relative humidity) were taken from in-situ observations. Next, an ensemble of simulations (Table 4-2) was run for modeled processes impacting snow accumulation examined in this study (partitioning, new snow density, and compaction). Process parameterizations were selected from a range of the most commonly used functions in snow hydrology models [Essery *et al.*, 2013; Clark *et al.*, 2015b]. Parameter ranges for each function were determined by choosing values that resulted in physically possible estimated states or fluxes, as illustrated in Figures S1-S6. Each ensemble of simulations, referred to as process experiments, was run in a step-wise approach as illustrated in Figure 4-3b and described below.

For the partitioning experiment, we evaluated all days when both precipitation occurred and observations of daily accumulated SWE were available (N=564). Figure 4-4a shows all model simulations compared to snow board observed SWE for an example period where the sensitivity of the linear partitioning method varied depending on the wet-bulb temperature (T_{wet}). The ensemble member with the highest KGE value was selected, and its parameter values were applied to the snow density experiment, as illustrated in Figure 4-3b.

For the snow density experiment, only days when the simulated SWE error was less than observational uncertainty (± 1.3 mm) were evaluated to prevent large partitioning errors from propagating into new snow density evaluations. Again, the ensemble member with the highest

KGE value was selected, and its option/parameter values were applied to the compaction. Figure 4-4b illustrates modeled new snow depth sensitivity to density model configuration. This direct comparison is only possible because we modified SUMMA to match observations. For instance, if we had instead only used the difference in the bulk snow depth between days, compaction of the underlying snowpack would have biased our measure of new snow density. Remaining factors impacting snow density changes between the time of snowfall and the time of the snow board measurement are discussed in section 4.6.

For the compaction experiment, we assumed that overburden was the dominant factor contributing to compaction of the existing snowpack during snow accumulation days (discussed in Section 4.6.2). Therefore, it follows that compaction errors will be largest for days when the accumulation of SWE for that day was biased. Thus we only evaluate model compaction values during days when the simulated partitioning (modeled new SWE) values were within observational uncertainty. Modeled compaction of the existing snowpack was calculated from model states exactly as observed compaction was calculated, as described in section 4.3.1. To be explicit, modeled compaction was defined as the difference between the daily modeled change in bulk snow depth (continuous simulation) to the modeled accumulation of new snow depth (snow board simulation) as defined in Equation 2,

$$Comp_{mod} = newDepth_{mod} - bulkDepth_{mod} \quad \text{Equation 2}$$

Finally, the two parameters that control compaction due to over burden ($D1$, $D2$) as implemented in the Anderson (1976) function were varied in an ensemble of 81 simulations.

4.4.5. Diagnosing daily snow accumulation errors

From the process-based methods above, we kept track of the most likely source of model error during each day using the best fit parameters provided in Table 4-2. Given the direction of error propagation from partitioning, to new snow density, into compaction (Figure 4-1), we were only able to isolate the error source for the subset of days where all “upstream” errors were within observational uncertainty (see Figure 4-1). For example, of the 564 snow accumulation days between 2004 and 2009, the simulated daily partition was within the observational uncertainty on 333 days, thus the modeled newly fallen snow density skill could only be assessed for these 333 days, with the remaining 231 assumed to be in error due to partitioning. Uncertainties in this error diagnostic approach are discussed in section 4.6.2.

4.4.6. Case study of water year 2015

As an example of the application of the process-based error diagnostic method, we focused on water year 2015 because its winter average temperature anomaly (+2.1 °C) was equal to projected winter temperature increases in the 2040’s [Elsner *et al.*, 2010; Klos *et al.*, 2014; Mauger *et al.*, 2015; Vano, 2015]. During historically low snow years (e.g. California 2006-2015 drought, (Kogan and Guo, 2015)), the water content of snow has become more valuable per unit volume, thus errors in model predictions of snow accumulation will have a larger impact on water resources. Characterizing errors in modeled new snow accumulation will help focus efforts to improve model robustness in the current and future rain-snow transitional climates.

4.5. Results

4.5.1. Lumped method results

From the ensemble of 5342 model configurations, the “best” simulation of bulk snow depth accumulation was selected for water years 2004 to 2009 using the highest KGE metric (Equation 1). Selected parameter values are provided in Table 4-2. Because SUMMA was purposefully calibrated to the accumulation of bulk snow depth, the best model run had a small bias of 1% of observations and a KGE value of 0.78. The model skill from the calibration represented an upper bound for this site and water years given the ability of new snow accumulation functions included here [Gong *et al.*, 2011; Nearing and Gupta, 2014]. Hidden model errors in bulk snow accumulation that had a compensatory impact throughout the study period were diagnosed using the process-based approach as reported below.

4.5.2. Process-based method results

Precipitation partitioning experiment

Simulated daily SWE accumulation (new SWE) was sensitive to the range of parameters because the SNQ winter wet-bulb temperature (T_{wet}) was frequently near 0 °C during snowfall events. Modeled new SWE sensitivity is illustrated in Figure 4-5a, where all model configurations (*grey circles*) are compared to observations of new SWE for the calibration period. The parameter options with the lowest model error (*blue dots* in Figure 4-5a) had a T_{wet} critical value (P_c) of -0.24 °C with a mixed-phase range (P_r) of 1.625 °C (Table 4-2). Out of the 564 days with observed or modeled snowfall during the calibration period (water years 2004-2009), the model was within the uncertainty of the snow board SWE measurements (± 1.3 mm) 333 days (59%), which was 64% of total accumulated SWE (Table 4-3). The remaining 231 (41%) days

highlighted the difficulty of predicting precipitation phase at this maritime site using near-surface T_{wet} .

The observed fraction of daily precipitation measured as ice is shown in Figure 4-6a. The daily fraction as ice was calculated from the ratio of daily accumulated SWE on the snowboard to the daily accumulated precipitation (rain and snow). Total precipitation amount is indicated by the relative circle size. The partitioning function with the above selected parameters is also shown in Figure 4-6a, which does not appear to match the daily observations. However, this discrepancy is partly explained by the difference in time steps between the observations (daily) and model (hourly). The daily fraction of ice derived from the modeled snow board SWE using the above partitioning function is shown in Figure 4-6b, which more closely matches the observations on an equal daily resolution. Using this more direct comparison, we found the largest model errors in accumulated SWE occurred near a T_{wet} of 0°C (Figure 4-6c) but were unbiased as a result of calibration (Figure 4-5a).

New snow density experiment

The above identified errors in partitioning directly impacted simulations of bulk snow depth and the calibration of best new snow density function. Evaluation of the ensemble of new snow depth simulations using all days ($N=564$) and only days where partitioning errors were within observed uncertainty ($N=333$), are shown in Figure 4-5b and 5c, respectively. The exclusion of partitioning errors reduced the largest new snow depth errors (reduced scatter of grey dots in Figure 4-5c). The ensemble member with the lowest error (highest KGE value) in daily accumulated snow depth was different for the two sets of days. Excluding partitioning error days

resulted in the constant density method with a value of 78 kg m^{-3} , while including all days selected the Pahaut (1976) method (Table 4-2).

In general, the choice of parameter values was more important than the choice of new snow density function, as illustrated by Figure 4-7a. All new snow density functions could have a KGE value greater than 0.8 (*red dots*) so long as the correct parameter values were selected for this location. However, if the optimal parameter values were unknown and selected at random, the Hedstrom and Pomeroy (1998) and Pahaut (1976) functions would have a higher likelihood of a higher KGE value. The resulting functions compared to observations are shown in Figure 4-7b, which further illustrates the similarity in moderate skill between all competing hypotheses. The large variability of measured density for a given average temperature was a combination of variations in falling density, compaction, and melting; which are further discussed in section 4.6.2.

Compaction experiment

The modeled compaction of the existing snowpack exhibited large sensitivity to the range of parameter values used here (Figure 4-5d and 5f). Excluding days where the partitioning error was outside observational uncertainty (Figure 4-5f) removed many of the largest errors in modeled snow compaction. For the remaining subset of days where partitioning was correct (333 days), modeled compaction was in error 67 days (Table 4-3).

4.5.3. Bulk snow depth

Simulations of bulk snow depth using the three model configurations in Table 4-2 are compared to observations for the calibration period (Figure 4-8a) and evaluation period (Figure 4-9a). All

simulations produced generally high quality simulations of the total bulk snow depth for most water years, despite having different model configurations (Table 4-2). A notable result was that both process-based configurations had similar skill in simulating the bulk snow depth as the lumped configuration, which represented the upper bound in this study. However, inter-model simulation differences were found in simulated new SWE (Figure 4-8b and Figure 4-9b), new snow depth (Figure 4-8c and Figure 4-9c), and old snow compaction (Figure 4-8c and Figure 4-9c); which had a compensatory effect on bulk snow depth accumulation.

4.5.4. Diagnosis of bulk snow accumulation errors

For both the calibration and evaluation periods, errors due to partitioning of precipitation resulted in the largest absolute number of days compared to other processes (Figure 4-10). However, process of new snow density and compaction were only evaluated for days where partitioning errors were small (to prevent cascading errors). Therefore, as a percentage of all available days each process was evaluated (*outlined boxes* Figure 4-10), new snow density errors were most common (55% calibration, 52% evaluation), followed by partitioning errors (41% calibration, 45% evaluation), and compaction of old snow errors during accumulation days (20% calibration, 16% evaluation) (Table 4-3). Only 25% of days were identified as having none of the above errors, which meant that during the majority of snow accumulation days (75%) at least one process representation failed; most commonly new snow density and precipitation partitioning. However, the individual daily errors identified canceled out over annual time scales during most years, resulting in high skill in simulating bulk snow depth (Figure 4-8 and Figure 4-9). The exception to this finding was water year 2015, which had an anomalously warm winter (December through February) temperatures 2°C higher than the 1980 to 2014 average.

Figure 4-11 illustrates the identified source of bulk snow depth accumulation errors during water year 2015 for each day. While on average, about 12 storms build the annual snowpack during our study period, observations show that the 2015 seasonal snowpack was built with only seven storms. The dominant source of new snow accumulation error during the seven major storms of water year 2015 was incorrect partitioning, based on the process-based evaluation. Four available manual full snowpit measurements of bulk SWE [Wayand *et al.*, 2015a] corroborate that the model accumulated too much mass, in contrast to a density error (not shown). Interestingly, water year 2015 had precipitation partitioning errors as often as other years (Figure 4-10), but those errors mattered more toward bulk snow accumulation because a larger fraction of winter precipitation occurred near the freezing point, where partitioning parameterizations were most uncertain (Figure 4-6c). This example illustrates the utility of the process-based method, which is not to select the best-fit model, but that when the best-fit model fails, to identify the process(es) responsible for that failure (e.g. precipitation partitioning in water year 2015). In addition, the process-based method identified the need for new partitioning methods that will not fail during warm winters, which may become more common in the future for the Washington Cascades (Elsner *et al.*, 2010; Klos *et al.*, 2014; Vano, 2015; Mauger *et al.* 2015).

4.6. Discussion

4.6.1. Robustness of simulations of bulk snow accumulation

The lumped method identified a model configuration that resulted in very low error simulating bulk snow depth during both calibration and evaluation periods (Figure 4-8 and Figure 4-9).

However, the process-based approach presented here revealed that on a daily time scale, one of

the three snow accumulation processes was in error 80% of the time, indicating the models did not get the right answer (i.e. bulk snow depth accumulation) for the right reasons [Kirchner, 2006]. This level of skill may be acceptable for some applications (i.e. predicting peak basin-averaged SWE for seasonal streamflow forecasts) but will not be acceptable for others (i.e. assessing climate change sensitivity, forecasting of rain-on-snow floods, or backing out SWE from observed snow depth (Egli *et al.*, 2009; Sturm *et al.*, 2010; Currier *et al.* 2016).

4.6.2. Uncertainty in diagnosis of daily model error source

Processes of precipitation phase, density of falling snow, and compaction of existing snowpack were measured indirectly with available daily observations at the SNQ site (i.e. snow board measurements). An assessment of the degree to which the daily time scale impacted the diagnostic of sources of error was done to ascertain the uncertainty of this study's results.

The measured snow board SWE every 24 hours is a function of the accumulated snowfall and retained rainfall minus any drained snowmelt. Retention of rainfall in newly accumulated snow (i.e. during the passage of warm fronts when snow changes to rain) should be less than ~10% by mass [Boone and Etchevers, 2001; Essery *et al.*, 2013], which suggests that our daily partitioning fractions calculated in this study (Figure 4-6) could be biased high by 10% during these events. Quantifying the additional error introduced by partial melting of accumulated snow board SWE is more difficult. Although snowmelt lysimeter observations were available, they are 1) impacted by hydrological process taking place throughout the bulk snow pack, and 2) did not always provide accurate quantitative estimates of snowmelt [Wayand *et al.*, 2015a].

Additional processes that impacted the measured snow density after 24 hours besides the density of *falling* snow include the compaction of accumulated snow due to overburden,

metamorphism, and/or wind redistribution. Thus, some of the scatter in Figure 4-7 is likely due to a combination of these processes and variability in the density of falling snow [Wayand *et al.*, 2015a]. Without direct observations of falling snow density, or sub-daily observations of fallen snow density, it is difficult to separate out these impacts and quantify their effect on the calculated density values shown in Figure 4-7.

Compaction of the underlying snowpack was calculated here based on measurements of the change in total bulk snow depth (from a snow stake) and accumulation of new snow depth (from a snow board). Besides the observational uncertainty of both measurements, additional error may have resulted from differential accumulations of snow at each location (~12 m apart); however, this difference is likely small compared to the average daily new snow depth accumulations (51 mm day^{-1}) and average compaction rates (25 mm day^{-1}) observed.

The assumed control of overburden on compaction rates was supported by the fact that observed bulk compaction showed a high correlation ($R^2=0.6$) with the amount of accumulated new SWE. Further, temperature driven metamorphism and resulting compaction was likely small given small internal snowpack temperature gradients in a maritime climate during snow accumulation. However, the impact of liquid water was likely significant, especially during frequent warm frontal systems when snow switched to rain within a few hours. We were unable to isolate this process given available observations.

In summary, the proxies used to represent precipitation partitioning, new snow density, and compaction process were impacted by other processes that could not be isolated given available observations at the SNQ site. Thus these proxies could not be compared directly to each process parameterization, but were instead used to evaluate the modified SUMMA snow

board simulations (Figure 4-2b), which inherently included non-isolated process. For example, snow board simulations of new snow density were impacted by compaction and potential snowmelt, thereby matching available snow board observations that are also impacted by these processes.

4.6.3. Applicability of process-based method

The methodology used here to identify process representation errors and limit propagation of model errors can be generalized to other areas of snow hydrology. The requirements for such application are observations of the boundary conditions (here meteorological forcing data) and internal snow pack observations (here daily new snow accumulation). A lack of the required observations is likely the greatest limitation to applying this method to other processes and at other locations, which makes efforts to connect and share available mountainous data sets (Pomeroy *et al.* 2015) critical for model development.

4.7. Summary

This study presented a novel process-based approach to diagnosing model errors through an example that focused on snow accumulation processes. Although the underlying principle to isolate model process and reduce propagation of model errors has been previously advocated [Clark *et al.*, 2011a], this is the first study to the authors' knowledge that has provided a complete implementation. For the Snoqualmie Pass study site, we found that errors in new snow density and precipitating partition occurred during 53% and 43% of available snow accumulation days, respectively, while compaction errors were less frequent (18%). We found that the choice of new snow density function and parameter values was impacted by “upstream” precipitation partitioning errors, suggesting caution must be used to evaluate future new snow density

parameterizations. Finally, the main benefit of the process-based method is not that it results in a better fit than traditional calibration methods (Figure 4-8 and Figure 4-9), but that when the model fails we can identify the process responsible for that failure (i.e. partitioning in water year 2015, Figure 4-11). Therefore, these results suggest that effort should be focused on improving precipitation partition parameterizations for rain-snow transitional climates, especially during anomalously warm winters; thereby illustrating why process isolation and analysis is critical for model development and advancement.

Acknowledgements

All meteorological raw, quality controlled and filled data are available at <http://dx.doi.org/10.6069/H57P8W91>. SUMMA model code is available at <https://github.com/NCAR/summa> and scripts to create SUMMA configuration files used in this study are available at https://github.com/NicWayand/summa_scripts. This work was supported by the National Science Foundation (EAR-1215771).

4.8. Tables

Table 4-1. Definitions of abbreviations used.

KGE	Kling Gupta Efficiency
SWE	Snow water equivalent
New Snow	The new snow accumulated on a snow board within 24 hours
Old Snow	The existing snowpack underlying the accumulated “New” snow
Bulk Snow	The total snow depth from the ground to the snow surface (New and Old)
P	Precipitation
RH	Relative Humidity
T _{wet}	Wet-bulb temperature
T _{air}	Near surface air temperature
WS	Near surface wind speed

P_{frozen}	Fraction of precipitation ice
P_{liquid}	Fraction of precipitation liquid

Table 4-2. Model options and parameter values.

Process	Option	Parameter full name (abbreviation) [unit]	Min Value	Max Value	Default value from literature	Lumped method selected value	Process-based method <i>without</i> Cascading errors selected value	Process-based method <i>with</i> Cascading errors selected value
Precipitation Partitioning	[USACE, 1956]	Center threshold (Pc)[°C]	-1	1	1	0	-0.24	-0.24
		Mixed-phase range (Pr) [°C]	0.1	5	4	0.5	1.625	1.625
New snow density	[Hedstrom and Pomeroy, 1998]	Minimum new density (SDmin)[kg m ⁻³]	50	100	67.92	100	-	-
		Density multiplier (SDm)[kg m ⁻³]	25	75	51.25	50	-	-
		Density scalar (SDsc)[°K]	1	5	2.59	1	-	-
	[Pahaut, 1976]	Density additive (SDa) [kg m ⁻³]	80	120	109	-	-	80
		Density multiplier (SDb)[kg m ⁻³ K ⁻¹]	1	12	6	-	-	1
		Wind speed factor (SDc)[kg m ^{-7/2} s ^{-1/2}]	16	36	26	-	-	21
	[Anderson	Minimum new	50	100	50	-	-	-

	, 1976]	density (SDmin)[kg m ⁻³]						
		Density Multiplier (SDd) [°K ⁻¹]	1	3	1	-	-	-
	Constant new snow density	Constant density (SDconst)[kg m ⁻³]	50	250	100	-	76.8	-
Compaction	[Anderson, 1976]	Overburden density scalar (D1)[kg ⁻¹ m ³]	0.02	.036	0.0230	0.02	0.02	0.02
		Overburden temperature scalar (D2) [°K ⁻¹]	0.06	0.1	0.0800	0.06	0.095	0.1

Table 4-3. Number of days attributed to each source of modeled¹ error.

	Variable evaluated (process represented)	# days snow fall	# days unknown due to upstream error or missing observations required ²	# available days to evaluate process	# days model error <i>within</i> observed uncertainties (# days available) [% of available days]	# days model error <i>outside</i> observed uncertainties (# days available) [% of available days]
Calibration Period (2004-2009)	New SWE (precipitation partitioning)	564	0	564	333 (564) [59%]	231 (564) [41%]
	New Depth (snow density)	564	231	333	151 (333) [45%]	182 (333) [55%]
	Old Compaction (overburden compaction)	564	231	333	266 (333) [80%]	67 (333) [20%]
	No Error				144 (25%)	
Evaluation Period (2010 - 2015)	New SWE (precipitation partitioning)	552	0	552	304 (552) [55%]	248 (552) [45%]
	New Depth (snow density)	552	248	304	147 (304) [48%]	157 (304) [52%]
	Old Compaction (overburden compaction)	552	248	304	256 (304) [84%]	48 (304) [16%]
	No Error				138 (25%)	

¹ Statistics shown for the process-based SUMMA configuration without cascading errors.

² For example, modeled snow density values were not evaluated for days where a precipitation partitioning error was observed.

4.9. Figures

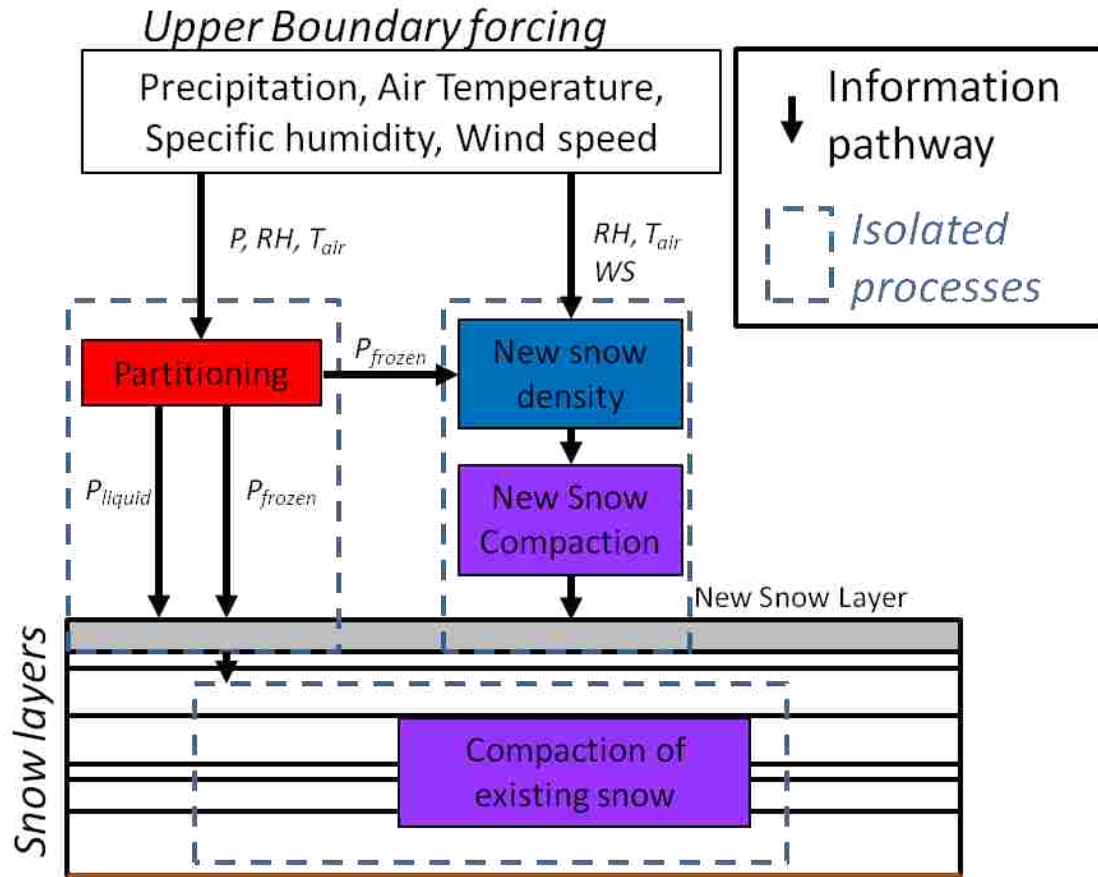


Figure 4-1. Example of isolating new snow accumulation processes. All fluxes into *dashed boxes* were taken directly from observations when possible. Variable abbreviations are defined in Table 1.

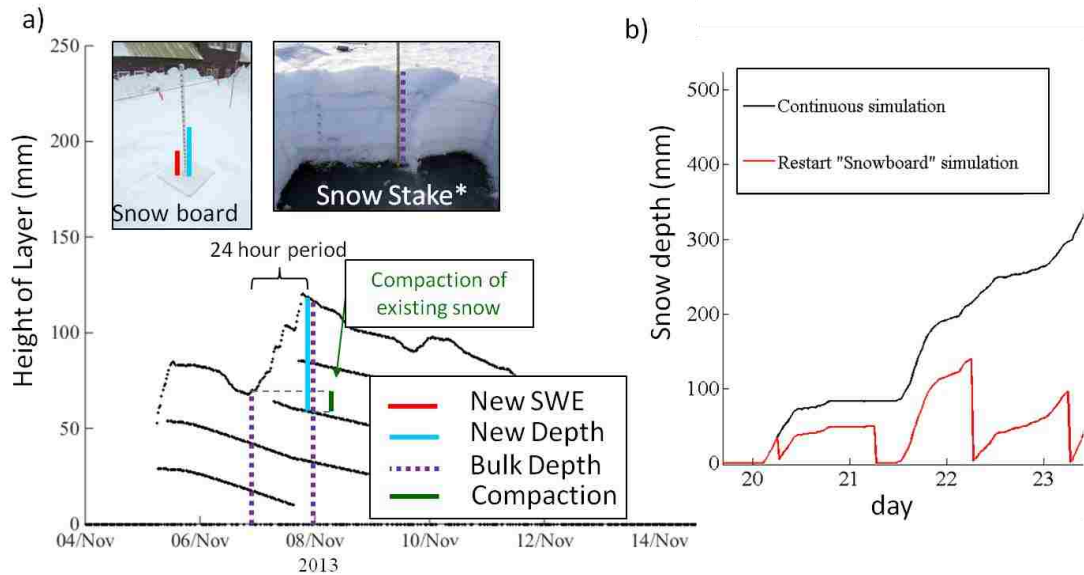


Figure 4-2. (a) Images show available measurements of new SWE, new snow depth, and bulk snow depth. *Horizontal black lines* show modeled snow layers (accumulation, compaction and merging) that are representative of observed layers shown in right image. *Note: the right image shows a snow pit for illustration only, bulk snow depth was read from off a 4 m snow stake (see Figure 2 of Wayand *et al.* 2015). (b) Example of the “modeled snowboard” simulations, which were compared to observations in (a). Note: the *red line* shows modeled snow depth at the *end* of modeled hourly time step, thus first step is non-zero.

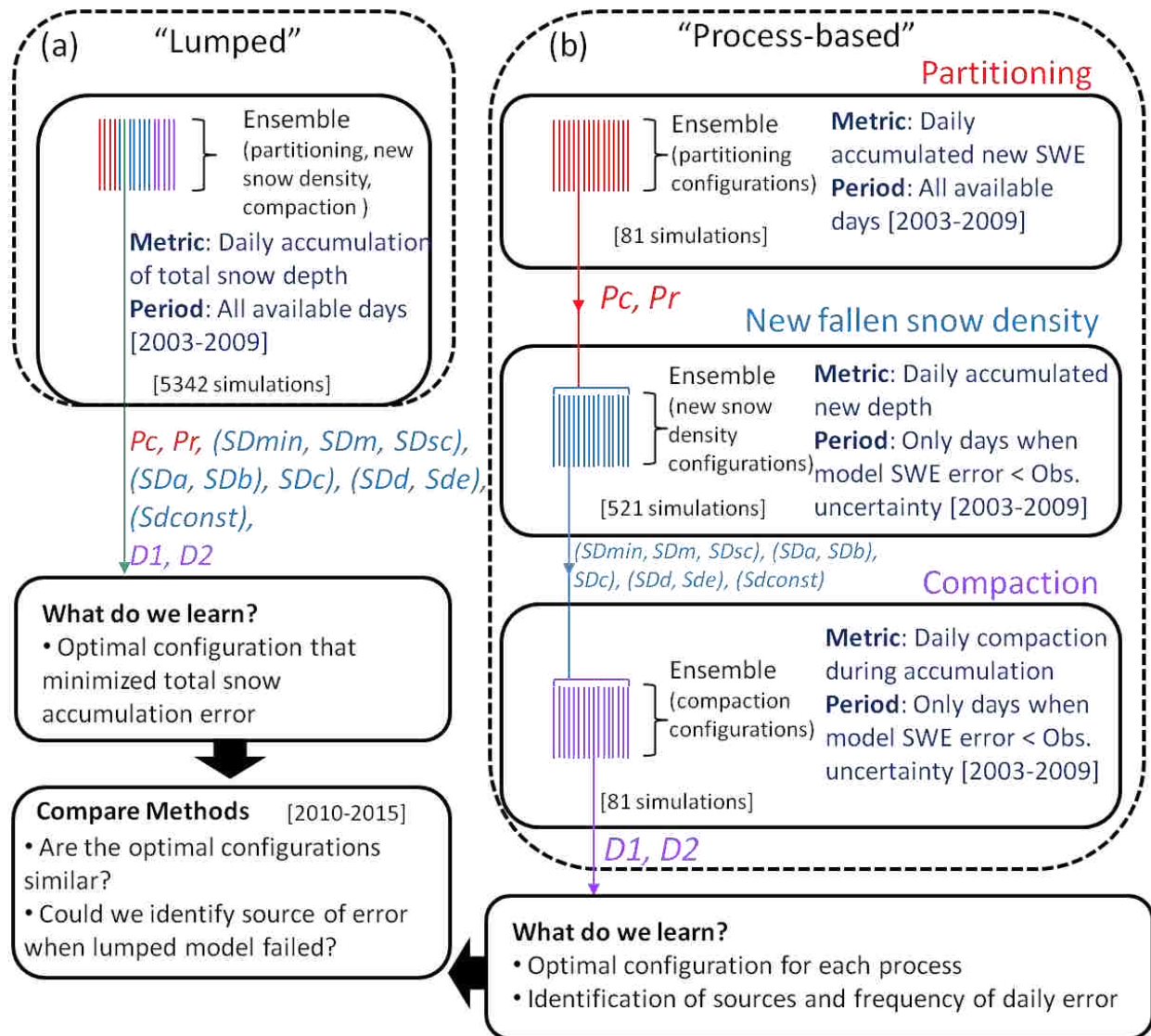


Figure 4-3. Methodology for both (a) Typical and (b) Processed based methods. The typical method uses a lumped calibration approach by running all model option/parameter configurations. In contrast, the processed based method evaluates one process at a time, passing on the selected option/parameters to the next process evaluation. Selected model option/parameters are defined in Table 3.

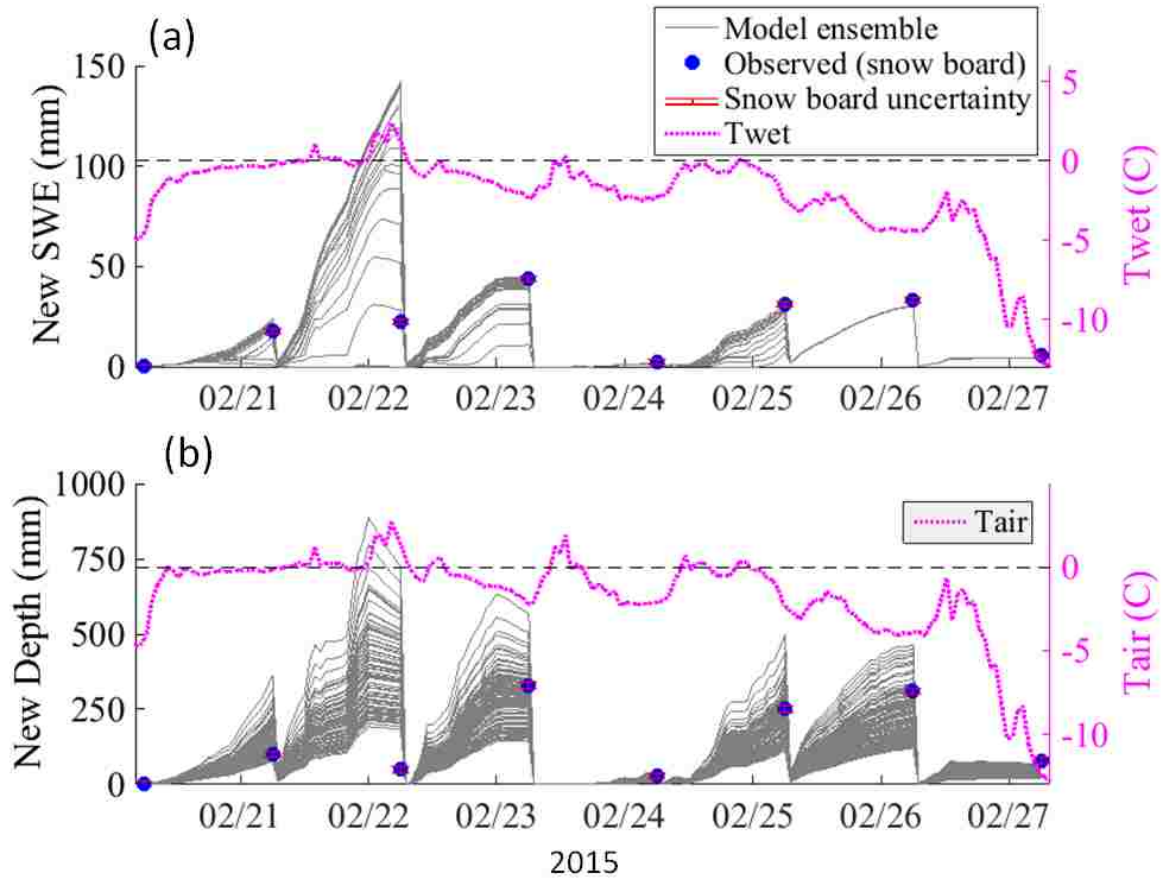


Figure 4-4. Example of model ensemble of (a) accumulated SWE, and (b) accumulated snow depth, compared to independent snow board measurements of 24 hour accumulated SWE and snow depth. Observed wet-bulb (T_{wet}) and air (T_{air}) temperatures are also shown because modeled partition depended on T_{wet} and new snow density on T_{air} .

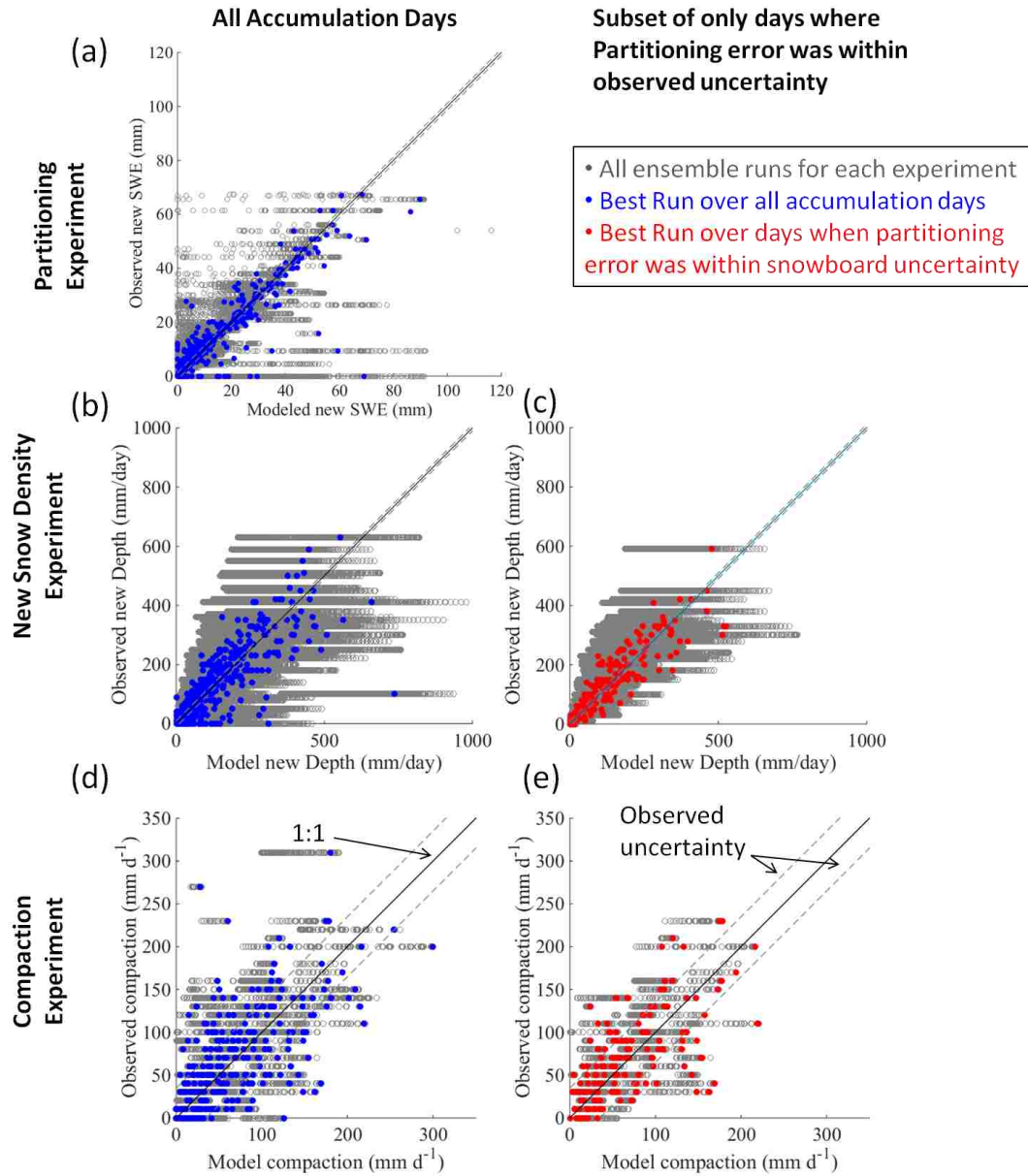


Figure 4-5. Modeled and observed daily accumulated new SWE (a), new snow depth (b), and compaction (c), shown for each day. *Gray circles* show all ensemble simulations. *Blue and red filled circles* show ensemble member selected from the highest KGE value.

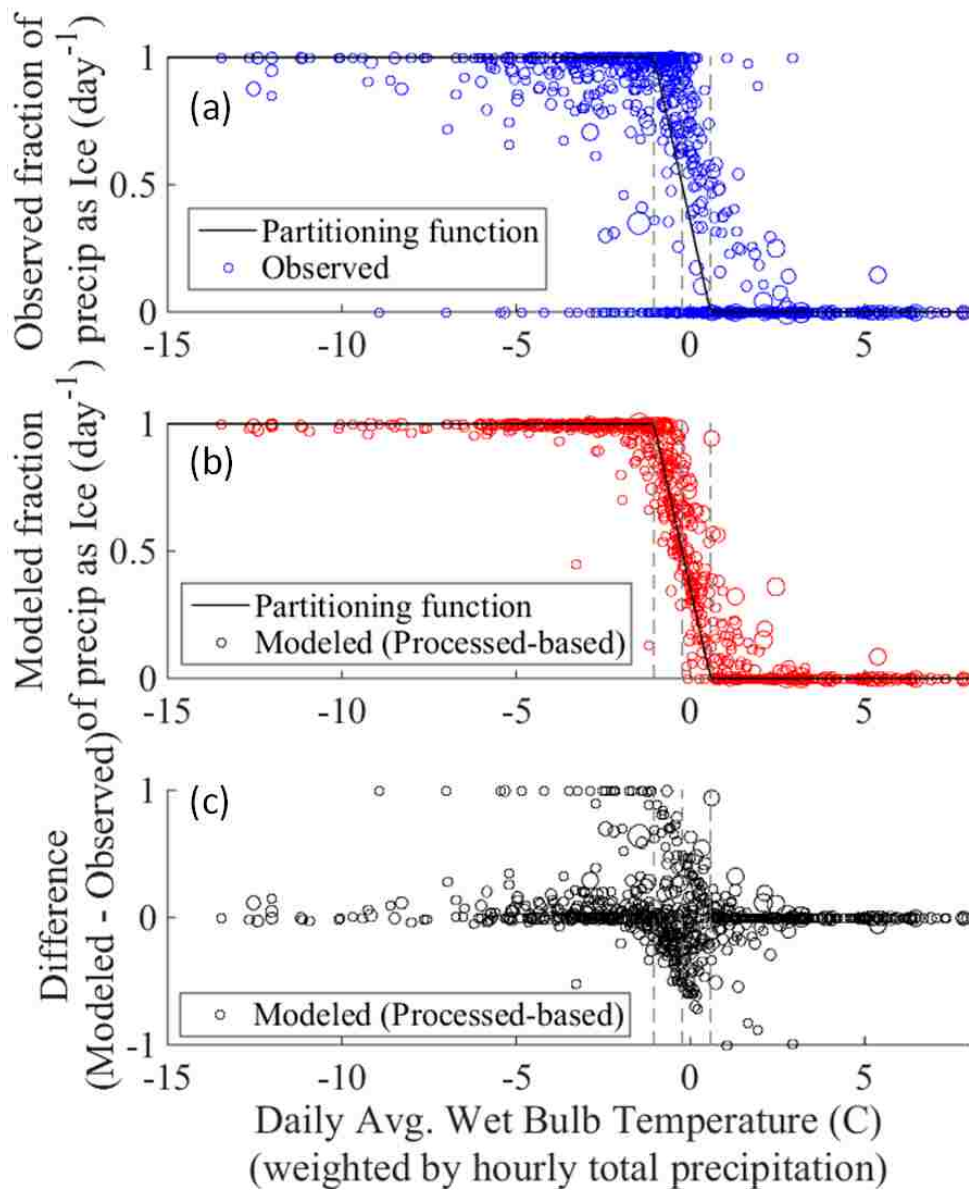


Figure 4-6. Daily fraction of precipitation (a) observed and (b) modeled as ice. Observed fraction was calculated from the ratio of snow board SWE to total gauge precipitation. Modeled fraction was calculated from the ratio of simulated new SWE (restart simulations) to the observed total gauge precipitation.

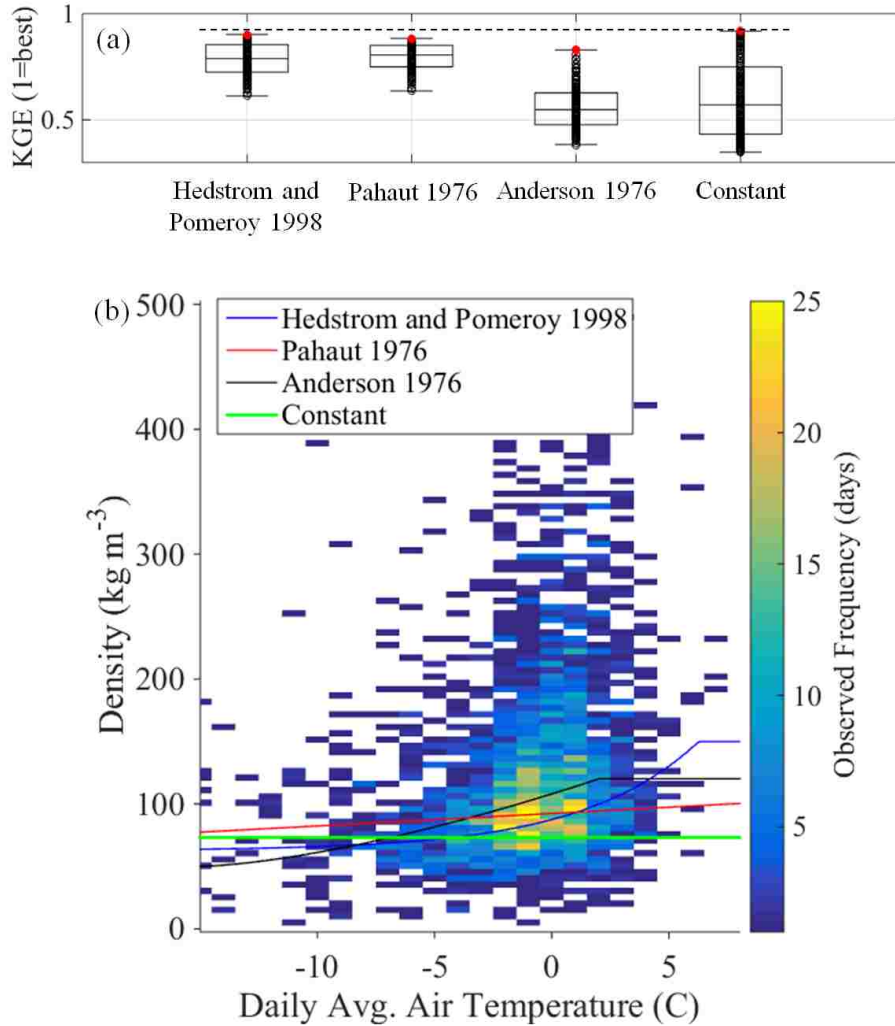


Figure 4-7. (a) Calibration results for each new snow density function, showing near-equal performance given the right parameter values. A KGE value of unity is best. (b) Observed newly fallen snow density compared to the daily average air temperature during water years 1980-2015. Overlaid lines, show each function in (a) with the highest KGE value (*red circles*).

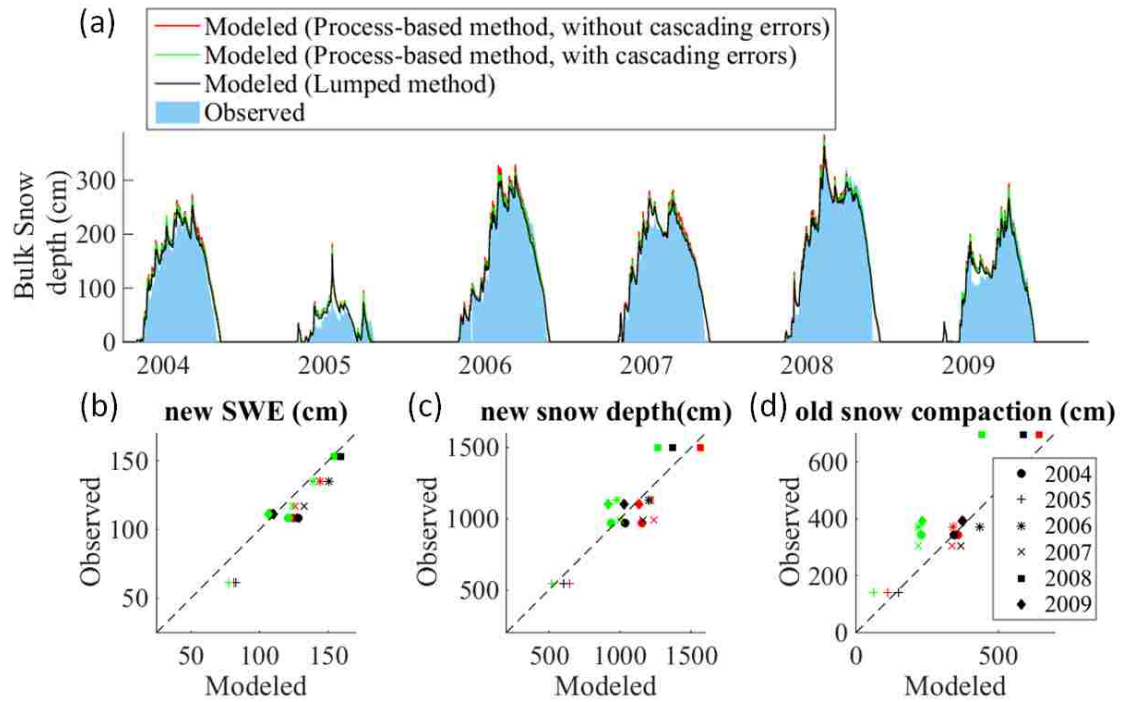


Figure 4-8. (a) Modeled and observed bulk snow depth during the calibration period (water years 2004-2009). Vertical white periods represent missing snow stake measurements. Scatter plots of modeled and observed *total accumulated* new SWE (b), new snow (c), and compaction of old snow during accumulation days (d) for each water year. Symbol type indicates each water year while color refers to model simulations defined in legend (a).

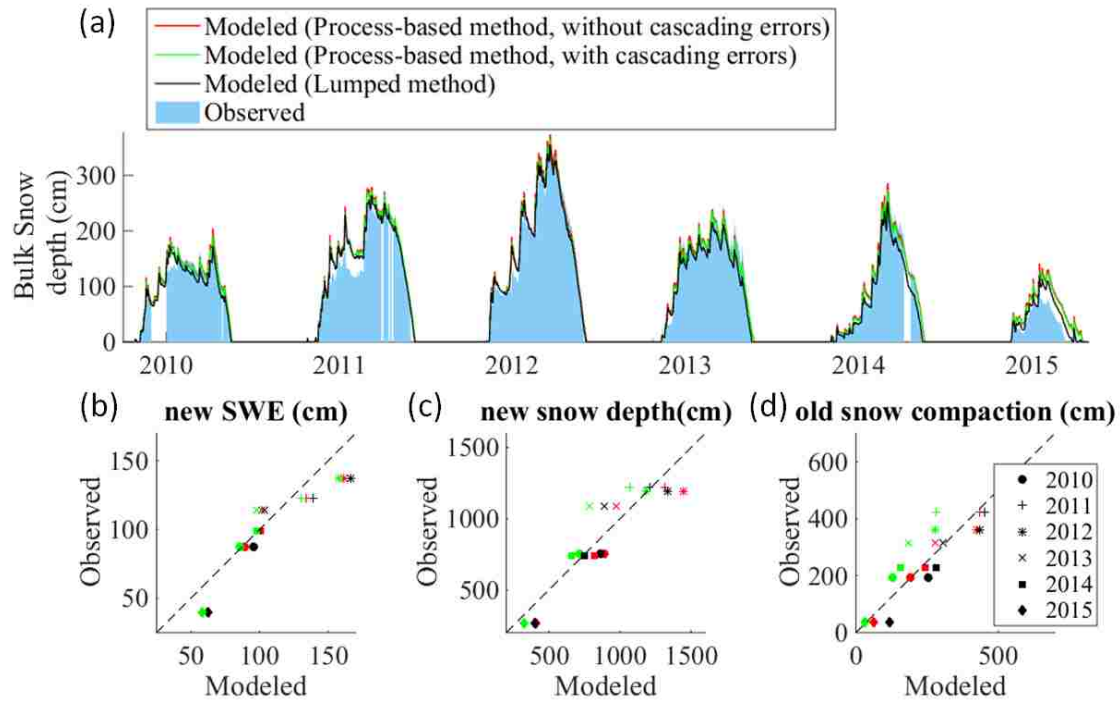


Figure 4-9. Same as Figure 8, but for the evaluation period (water years 2010-2015).

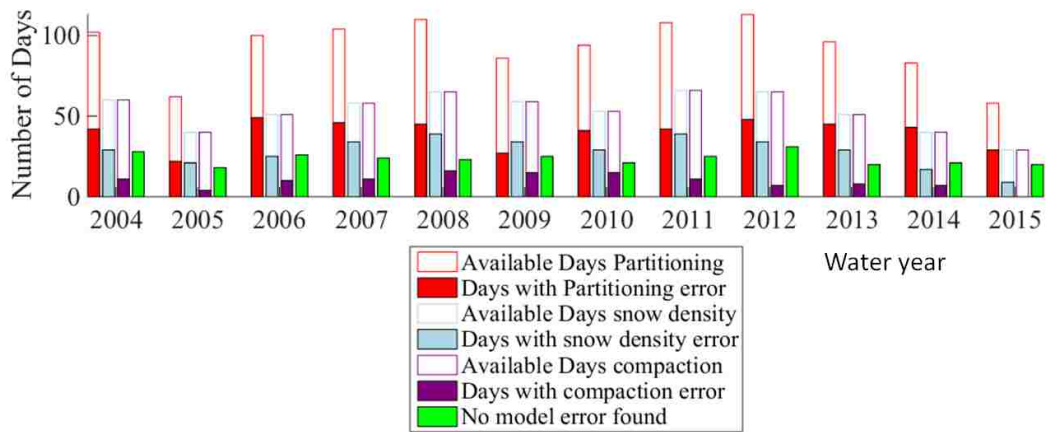


Figure 4-10. Frequency of each source of model daily error (*solid bars*) out of available days where cascading errors were removed (*outline bars*), for each water year.

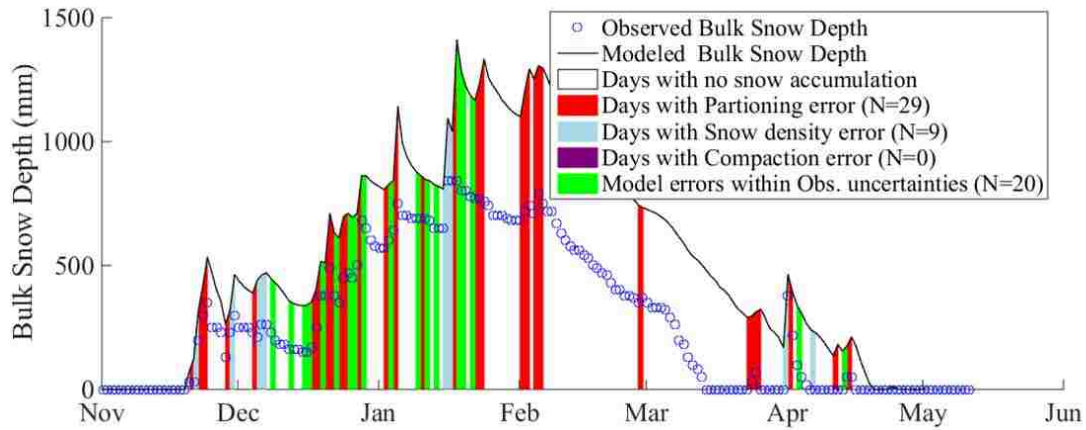


Figure 4-11. Time series of observed and modeled total snow depth for water year 2015. Colors for each day show the identification of the dominate source of model error using the process-based model configuration (without cascading errors). *White* areas show non-accumulation periods that not included in analysis.

Chapter 5. Impacts of Cold Air Intrusions on Snoqualmie Pass Snow

Abstract

Cold air from eastern Washington often flows westward through mountain passes in the Washington Cascades, creating localized inversions and locally depressing climatological temperatures. The persistence of this inversion during a frontal passage can result in complex patterns of snow and rain that are difficult to predict. Yet, these predictions are critical to support highway avalanche control, ski resort operations, and modeling of headwater snowpack storage. In this study we used observations of precipitation phase from a disdrometer and snow depth sensors across Snoqualmie Pass, WA, to evaluate surface-air-temperature-based and mesoscale-model-based predictions of precipitation phase during the 2014-2015 winter. With calibration, the skill of surface-based methods was greatly improved by using air temperature from a nearby higher-elevation station, which was less impacted by surface inversions. When no a prior calibration is performed, we found a hybrid method that combines surface-based predictions with output from the Weather Research and Forecasting mesoscale model to have comparable skill to calibrated surface-based methods. These results suggest that phase prediction in mountain passes can be improved by incorporating observations or models from above the surface layer.

5.1. Introduction

Accurate partitioning of precipitation into rain and snow in mountainous terrain is an important component of hydrological modeling [Maurer and Mass, 2006; Lundquist et al., 2008a; White et al., 2010; Minder et al., 2011; Mizukami et al., 2013], climate sensitivity studies [Minder, 2010], transportation management [Barbara et al., 2008], and avalanche forecasting [Stimberis and Rubin, 2011a]. Existing air temperature (T_{air}) based methods of predicting precipitation phase

show the lowest skill in maritime climates that see frequent transitions between rain and snow. Further, mountain passes represent an added challenge for phase prediction methods because they are influenced by climatologically different air masses [Steenburgh *et al.*, 1997; Sharp and Mass, 2004] and may have multiple freezing levels. Although passes represent a small geographic area of mountainous terrain, improving precipitation phase methods in such regions is important because of the heavy use of passes for transportation, water resources, and recreation.

Methods of partitioning precipitation into rain and snow vary widely, depending on the observations available and application. Here we focus on two methods available in near-real time, with the goal of improving simulations of snowpack accumulation for spring water supply forecasts: 1) using observed near-surface T_{air} with thresholds for rain/snow, and 2) output from a numerical weather prediction model.

Hydrological models most commonly depend on threshold values of near-surface T_{air} [USACE, 1956; Auer, 1974] or wet-bulb temperature [Harder and Pomeroy, 2013] from available mountain stations. Including humidity observations to calculate the wet-bulb or dew-point temperature has been shown to improve phase prediction in continental climates [Harder and Pomeroy, 2013; Marks *et al.*, 2013], but is not always feasible because only 35% of stations measuring snow depth in the U.S. have humidity measurements [Raleigh *et al.*, 2016]. Near-surface T_{air} methods (referred to as surface-based from here on) assume the upper tropospheric temperature and hydrometeor type are correlated with near-surface temperature. However, this is often violated during the passage of frontal systems or within topographically induced cold air pools [Maurer and Mass, 2006; Lundquist and Cayan, 2007; Lundquist *et al.*, 2008a]. Further errors in T_{air} -based partitioning often occur because air temperature must be interpolated between

available station observations. Unfortunately, the location of meteorological observations in mountains is not ideal due to access and power requirements and often poorly reflect terrain-related temperature variations. For example, Figure 5-1a shows the distribution of public roads through the Cascades, which generally follow the lowest elevation path through passes. Figure 5-1b shows the locations of all available stations over the Washington Cascades measuring at least hourly T_{air} . Over 80% of high-elevation (>1000 m) stations are located within 5 km of a paved public road, which means observations have a bias towards sampling mountain passes conditions. Including pass-influenced mountain stations into lapse rate calculations can lead to large errors in prediction of distributed precipitation phase and runoff [Minder *et al.*, 2010].

Short-term forecasts (<3 days) from mesoscale atmospheric models are the primary tool used by flood, avalanche, and transportation forecasters to predict phase at the surface. Because model output is available over large domains, it is an appealing method for modeling snow accumulation. Cloud microphysics that control snow or rain at the surface are represented within mesoscale models using complex parameterizations that have greatly improved in realism during the past years [Khain *et al.*, 2000; Thompson *et al.*, 2004; Minder *et al.*, 2008]. Previous studies have found mesoscale models can accurately simulate snowfall accumulations in mountainous terrain with appropriate grid resolution [Ikeda *et al.*, 2010], but these models may have difficulty within mountain pass environments [Steenburgh *et al.*, 1997].

Each of the two above methods has advantages and disadvantages in terms of representing rain or snow within mountain pass environments. Surface-based approaches enjoy the advantage of a large number of observation locations, many in the areas of most interest (the passes). On the other hand, air temperature in passes is often decoupled from the upper atmosphere where rain or snow is formed and modified; thus surface stations are not

representative of the flow aloft, in which precipitation forms and evolves. In contrast, mesoscale models represent tropospheric temperature structures, but may fail to resolve pass level air flow that is important for local snow accumulations in passes. A combination of information from both methods may provide better predictability of surface phase.

The purpose of this paper is to identify the best method for predicting precipitation phase in a mountain pass environment subject to frequent inversions. To do so, we answer four main questions: 1) Using a surface-based linear threshold model, what is the best source of T_{air} measurement to use? 2) How much is skill improved with local calibration of threshold values? 3) Does the predicted phase from the Weather Research and Forecasting (WRF) [Skamarock and Klemp, 2008] model's microphysical scheme have higher skill than surface-based models? 4) Can information from surface stations and the WRF model be combined to provide improved phase prediction skill than each parent model? We focus our analysis on the Snoqualmie Pass study domain and observational data as described in Section 5.2. Phase prediction methods evaluated are defined in Section 5.3, and results are detailed in Section 5.4. Implications of study results are discussed in section 5.5, and a summary of the main findings in Section 5.6.

5.2. Study domain and data

5.2.1. Snoqualmie Pass

Snoqualmie Pass (Figure 5-2) is located within the larger Stampede Gap area, which forms the second lowest gap in the Washington Cascades (921 m). Weather in the pass is influenced by cold air from eastern Washington as well as frontal systems approaching from the west [Breyfogle, 1986; Steenburgh *et al.*, 1997]. Figure 5-3a shows the climatological wind rose from the heated anemometer at the Dodge Ridge station (see Figure 5-2c) between 2002 and 2015.

Winds are predominantly from the southwest or southeast, which illustrates the strong topographic controls on pass winds (see orientation of the pass in Fig. 2c). During southeast flow, the average December to January (DJF) air temperatures at the Snoqualmie Pass are 2.6°C colder than during southwest flow (Figure 5-3b).

5.2.2. Observations of phase at surface

All stations and observations used are detailed in Table 1. Observations of precipitation phase were made using a PARticle SIze VELOCITY (PARSIVEL-2) disdrometer and multiple acoustic snow depth sensors. The disdrometer was installed for the 2014-2015 winter only at the Snoqualmie Pass snow study site (SNQ) (Figure 5-2c). SNQ is located at the top of the pass saddle within a forest gap. A full site description is provided by *Wayand et al.* (2015a). Laser-optical disdrometer measurements were taken at 10 second intervals and used to classify hydrometeor type based on the diameter-fall-speed relationship [*Battaglia et al.*, 2010]. Hourly snow depth measurements were obtained from SNOTEL and NWAC stations (Figure 5-2c) within 28 km to provide observations of rain or snow for the region surrounding SNQ.

5.2.2. Meteorological Observations

Air temperature records were obtained from Northwest Avalanche Center (NWAC) and Washington State Department of Transportation (WSDOT) stations at the pass (Figure 5-2c). These stations were selected because they provide an approximation of the vertical temperature gradient from the valley floor (921 m) to the ridge top (1667 m). Adjusted to sea-level air pressure was obtained from the Seattle Tacoma (KSEA) and Ellensburg (KELN) airports (Figure 5-2a), to identify the cross-Cascades pressure gradient.

5.3. Methods

Predictions of rain or snow type from a surface-based method and WRF model were evaluated across Snoqualmie Pass during water year 2015 (October-September). The 4-5 January 2015 storm was then used to illustrate persistent issues in both phase prediction methods.

5.3.1. Observations of precipitation phase

Disdrometer measurements at SNQ (Figure 5-2c) of hydrometeor type were classified into ice fraction to allow the evaluation of phase models. All labels of snow, hail, pellets, or graupel, were classified as one, mixed precipitation as 0.5, and rainfall as 0. See Appendix A1 for specific hydrometeor type classifications. The 10-second samples were then aggregated to 10-minute and 1-hour periods by averaging the fraction of frozen hydrometeors within each period. We refer to this value as the snow-fraction, but note this includes all frozen hydrometeors (e.g., snow, hail, pellets, and graupel). Accumulation of snow/ice and rainfall were then calculated by the product of the hourly snow-fraction and accumulated total precipitation at SNQ. Disdrometer observations were available for 83% of the time between October 2014 and March 2015. Manual measurements of 24-h snow depth and SWE accumulation on snow boards, and a snowmelt lysimeter, were also used as a first-order check of disdrometer-derived snow accumulation.

Snotel and NWAC stations surrounding Snoqualmie Pass (Figure 5-2c) were used to derive precipitation phase at 6-h periods. Acoustic samples of snow depth are inherently noisy due to many factors [Anderson and Wirt, 2008]; thus, careful processing was required to extract a precipitation phase signal. First, hourly samples were controlled for outliers or extreme jumps following Meek and Hatfield (1994). Then hourly data were smoothed using a moving 24-h window to remove diurnal cycles caused by sensor unit heating. Finally, precipitation phase was

determined when snow depth increased more than 6 mm (twice the instrument precision of 3 mm) in a 6-h period, which was selected as the minimum time period to avoid false identification of snow accumulation. This methodology was evaluated at the SNQ site where both disdrometer and snow depth sensors were available for water year 2015. The 6-h phase derived from snow depth only had a correlation of determination (r^2) of 0.5 with disdrometer-derived phase, indicating that 50% of the variability was not explained. Therefore, snow-depth derived precipitation phase must be used with caution for model evaluation in rain-snow transitional climates such as Snoqualmie Pass. However, because snow-depth observations are most prevalent in mountainous terrain, we include them in our model evaluation here for completeness.

5.3.2. Precipitation phase methods

Weather and Forecasting Model (WRF)

Archived output from the Weather and Forecasting Model (WRF) was obtained from the Northwest Modeling Consortium [Mass *et al.*, 2003] for water year 2015. This model was selected because it is currently used by NWAC and WSDOT avalanche forecasters at Snoqualmie Pass. The Northwest WRF forecasts use three nested domains (36, 12, 4, and 4/3 km), with the inner most domain covering Washington State. WRF Version 3.6.1 was used with the Thompson microphysical scheme without convective parameterization in the 4/3 km domain. Forecast hours 12-24 were concatenated to provide continuous model output; a product used in previous studies [Minder *et al.*, 2010]. Hourly surface fields and upper air temperature profiles were extracted at 4/3 km grid cells over the study domain (see *black dots* in Figure 5-2c), which just resolves the Snoqualmie Pass valley. WRF snow-fraction was calculated as the fraction of

total frozen precipitation divided by total precipitation for each hour, derived from the microphysical scheme. We refer to this as the WRF microphysical (WRF-MP) method to differentiate from surface-based methods using air temperature from the WRF model, as described below.

Surface-based method

A one or two-threshold linear model based on T_{air} was used as the surface-based method for this study [USACE, 1956; Auer, 1974]. Although other functional forms exist (i.e., sigmoidal [Dai, 2008]), they did not show improved skill over a linear function and therefore were not applied here. The decision to use T_{air} instead of the wet-bulb or dew-point temperature [Harder and Pomeroy, 2013; Marks et al., 2013], was made because saturated conditions at Snoqualmie Pass during precipitating hours resulted in small differences between all three air temperature measures. In addition, using air temperature alone makes these results more applicable to the majority of snow stations (65%) that do not measure humidity [Raleigh et al., 2016].

For each station (SNQ, Dodge Ridge, and Alpental Summit) two linear models were created that use un-calibrated and calibrated threshold values. Un-calibrated models assumed that only snow (rain) fell when the temperatures were less than (greater than) 0°C . Calibrated thresholds temperatures were selected by maximizing the r^2 value between modeled and observed snow-fraction. The parameter space of threshold temperature values ranged from -10°C to 10°C with 0.1°C increments. Calibration was performed using all available hours ($N=576$) during the 2015 water year. We note that the selected threshold values were dependent on the timestep used here (hourly), as has been previously discussed [Harder and Pomeroy, 2013].

Air temperature at 2-m above ground from WRF's land surface model (NOAH) and air temperature from the fourth highest model level (~1129 m a.s.l.) were also used to calibrate threshold values for the surface-based method as described above. The fourth WRF model level above ground was selected because it had the highest correlation (0.62) with phase observations at SNQ. Temperatures from lower layers had only marginally less skill (0.6-0.61), but temperature in layers above 1129 m showed rapidly decreasing skill. We note that a warm bias in 2-m air temperature of the NOAH land surface model has previously been identified [Jin and Miller, 2007; Livneh et al., 2010] and was also found in this study. In addition, over-mixing of the planetary boundary layer during observed inversions is a known challenge for the WRF model [Sterk et al., 2015], which is important within the Snoqualmie Pass area, where surface inversions are common.

Simple hybrid method

A simple, non-calibrated, hybrid method was developed to test if using information from both methods (surface temperatures and WRF model output) resulted in better predictability of surface precipitation phase. Our hypothesis is that the WRF model accurately represents upper air temperatures but fails near the surface due to local inversions. In contrast, near-surface observations of air temperature capture conditions below local inversions, but lack information about the tropospheric conditions aloft. Therefore, we define a simple hybrid method as,

$$Sf_{hybrid} = \frac{Sf_{WRF} + Sf_{SNQ}}{2} \quad \text{Equation 5-1.}$$

where Sf_{WRF} is the snow-fraction predicted by the WRF model's microphysical scheme and Sf_{SNQ} is the snow-fraction predicted from the un-calibrated linear model using air temperature from the SNQ station.

5.3.3. Storm selection and case studies

Figure 5-4 shows the hourly average T_{air} , wind direction, and daily precipitation at Snoqualmie Pass for water year 2015. The largest precipitation events (highlighted in Figure 5-4c) occurred during the passage of warm fronts, consistent with previous studies [Steenburgh *et al.*, 1997]. Between frontal systems, synoptic high pressure dominated and a negative (offshore) pressure gradient existed across the Cascades, which drove east winds through the passes and resulted in the coldest air temperatures of the winter. The 4-5 January event was selected as a case study to illustrate common issues with both surface-based and WRF-model-based predictions of precipitation phase in a pass environment.

5.4. Results

5.4.1. Phase predictability using near-surface T_{air}

Figure 5-5a shows the dependence of 10-minute averaged snow-fraction to near-surface T_{air} at the SNQ site for water year 2015. Figure 5-5b shows the same data expressed as percentage of time within each 0.5°C temperature bin. Frozen precipitation occurred 100% of the time below -3°C , and liquid precipitation occurred more than 80% of the time above $+3^{\circ}\text{C}$, but in between there was an almost equal chance of frozen or liquid precipitation. This result illustrates the known difficulty of methods based on observed near-surface (2-m) temperature to predict precipitation phase, especially in a rain-snow transitional environment where a large fraction of

winter precipitation falls near 0°C (Figure 5-5c). In summary, additional information from the atmosphere aloft is needed to improve poor phase prediction skill ($r^2 = 0.35$) when near-surface temperatures are near zero (-3°C to +3°C).

Figure 5-6 shows the relationships between T_{air} from different stations and the WRF model with the observed fraction-ice at SNQ. Solid lines show the best-fit linear model (highest correlation coefficient between predicted and observed hourly snow-fractions). The highest r^2 values were found using air temperature from the Alpentel Summit station (0.66), followed by the WRF-level (0.61), Dodge Ridge (0.48) and WRF-2m (0.45). Vertical dashed lines show the un-calibrated surface-based model that assumes rain (snow) above (below) 0°C.

5.4.2. Evaluation of phase prediction methods at SNQ station

Snow-fraction

The skill of each method to capture hourly snow-fraction observations at SNQ is shown in Figure 5-7. During all precipitating hours where disdrometer observations were available (N=576), the highest correlation coefficient (r^2) values came from the calibrated surface-based method using T_{air} from the Alpentel Summit station (0.66) and the WRF upper-level (0.60). By design, the calibrated surface-based models had better skill than un-calibrated. However, an important finding was that the phase predicted by the WRF-MP model had higher skill than any un-calibrated single source of air temperature.

The pass-level direction of winds had a large impact on the skill of some models (Figure 5-7c,d). When winds were from the southeast, the SNQ and Dodge Ridge stations' T_{air} values had reduced r^2 values (0.33-0.34) compared to periods when southwest flow dominated (0.72-

0.83) and the majority of total precipitation fell (58%). In contrast, the calibrated Alpental Summit station at the highest-elevation had equally high skill under both wind directions because it was less impacted by surface inversions. Most importantly, the hybrid WRF-SNQ method showed the highest skill during southwest flow of any un-calibrated and most calibrated models.

Snow accumulation

The skill of phase prediction models during the ten wettest storms (Figure 5-7b) is reflected in the annual accumulation of snow water equivalent shown in Figure 5-8. Using air temperature from the SNQ station as a predictor of surface phase resulted in a bias of +30% (+38%) of observations with (without) calibration of rain/snow thresholds. The Alpental Summit model showed a small bias (-1%) in annual accumulation if calibrated, but over-predicted snowfall by +82% of observations without calibration. Modeled snow accumulation from the WRF-MP model under-predicted snowfall accumulation by -52% of observations (*gray solid line*). When WRF precipitation was used instead of SNQ gauge observations, snow accumulations were only slightly reduced (*gray dashed line*). Overall, the hybrid WRF-SNQ model was the best un-calibrated predictor of snow accumulation.

5.4.3. Case study, 4-5 January, 2015

This event was selected to illustrate the major strengths and weakness of both phase prediction methods. The 4-5 January storm included an intense warm front that brought the highest storm precipitation totals (191 mm) at SNQ for the 2015 water year (highlighted in Figure 5-4), with 156 mm (35 mm) falling as rain (snow). Major flooding occurred downstream on the Snoqualmie and the Tolt rivers west of the pass. The jet stream and parent low pressure system passed north of Washington State, bringing the warm front across Snoqualmie Pass summit at

21:00 on 4 January. Wind direction and T_{air} at SNQ were from the southeast and near -3°C until 18:00 4 January, after which the winds shifted to south-west, and T_{air} rose to 0°C by 21:00. The cross-mountain pressure gradient (Seattle Tacoma airport to Ellensburg airport) reached a minimum of -5 mb at 02:00 on 5 January (see Figure 5-4b).

Observations of phase at SNQ (Figure 5-9a) showed light continuous snowfall until 18:00 on 4 January; followed by mixed precipitation transitioning to all rainfall after 19:00. Disdrometer observations were not available after 24:00, but 5 minute lysimeter data and 15 minute snow depth observations (not shown) indicate continuous rainfall after 24:00. Precipitation rates increased during the transition period from 4 mm hr^{-1} to a peak of 15 mm hr^{-1} at 21:00 pm on 4 January (Figure 5-9b).

The hybrid WRF-MP and SNQ method captured the timing of the snow-rain transition the best, with WRF-MP and Alpentel Summit approximately four hours too early, and SNQ four hours too late. In terms of snow and rain totals (Figure 5-9c), the SNQ timing error mattered the most as it occurred during the highest observed rainfall rates when air temperatures at SNQ were between -0.3°C to -0.1°C .

Figure 5-10 shows the vertical profile of T_{air} from available surface stations and WRF modeled layer temperatures. Prior to the transition period, the WRF temperatures were too warm by $4-6^{\circ}\text{C}$ and did not capture the persistence of the near surface inversion. However, the surface cold air appeared to have little effect on the observed phase at the surface in this case, due to its shallow depth (~ 200 m). The inversion caused phase predictions using SNQ T_{air} to fail (predicting snow), while the higher-elevation stations sampled air temperatures more representative of the average temperatures that hydrometeors fell through.

Distributed model values and observations of snow-fraction surrounding Snoqualmie Pass at 6-h intervals are shown in Figure 5-11. Background colors show WRF modeled snow-fraction derived from the Thompson scheme. Similar to results at the SNQ station, WRF transitions to rain between 12:00 and 18:00 at stations west of the pass while station observations show continued snow fall. Between 18:00 to midnight of the 4 January, only Snoqualmie Pass (SNQ) and Stamped Pass (SPP) show observed snowfall, while WRF predicted all rainfall. Finally, between 00:00 and 06:00 on the 5 January, the remaining observations east of the pass switch to rain.

5.5. Discussion

5.5.1. Recommendation for best rain-snow partitioning method at Snoqualmie Pass

Results showed that the best method for predicting rain-snow partitioning varied depending on the availability of observations at Snoqualmie Pass. The highest predictive skill was found when the ridge-top station (Alpentel Summit) air temperature was used with pass-level observations (SNQ's disdrometer) to calibrate ideal rain-snow thresholds (Figure 5-7). This skill was reduced by half if default rain-snow thresholds (0°C) were used (i.e. no calibration). An intermediate method (not shown) that adjusted air temperature at Alpentel Summit using the average local lapse rate (-5.5°C) and partition precipitation using the default threshold found no improvement over using air temperature from the SNQ station itself. Finally, we note that air temperature observations are not always available or reliable at higher-elevations above passes (e.g., Alpentel Summit was hit by lightning the summer of 2015), thus the best method to predict rain-snow partition may vary by location.

Using predicted phase from the WRF-MP model is appealing because of its widespread availability, yet at SNQ for water year 2015 we found significant under accumulations of snowfall (Figure 5-8). Overall, we recommend using the simple hybrid method at Snoqualmie Pass because it showed the highest skill during the ten wettest storms of water year 2015 without local calibration (Figure 5-7). While we could not test this method during other years or at other locations, it suggests that combining information from the WRF model and surface observations can provide better predictions of phase locations subject to local inversions.

5.5.2. Frequency of inversions during precipitation at SNQ

Surface inversions at and east of Snoqualmie Pass are a common feature during regional high pressure periods between low-pressure systems [Breyfogle, 1986]. Analysis of the local lapse rate between the SNQ and Alpental Summit stations between 2003 and 2015 showed that they occurred on average 25% of the time during DJF months and could reach +20 °C/km in intensity. Water year 2015 had the highest occurrence of inversions (30%) over the analyzed period. The main impacts of such an inversion are to keep T_{air} and snowpack temperatures colder at Snoqualmie Pass than non-gap locations during clear weather periods. However, the persistence of such cold air can also impact the amount of precipitation on downwind slopes [Stiler *et al.*, in press], freezing rain occurrence [Sharp and Mass, 2004], and precipitation phase during transition periods from regional high to low pressure (i.e. the 4-5 January event). At SNQ, for the DJF months of water years 2003-2015, an average of 128 mm of precipitation fell during an inversion, or 14% of average total DJF precipitation (1009 mm). During WY 2015, 235 mm (23%) of precipitation fell through an inversion, of which only 21 mm was snow and 160 mm rain (54 mm fell when disdrometer observations not available).

5.6. Conclusion

Two common methods of partitioning precipitation into rain and snow were evaluated with disdrometer observations in a mountain pass environment (the Cascades of Washington State) during water year 2015. During storms that brought the majority of winter precipitation, it was shown that air temperature from a nearby higher-elevation station (Alpental Summit at 1667 m) was a better predictor for precipitation phase at the pass (921 m) than temperature measured at the pass itself (921 m). This suggests that ridge-top stations measure air temperatures more representative of the environment hydrometeors are exposed to, compared to pass level stations that are impacted more by surface inversions. Because the majority of mountain stations in the Washington Cascades are located near mountain passes (Figure 5-1) gridded data sets should incorporate a station's topographic index, to improve phase predictions derived from gridded air temperature.

Finally, the best method that did not require calibration was a simple hybrid approach that combined an un-calibrated surface-based model at pass level with WRF mesoscale model output. Because the biases in snow-fraction from both parent models (WRF-MP and SNQ un-calibrated) were opposite due to local surface inversions, we expect the simple hybrid method to perform well over other mountain ranges where inversions are frequent (e.g. Canadian Rockies [Vionnet *et al.*, 2015]). Overall, these findings suggest that phase prediction in mountain passes can be improved by incorporating observations or models of the atmosphere above the surface layer.

5.7. Tables

Table 5-1. Stations used in study.

Network ¹	Observed Variables ²	Station Name	Elevation (m)	Latitude	Longitude
UW, WSDOT	PT, T _{air} , P, SD	Snoqualmie pass (SNQ)	921	47.4249	-121.4139
WSDOT	T _{air} , WS, WD	Dodge Ridge	1146	47.4207	-121.4292
NWAC	T _{air}	Alpental Summit	1667	47.4388	-121.4427
	T _{air}	Alpental Mid	1326	47.4341	-121.4348
	T _{air}	Alpental Base	945	47.4441	-121.4248
SNOTEL	SD	Meadows Pass	1067	47.2831	-121.4720
	SD	Mt. Gardner	914	47.3577	-121.5680
	SD	Olallie Meadows	1128	47.3741	-121.4421
	SD	Rex River	1219	47.3020	-121.6048
	SD	Stampede Pass	1177	47.2745	-121.3416
	SD	Tinkham Creek	936	47.3322	-121.4695
NWS/FAA	PR	SeaTac Airport (KSEA)	532	47.0338	-120.5313
NWS/FAA	PR	Ellensburg Bowers Field (KELN)	130	47.4447	-122.3136

¹ Networks names refer to: University of Washington (UW), Washington State Department of Transportation (WSDOT), North West Avalanche Center (NWAC), Natural Resources Conservation Service Snow Telemetry (SNOTEL)

² Abbreviations: precipitation type (PT), near-surface air temperature (T_{air}), total precipitation (P), snow depth (SD), wind speed (WS), wind direction (WD), air pressure (PR).

5.8. Figures

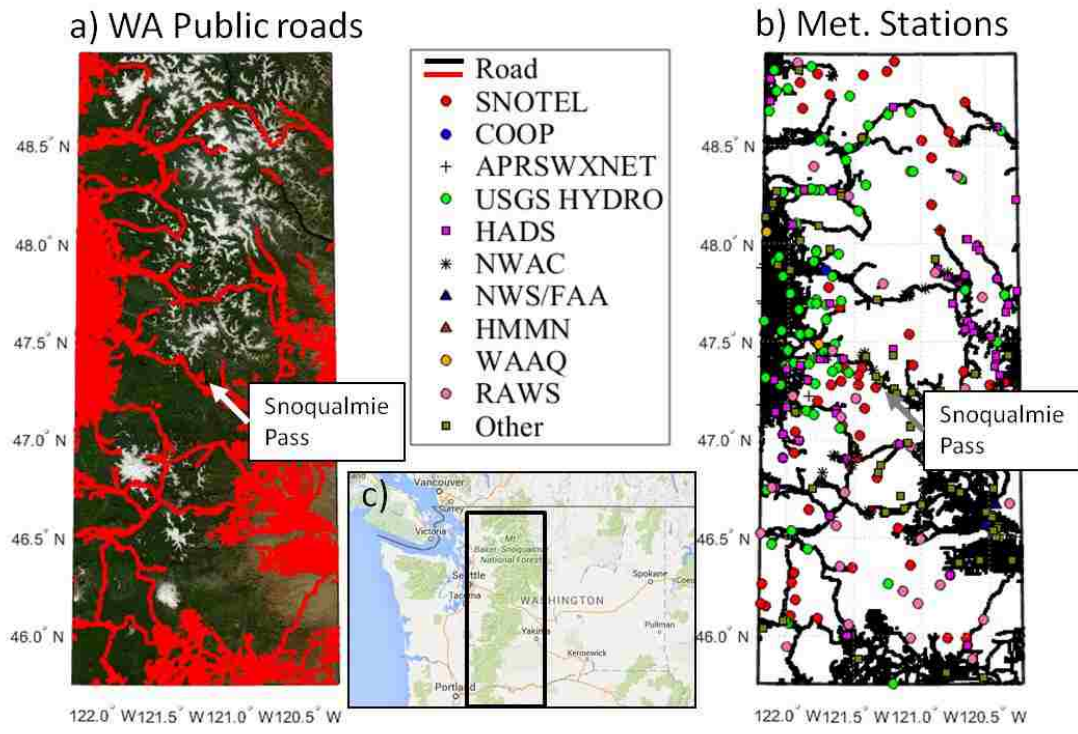


Figure 5-1. (a) Public roads (red) through major mountain pass of the Washington Cascades. (b) Locations of available meteorological stations measuring at least air temperature at a hourly resolution as of February 2016. (c) Regional map

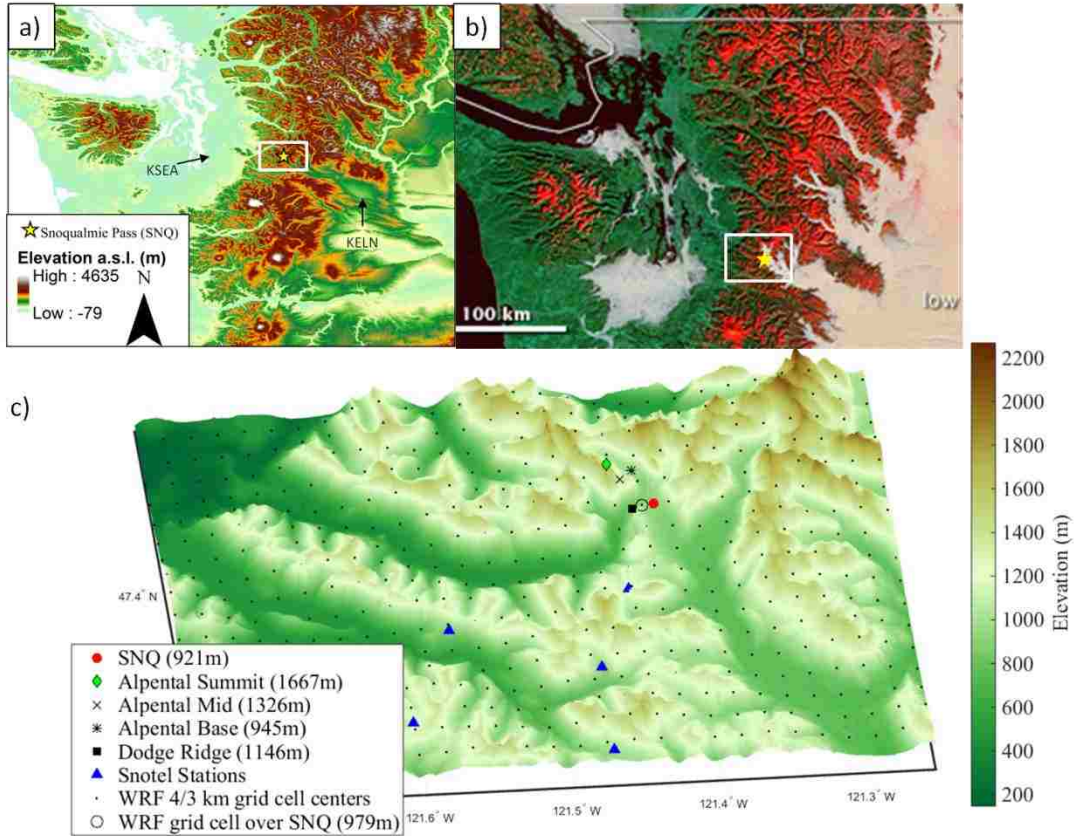


Figure 5-2. (a) Washington Cascades and Snoqualmie Pass study domain (b) False color MODIS image on January 10 2009 showing extent of low clouds east of passes during a period of high pressure over Washington State in between storm systems. (c) Snoqualmie Pass study domain (White boxes in (a) and (b)), showing the locations of stations used in analysis. *Black dots* show the center of 4/3 km WRF grid cells, which marginally resolve the pass valley. Precipitation phase was mainly evaluated at the SNQ station (*red circle*) using disdrometer observations.

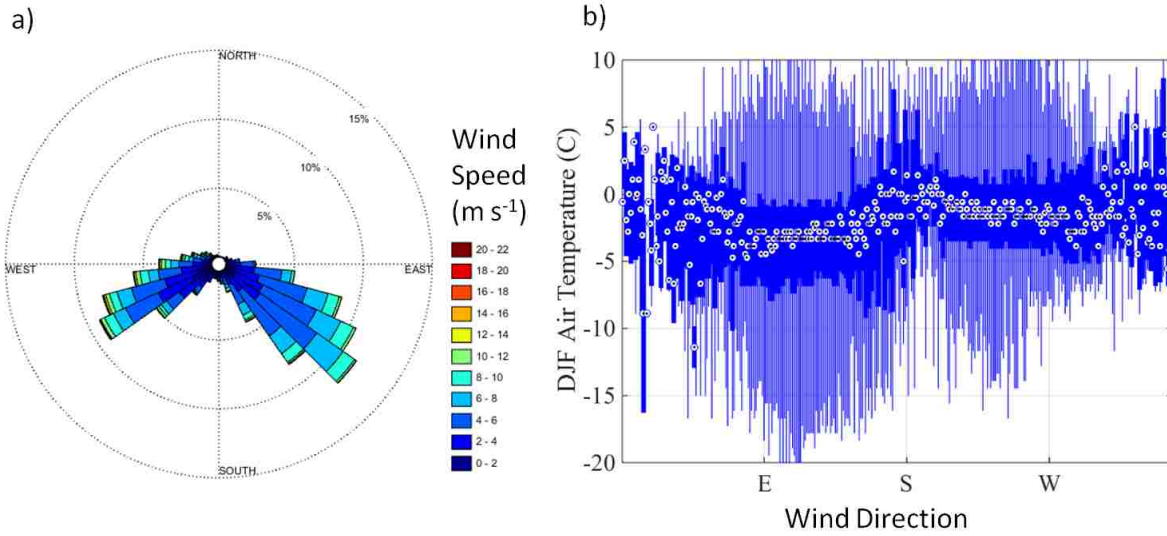


Figure 5-3. Climatological wind roses during winter (DJF) at the Dodge Ridge station located at the summit (1146 m) of Snoqualmie Pass (a), and hourly averaged air temperature during DJF as a function of wind direction (b). For each 1° wind direction bin, white circles show the median DJF air temperature, dark blue lines show the 25th and 75th percentiles, and line blue lines the max and min temperatures.

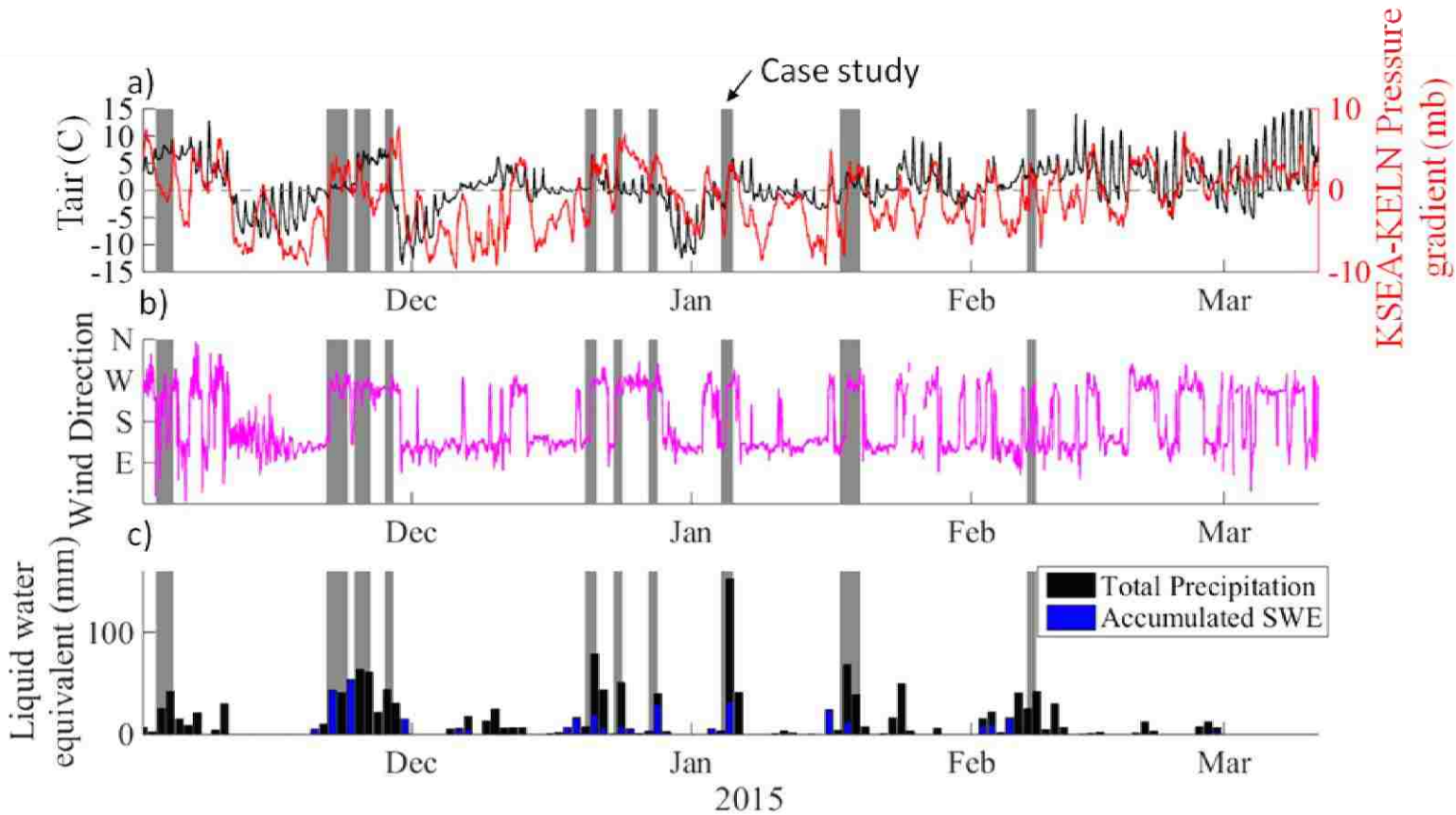


Figure 5-4. Observations from Snoqualmie Pass during water year 2015. Grey boxes highlight largest 10 storms by precipitation totals. (a) Air temperature from SNQ and cross-pass pressure gradient between KSEA to KELN, (b) Wind direction at the Dodge Ridge station, (c) Daily accumulated total gauge precipitation and measured SWE accumulation (via manual snow board measurements) at SNQ.

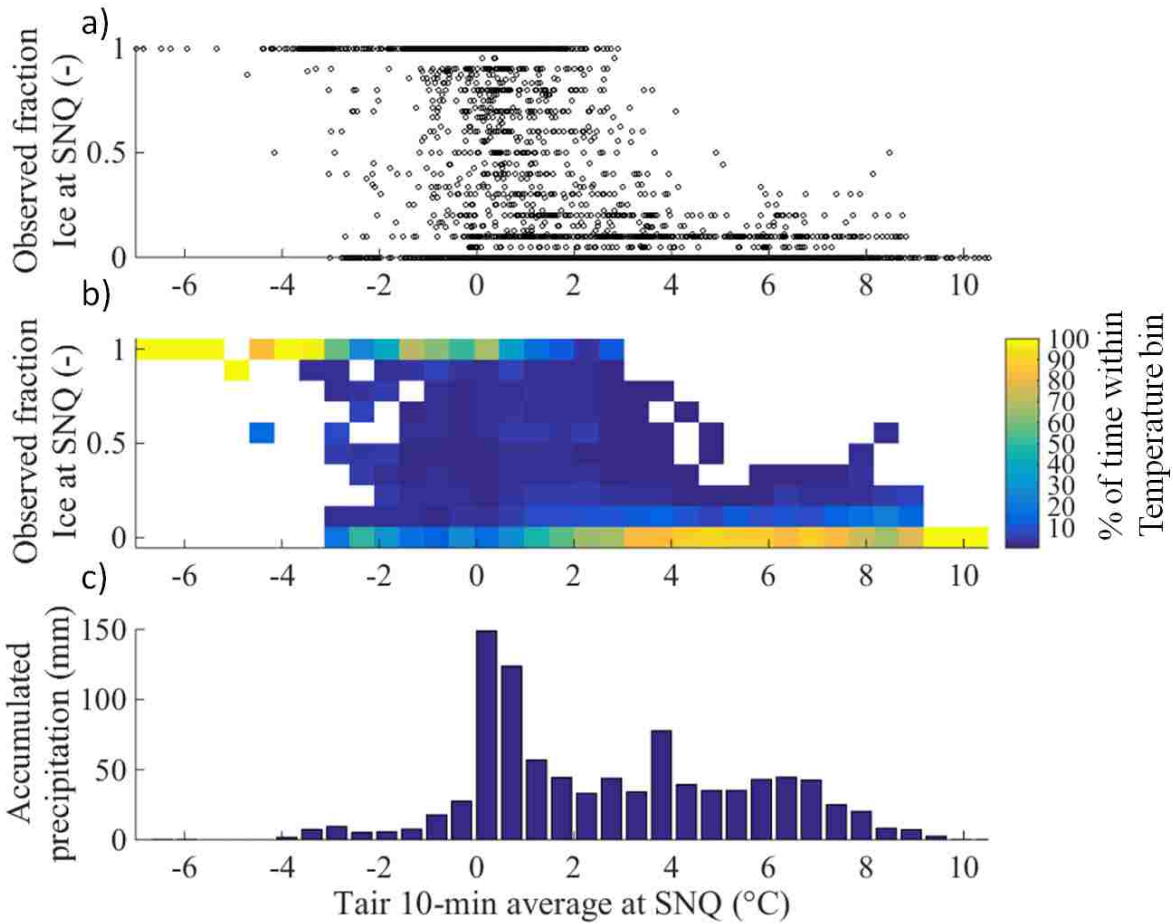


Figure 5-5. (a) Fraction of precipitation observed as ice (snow, graupel, hail etc.) within 10 min period by disdrometer observations compare to 10 minute air temperature averages. (b) Same observational data binned by 0.5°C x 0.1 snow-fraction bins, showing likelihood of snow/rain at each temperature range. (c) Total precipitation observed at SNQ during as a function of air temperature.

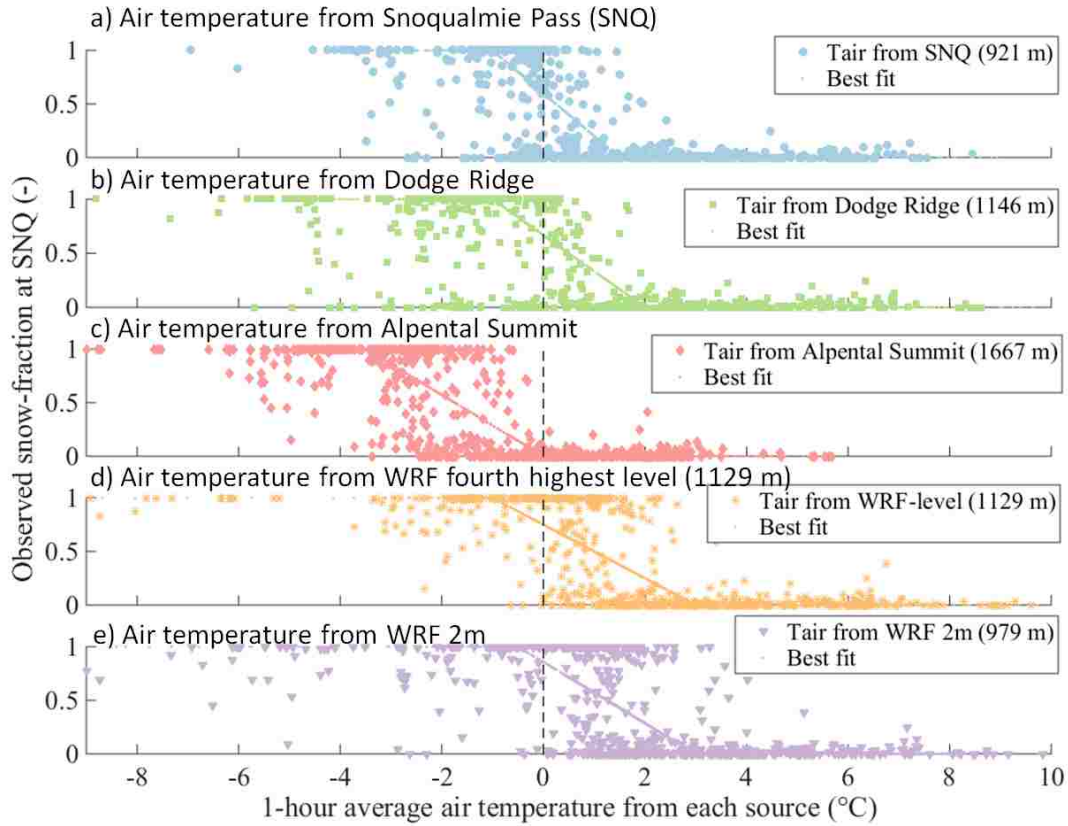


Figure 5-6. Observed fraction ice at SNQ versus observed 1 hour average air temperature at nearby pass stations and the nearest WRF grid cell. Solid line shows best fit linear model and vertical dashed line shows the un-calibrated model with an assumed threshold of 0°C.

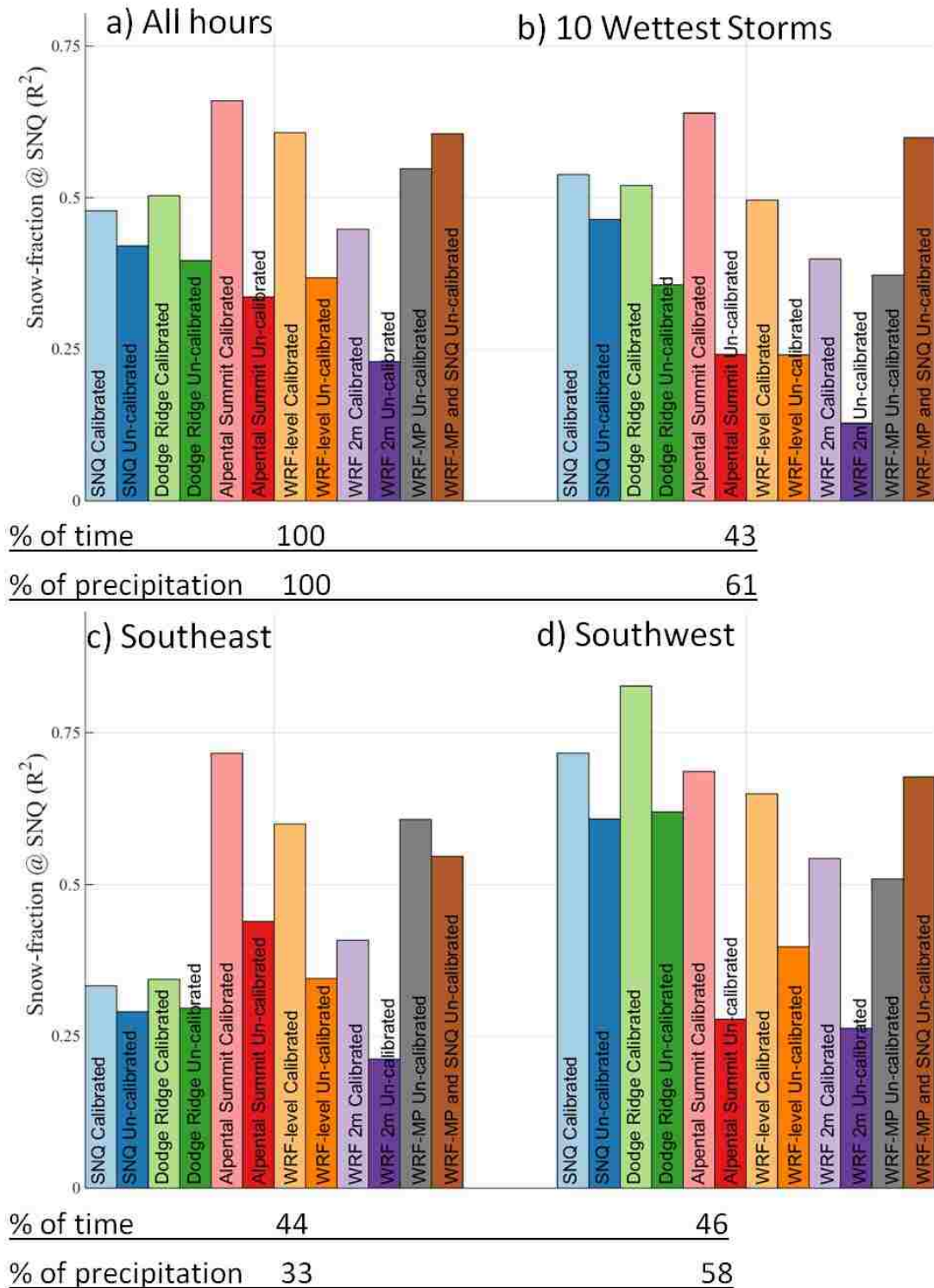


Figure 5-7. Coefficients of determination (r^2) between hourly distrometer observations of snow-fraction and model predicted snow-fraction. Subplots separate water year 2015 into (a) all available hours (N=576), (b) the 10 wettest storms (highlighted in Figure 5-4), and (c,d) by wind

directions as observed at the Dodge Ridge station. Below the x-axis shows the percentage of time and total precipitation observed during each period at the SNQ station when disdrometer observations were available

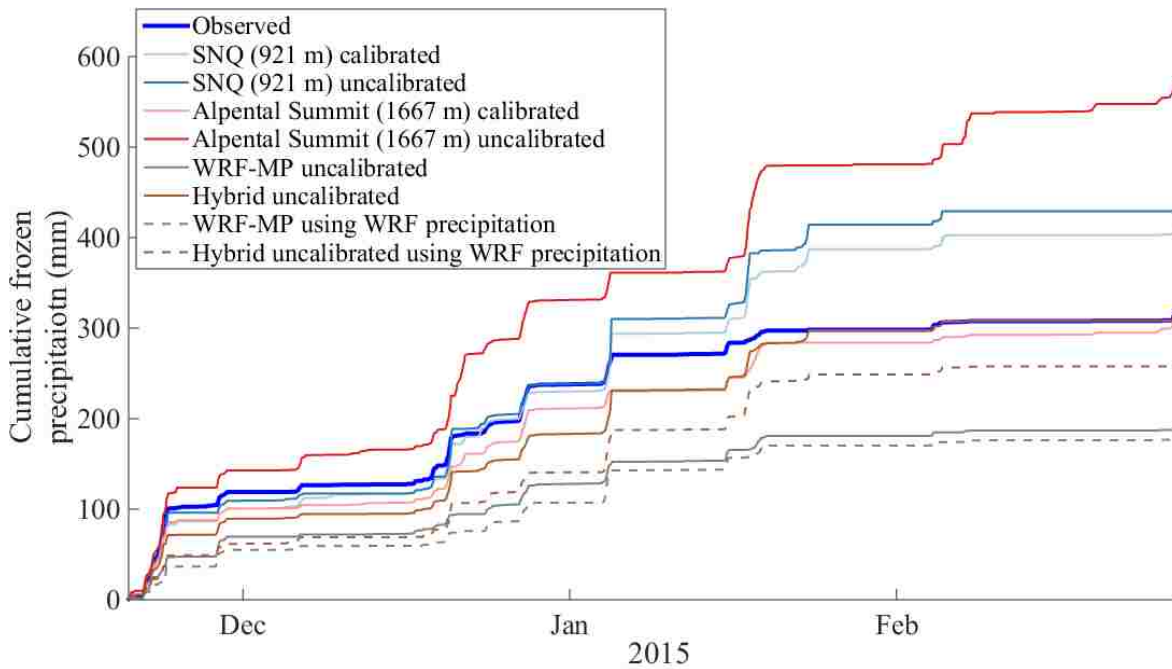


Figure 5-8. Total winter accumulation of snow water equivalent (SWE) observed and modeled at SNQ. Observed values are the product of disdrometer hourly snow-fraction and gauge observed precipitation. Modeled values are the product of predicted snow-fraction and gauge observed precipitation (solid lines) or WRF modeled precipitation (dashed lines).

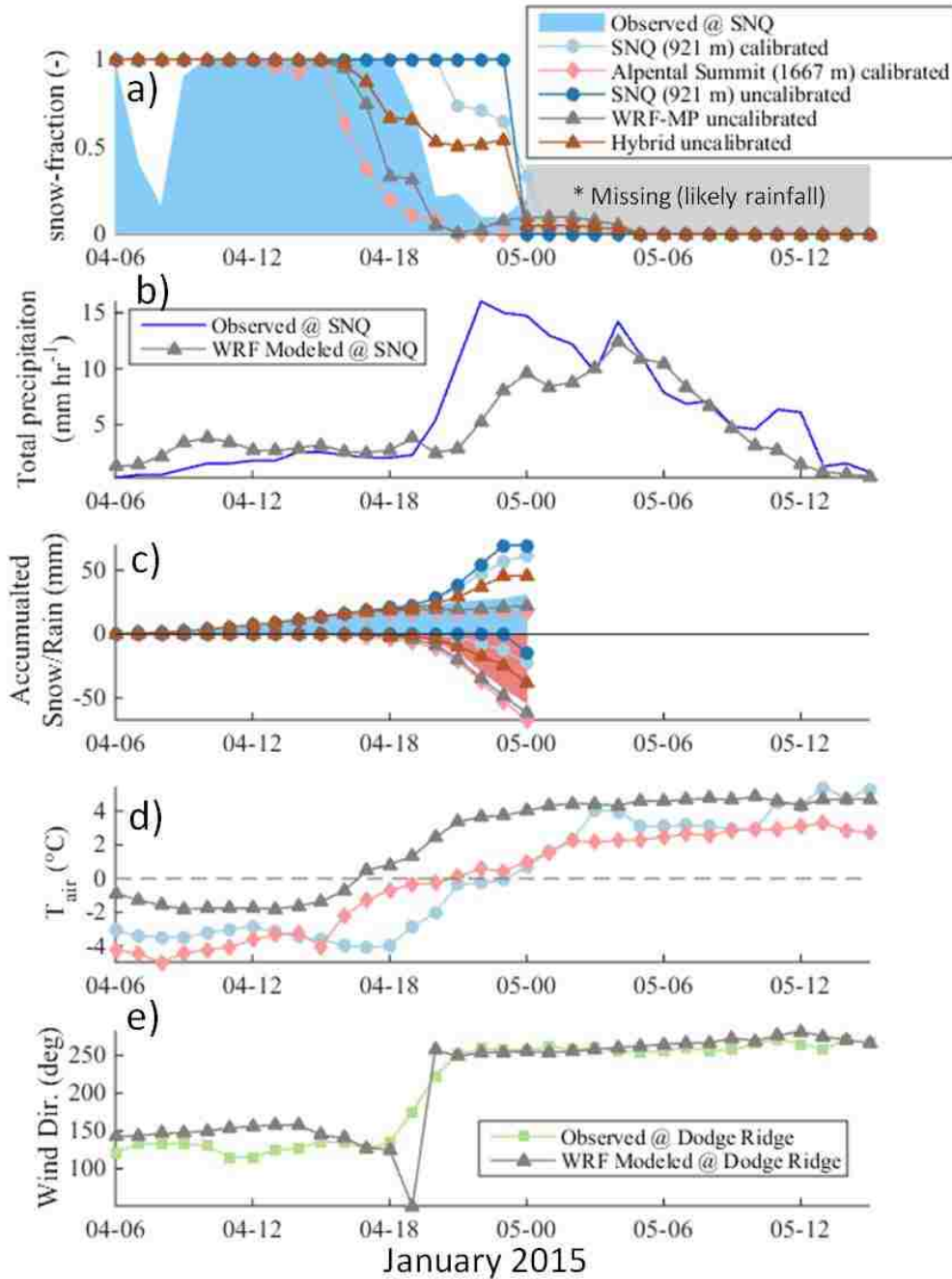


Figure 5-9. 4-5 January 2015 case study. Observed and modeled (a) snow-fraction, (b) total precipitation rate, (c) cumulative frozen and liquid precipitation, (d) 2-m air temperature, (e) wind direction. *Disdrometer error codes prevented quality data but in-situ snow depth, lysimeter, and snow board observations indicate rainfall (not shown).

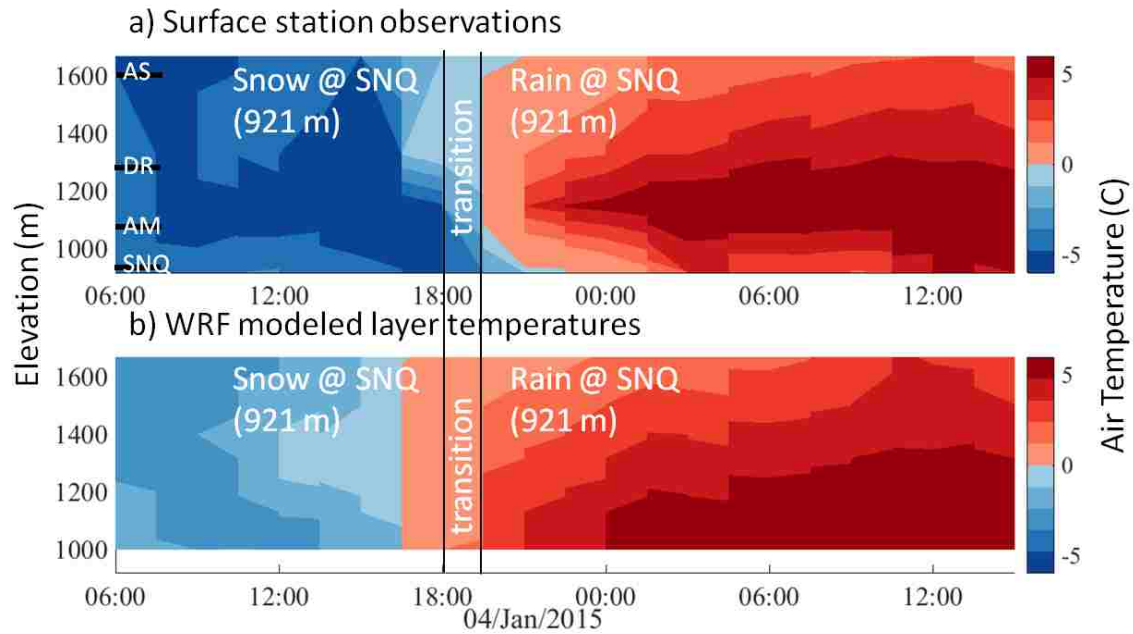


Figure 5-10. (a) Observed air temperature at Snoqualmie Pass during the 4-5 January 2015 event. Black horizontal lines show elevations and abbreviations of surface stations used (Alpental Summit (AS), Dodge Ridge (DR), Alpental Middle (AM), and Snoqualmie Pass (SNQ)). (b) WRF modeled air temperature at near surface layers. Temperatures have been linearly interpolated between stations and WRF layers.

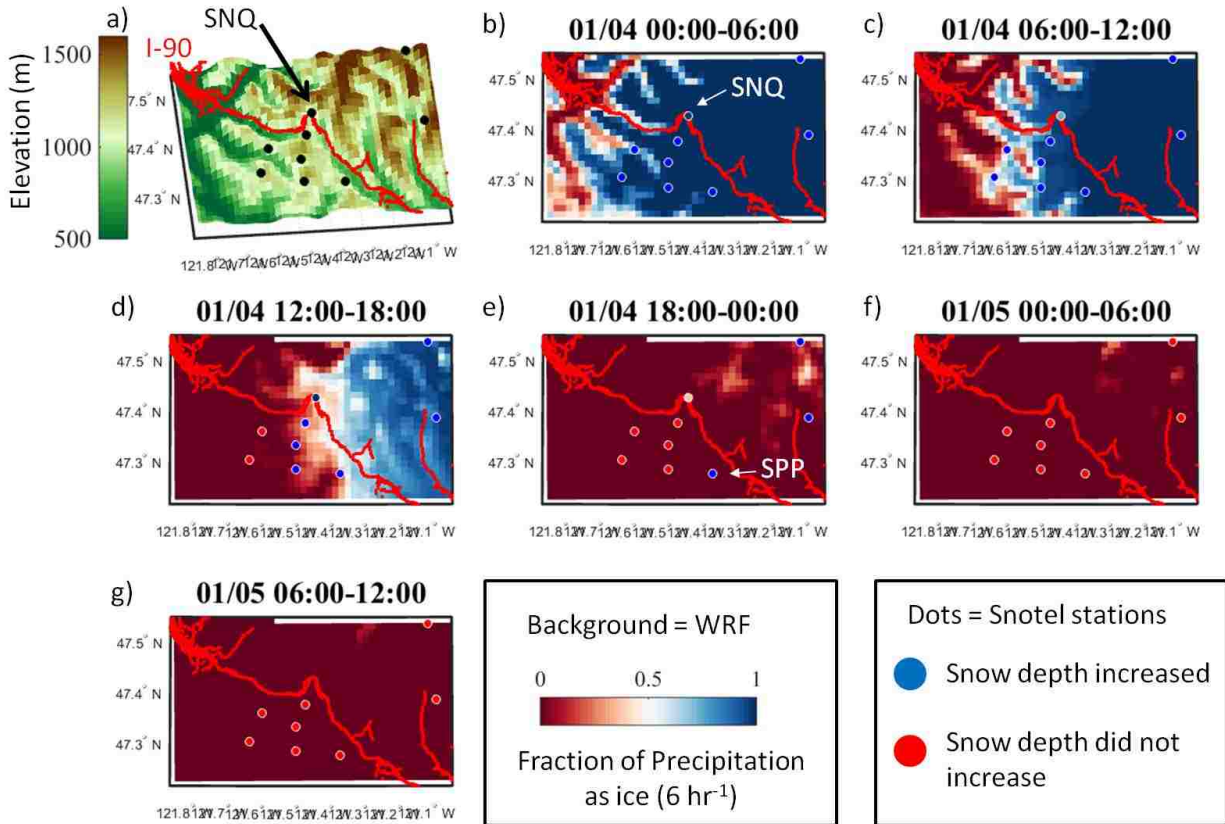


Figure 5-11. 4-5 January 2015 case study. (a) Domain of Snoqualmie Pass (shown in insert of Figure 1a) with locations of stations observing precipitation phase. (b-g) Background color shows WRF predicted fraction of 6 hour precipitation as ice. The annotated circle in (a) shows SNQ disdrometer observations of precipitation phase. *Blue (red) circles* indicate snowfall (rainfall), as derived from the 6 hour change in SNOTEL snowdepth. The Stampede Pass (SPP) station is annotated because it is located in the next pass to the south, where snowfall lasts longer during this event.

5.9. Appendix A

Table A1. Precipitation type and defined snow-fraction.

WMO Code	WMO Description	snow-fraction	% of available observations
1	'Cloud generally dissolving or becoming less developed'	-	0
2	'State of sky on the whole unchanged'	-	0
3	'Clouds generally forming or developing'	-	0

4	'Visibility reduced by smoke, e.g. veldt or forest fires, industrial smoke or volcanic ashes'	-	0
5	'Haze'	-	0
6	'Widespread dust in suspension in the air, not raised by wind at or near the station at the time of observation'	-	0
7	'Dust or sand raised by wind at or near the station at the time of observation, but not well-developed dust whirl(s) or sand whirl(s), and no duststorm or sandstorm seen; or, in the case of ships, blowing spray at the station'	-	0
8	'Well-developed dust or sand whirl(s) seen at or near the station during the preceding hour or at the time of observation, but no dust storm or sandstorm'	-	0
9	'Duststorm or sandstorm within sight at the time of observation, or at the station during the preceding hour'	-	0
10	'Mist'	-	0
11	'Patches of shallow fog or ice fog at the station, whether on land or sea not deeper than about 2 metres on land or 10 metres at sea'	-	0
12	'More or less continuous shallow fog or ice fog at the station, whether on land or sea, not deeper than about 2m/land or 10m/sea'	-	0
13	'Lightning visible, or thunder heard'	-	0
14	'Precipitation within sight, not reaching the ground or the surface of the sea'	-	0
15	'Precipitation within sight, reaching the ground or the surface of the sea, but distant, i.e. > 5 km from the station'	-	0
16	'Precipitation within sight, reaching the ground or the surface of the sea, near to, but not at the station'	-	0
17	'Thunderstorm, but no precipitation at the time of observation'	-	0
18	'Squalls at or within sight of the station during the preceding hour or at the time of observation'	-	0
19	'Funnel clouds at or within sight of the station during the preceding hour or at the time of observation'	-	0

20	'Drizzle (not freezing) or snow grains, not falling as showers, during the preceding hour but not at the time of observation'	-	0
21	'Rain (not freezing), not falling as showers, during the preceding hour but not at the time of observation'	-	0
22	'Snow, not falling as showers, during the preceding hour but not at the time of observation'	-	0
23	'Rain and snow or ice pellets, not falling as showers; during the preceding hour but not at the time of observation'	-	0
24	'Freezing drizzle or freezing rain; during the preceding hour but not at the time of observation'	-	0
25	'Shower(s) of rain during the preceding hour but not at the time of observation'	-	0
26	'Shower(s) of snow, or of rain and snow during the preceding hour but not at the time of observation'	-	0
27	'Shower(s) of hail, or of rain and hail during the preceding hour but not at the time of observation'	-	0
28	'Fog or ice fog during the preceding hour but not at the time of observation'	-	0
29	'Thunderstorm (with or without precipitation) during the preceding hour but not at the time of observation'	-	0
30	'Slight or moderate duststorm or sandstorm has decreased during the preceding hour'	-	0
31	'Slight or moderate duststorm or sandstorm no appreciable change during the preceding hour'	-	0
32	'Slight or moderate duststorm or sandstorm has begun or has increased during the preceding hour'	-	0
33	'Severe duststorm or sandstorm has decreased during the preceding hour'	-	0
34	'Severe duststorm or sandstorm no appreciable change during the preceding hour'	-	0
35	'Severe duststorm or sandstorm has begun or has increased during the preceding hour'	-	0
36	'Slight/moderate drifting snow generally low (below eye level)'	-	0
37	'Heavy drifting snow generally low (below eye level)'	-	0

38	'Slight/moderate blowing snow generally high (above eye level)'	-	0
39	'Heavy blowing snow generally high (above eye level)'	-	0
40	'Fog or ice fog at a distance at the time of observation, but not at station during the preceding hour, the fog or ice fog extending to a level above that of the observer'	-	0
41	'Fog or ice fog in patches'	-	0
42	'Fog/ice fog, sky visible, has become thinner during the preceding hour'	-	0
43	'Fog/ice fog, sky invisible, has become thinner during the preceding hour'	-	0
44	'Fog or ice fog, sky visible, no appreciable change during the past hour'	-	0
45	'Fog or ice fog, sky invisible, no appreciable change during the preceding hour'	-	0
46	'Fog or ice fog, sky visible, has begun or has become thicker during preceding hour'	-	0
47	'Fog or ice fog, sky invisible, has begun or has become thicker during the preceding hour'	-	0
48	'Fog, depositing rime, sky visible'	-	0
49	'Fog, depositing rime, sky invisible'	-	0
50	'Drizzle, not freezing, intermittent, slight at time of ob.'	0	0
51	'Drizzle, not freezing, continuous, slight at time of ob.'	0	4
52	'Drizzle, not freezing, intermittent, moderate at time of ob.'	0	0
53	'Drizzle, not freezing, continuous, moderate at time of ob.'	0	1
54	'Drizzle, not freezing, intermittent, heavy at time of ob.'	0	0
55	'Drizzle, not freezing, continuous, heavy at time of ob.'	0	1
56	'Drizzle, freezing, slight'	1	0
57	'Drizzle, freezing, moderate or heavy (dense)'	1	0
58	'Rain and drizzle, slight'	0	15
59	'Rain and drizzle, moderate or heavy'	0	10
60	'Rain, not freezing, intermittent, slight at time of ob.'	0	0

61	'Rain, not freezing, continuous, slight at time of ob.'	0	5
62	'Rain, not freezing, intermittent, moderate at time of ob.'	0	0
63	'Rain, not freezing, continuous, moderate at time of ob.'	0	23
64	'Rain, not freezing, intermittent, heavy at time of ob. '	0	0
65	'Rain, not freezing, continuous, heavy at time of ob.'	0	4
66	'Rain, freezing, slight'	0.5	0
67	'Rain, freezing, moderate or heavy'	0.5	0
68	'Rain or drizzle and snow, slight'	0.5	0
69	'Rain or drizzle and snow, moderate or heavy'	0.5	1
70	'Intermittent fall of snowflakes, slight at time of ob.'	1	0
71	'Continuous fall of snowflakes, slight at time of ob.'	1	8
72	'Intermittent fall of snowflakes, moderate at time of ob.'	1	0
73	'Continuous fall of snowflakes, moderate at time of ob.'	1	14
74	'Intermittent fall of snowflakes, heavy at time of ob.'	1	0
75	'Continuous fall of snowflakes, heavy at time of ob.'	1	3
76	'Diamond dust (with or without fog)'	1	0
77	'Snow grains (with or without fog)'	1	0
78	'Isolated star-like snow crystals (with or without fog)'	1	0
79	'Ice pellets'	1	0
80	'Rain shower(s), slight'	0	0
81	'Rain shower(s), moderate or heavy'	0	0
82	'Rain shower(s), violent'	0	0
83	'Shower(s) of rain and snow, slight'	1	0
84	'Shower(s) of rain and snow, moderate or heavy'	1	0
85	'Snow shower(s), slight'	1	0
86	'Snow shower(s), moderate or heavy'	1	0
87	'Shower(s) of snow pellets or small hail, with or without rain or rain and snow mixed slight'	1	1
88	'Shower(s) of snow pellets or small hail, with or without rain or rain and snow mixed moderate or heavy'	1	9

89	'Shower(s) of hail, with or without rain or rain and snow mixed, not associated with thunder slight'	1	0
90	'Shower(s) of hail, with or without rain or rain and snow mixed, not associated with thunder moderate or heavy'	1	1
91	'Slight rain at time of observation Thunderstorm during the preceding hour but not at time of observation'	-	0
92	'Moderate or heavy rain at time of observation Thunderstorm during the preceding hour but not at time of observation'	-	0
93	'Slight snow, or rain and snow mixed or hail at time of observation - Thunderstorm during the preceding hour but not at time of observation'	-	0
94	'Moderate or heavy snow, or rain and snow mixed or hail at time of observationThunderstorm during the preceding hour but not attime of observation'	-	0
95	'Thunderstorm, slight or moderate, without hail, but with rain and/or snow attime of observation'	-	0
96	'Thunderstorm, slight or moderate, with hail at time of ob.'	-	0
97	'Thunderstorm, heavy, without hail, but with rain and/or snow at time ofobservation'	-	0
98	'Thunderstorm combined with dust/sandstorm at time of observation'	-	0
99	'Thunderstorm, heavy with hail at time of observation '	-	0

References

Anderson, E. A. (1976), A point energy and mass balance model of a snow cover, Silver Spring, Md. : Office of Hydrology, National Weather Service,.

Anderson, J., and J. Wirt (2008), Ultrasonic Snow Depth Sensor Accuracy, Reliability, and Performance, in Proceedings of the 76th Annual Western Snow Conference, pp. 99–102.

Andreadis, K. M., P. Storck, and D. P. Lettenmaier (2009), Modeling snow accumulation and ablation processes in forested environments, *Water Resour. Res.*, 45(5), 1–13, doi:10.1029/2008WR007042.

Anon (2008), Draft Background Report on Friant Dam Operations.

Auer, A. H. (1974), The Rain versus Snow Threshold Temperatures, 27, 67.

Barbara L, George X, Buell To, Moore D, Austin B, Wang Y-J. (2008), Storm-related closures of I-5 and I-90 : Freight Transportation Economic Impact Assessment Report, WA. Available at: <http://www.wsdot.wa.gov/research/reports/fullreports/708.1.pdf>

Battaglia, A., E. Rustemeier, A. Tokay, U. Blahak, and C. Simmer (2010), PARSIVEL snow observations: A critical assessment, *J. Atmos. Ocean. Technol.*, 27(2), 333–344, doi:10.1175/2009JTECHA1332.1.

Berris, S., and R. Harr (1987), Comparative snow accumulation and melt during rainfall in forested and clear-cut plots in the western Cascades of Oregon, *Water Resour. Res.*, 23(1), 135–142.

Biggs, T. W., and T. M. Whitaker (2012), Critical elevation zones of snowmelt during peak discharges in a mountain river basin, *J. Hydrol.*, 438-439, 52–65, doi:10.1016/j.jhydrol.2012.02.048.

Bohn, T. J., B. Livneh, J. W. Oyster, S. W. Running, B. Nijssen, and D. P. Lettenmaier (2013), Global evaluation of MTCLIM and related algorithms for forcing of ecological and hydrological models, *Agric. For. Meteorol.*, 176, 38–49, doi:10.1016/j.agrformet.2013.03.003.

Boone, A. (2002), Description du schema de neige ISBA-ES (Explicit Snow), *Cent. Natl. Rech.*

Boone, A., and P. Etchevers (2001), An intercomparison of three snow schemes of varying complexity coupled to the same land surface model: Local-scale evaluation at an Alpine site, *J. Hydrometeorol.*, (class 2), 374–394.

Breyfogle, S. R. (1986), Growth Characteristics of Hoarfrost With Respect to Avalanche Occurrence, Olympia.

Buck, A. L. (1981), New equations for computing vapor pressure and enhancement factor., *J. Appl. Meteorol.*, 20(12), 1527–1531, doi:10.1175/1520-0450(1981)020<1527:NEFCVP>2.0.CO;2.

Bureau of Reclamation (2005), Flood Damage Reduction Technical Appendix.

Campbell, G. S., and J. M. Norman (1998), *An introduction to environmental biophysics*, 2nd ed., Springer-Verlag, New York.

Clark, M. P., D. Kavetski, and F. Fenicia (2011a), Pursuing the method of multiple working hypotheses for hydrological modeling, *Water Resour. Res.*, 47(9), doi:10.1029/2010WR009827.

Clark, M. P., J. Hendrikx, A. G. Slater, D. Kavetski, B. Anderson, N. J. Cullen, T. Kerr, E. Örn Hreinnsson, and R. A. Woods (2011b), Representing spatial variability of snow water equivalent in hydrologic and land-surface models: A review, *Water Resour. Res.*, 47(7).

Clark, M. P. et al. (2015a), A unified approach for process-based hydrologic modeling: 2. Model implementation and case studies, *Water Resour. Res.*, 51, 2515–2542, doi:10.1002/2015WR017198.A.

Clark, M. P. et al. (2015b), A unified approach for process-based hydrologic modeling: 1. Modeling concept, *Water Resour. Res.*, 51(4), 1–17, doi:10.1002/2015WR017200.A.

Clark, M. P. et al. (2015c), *The structure for unifying multiple modeling alternatives Technical Description NCAR Technical Notes*, Boulder.

Cosgrove, B. a. (2003), Real-time and retrospective forcing in the North American Land Data Assimilation System (NLDAS) project, *J. Geophys. Res.*, 108(D22), 8842, doi:10.1029/2002JD003118.

Dai, A. (2008), Temperature and pressure dependence of the rain-snow phase transition over land and ocean, *Geophys. Res. Lett.*, 35(12), 1–7, doi:10.1029/2008GL033295.

Dilley, A. C., and D. M. O'Brien (1998), Estimating downward clear sky long-wave irradiance at the surface from screen temperature and precipitable water, *Q. J. R.*, 124, 1391–1401.

Egli, L., T. Jonas, and R. Meister (2009), Comparison of different automatic methods for estimating snow water equivalent, *Cold Reg. Sci. Technol.*, 57(2-3), 107–115, doi:10.1016/j.coldregions.2009.02.008.

Eiriksson, D., M. Whitson, C. H. Luce, H. P. Marshall, J. Bradford, S. G. Benner, T. Black, H. Hetrick, and J. P. Mcnamara (2013), An evaluation of the hydrologic relevance of lateral flow in snow at hillslope and catchment scales, *Hydrol. Process.*, 654(January), 640–654, doi:10.1002/hyp.9666.

Elsner, M. M., L. Cuo, N. Voisin, J. S. Deems, A. F. Hamlet, J. A. Vano, K. E. B. Mickelson, S.-Y. Lee, and D. P. Lettenmaier (2010), Implications of 21st century climate change for the

hydrology of Washington State, *Clim. Change*, 102(1-2), 225–260, doi:10.1007/s10584-010-9855-0.

Essery, R., N. Rutter, J. Pomeroy, R. Baxter, M. Stahli, D. Gustafsson, A. Barr, P. Bartlett, and K. Elder (2009), SNOWMIP2: An evaluation of forest snow process simulations, *Bull. Am. Meteorol. Soc.*, 90(8), 1120–1135.

Essery, R., S. Morin, Y. Lejeune, and C. B. Ménard (2013), A comparison of 1701 snow models using observations from an alpine site, *Adv. Water Resour.*, 55, 131–148, doi:10.1016/j.advwatres.2012.07.013.

Feiccabrino, J., W. Graff, A. Lundberg, N. Sandström, and D. Gustafsson (2015), Meteorological Knowledge Useful for the Improvement of Snow Rain Separation in Surface Based Models, *Hydrology*, 2(4), 266–288, doi:10.3390/hydrology2040266.

Flerchinger, G. N., W. Xaio, D. Marks, T. J. Sauer, and Q. Yu (2009), Comparison of algorithms for incoming atmospheric long-wave radiation, *Water Resour. Res.*, 45(3), 1–13, doi:10.1029/2008WR007394.

Garvelmann, J., S. Pohl, and M. Weiler (2014), Variability of observed energy fluxes during rain-on-snow and clear sky snowmelt in a mid-latitude mountain environment, *J. Hydrometeorol.*, 140211144106009, doi:10.1175/JHM-D-13-0187.1.

Garvelmann, J., S. Pohl, and M. Weiler (2015), Spatio-temporal controls of snowmelt and runoff generation during rain-on-snow events in a mid-latitude mountain catchment, *Hydrol. Process.*, 29, 3649–3664, doi:10.1002/hyp.10460.

Gerdel, R. (1948), Physical changes in snow cover leading to runoff, especially to floods, IAHS-AIHS Publ.

Gong, Y. W., Z. Y. Shen, Q. Hong, R. M. Liu, and Q. Liao (2011), Parameter uncertainty analysis in watershed total phosphorus modeling using the GLUE methodology, *Agr. Ecosyst. Env.*, 142, 246–255.

Gupta, H. V., H. Kling, K. K. Yilmaz, and G. F. Martinez (2009), Decomposition of the mean squared error and NSE performance criteria: Implications for improving hydrological modelling, *J. Hydrol.*, 377(1-2), 80–91, doi:10.1016/j.jhydrol.2009.08.003.

Gupta, H. V., M. P. Clark, J. a. Vrugt, G. Abramowitz, and M. Ye (2012), Towards a comprehensive assessment of model structural adequacy, *Water Resour. Res.*, 48(8), 1–16, doi:10.1029/2011WR011044.

Harder, P., and J. Pomeroy (2013), Estimating precipitation phase using a psychrometric energy balance method, *Hydrol. Process.*, 27(13), 1901–1914, doi:10.1002/hyp.9799.

Harr, R. (1981), Some characteristics and consequences of snowmelt during rainfall in western Oregon, *J. Hydrol.*, 53, 277–304.

Harr, R., and B. Coffin (1992), Influence of timber harvest on rain-on-snow runoff: a mechanism for cumulative watershed effects, *Interdiscip. approaches Hydrol. Hydrogeol.*, 455–469.

Hedstrom, N. R., and J. W. Pomeroy (1998), Measurements and modelling of snow interception in the boreal forest, , 1625(March), 1611–1625.

Heeswijk, M. van, J. Kimball, and Marks (1996), Simulation of water available for runoff in clearcut forest openings during rain-on-snow events in the western Cascade Range of Oregon and Washington.

Hinkelman, L. M., K. E. Lapo, N. C. Cristea, and J. D. Lundquist (2015), Using CERES SYN Surface Irradiance Data as Forcing for Snowmelt Simulation in Complex Terrain, *J. Hydrometeorol.*, 150702111346007, doi:10.1175/JHM-D-14-0179.1.

Hungerford, R., R. R. Nemani, S. W. Running, and J. C. Coughlan (1989), MTCLIM: a mountain microclimate simulation model.

Ikeda, K. et al. (2010), Simulation of seasonal snowfall over Colorado, *Atmos. Res.*, 97(4), 462–477, doi:10.1016/j.atmosres.2010.04.010.

Jin, J., and N. L. Miller (2007), Analysis of the Impact of Snow on Daily Weather Variability in Mountainous Regions Using MM5, *J. Hydrometeorol.*, 8(2), 245–258, doi:10.1175/JHM565.1.

Jones, J. a., and R. M. Perkins (2010), Extreme flood sensitivity to snow and forest harvest, western Cascades, Oregon, United States, *Water Resour. Res.*, 46(12), doi:10.1029/2009WR008632.

Kalnay, E. et al. (1996), The NCEP/NCAR 40-Year Reanalysis Project, *Bull. Am. Meteorol. Soc.*, 77(3), 437–471, doi:10.1175/1520-0477(1996)077<0437:TNYRP>2.0.CO;2.

Kattelman, R. (1997), Rapid changes in snow cover at low elevations in the Sierra Nevada, California, USA, edited by J. E. Walsh, *Ann. Glaciol.*, 25, 367–370.

Kavetski, D., and M. P. Clark (2011), Numerical troubles in conceptual hydrology: Approximations, absurdities and impact on hypothesis testing, *Hydrol. Process.*, 25(4), 661–670, doi:10.1002/hyp.7899.

Khain, A., M. Ovtchinnikov, M. Pinsky, A. Pokrovsky, and H. Krugliak (2000), Notes on the state-of-the-art numerical modeling of cloud microphysics, *Atmos. Res.*, 55(3-4), 159–224, doi:10.1016/S0169-8095(00)00064-8.

Kinar, N. J., and J. W. Pomeroy (2015), SAS2: the system for acoustic sensing of snow, *Hydrol. Process.*, doi:10.1002/hyp.10535.

Kirchner, J. W. (2006), Getting the right answers for the right reasons: Linking measurements, analyses, and models to advance the science of hydrology, *Water Resour. Res.*, 42(3), doi:10.1029/2005WR004362.

Kling, H., M. Fuchs, and M. Paulin (2012), Runoff conditions in the upper Danube basin under an ensemble of climate change scenarios, *J. Hydrol.*, 424-425, 264–277, doi:10.1016/j.jhydrol.2012.01.011.

Klos, P., T. Link, and J. Abatzoglou (2014), Extent of the rain-snow transition zone in the western US under historic and projected climate, *Geophys. Res.*, 4560–4568, doi:10.1002/2014GL060500.Received.

Landry, C., K. Buck, M. Raleigh, and M. Clark (2014), monitoring at Senator Beck Basin, San Juan Mountains, Colorado: A new integrative data source to develop and evaluate models of snow and hydrologic processes, *Water Resour.*, 1773–1788, doi:10.1002/2013WR013711.Received.

Lapo, K., L. Hinkelman, M. S. Raleigh, and J. D. Lundquist (2015), Impact of errors in the downwelling irradiances on simulations of snow water equivalent, snow surface temperature, and the snow energy balance, *Water Resour.*, 1649–1670, doi:10.1002/2014WR016259.Received.

Letcher, T. W., and J. R. Minder (2015), Characterization of the simulated regional snow albedo feedback using a regional climate model over complex terrain, *J. Clim.*, 28(19), 7576–7595, doi:10.1175/JCLI-D-15-0166.1.

Liang, X., D. P. Lettenmaier, E. F. Wood, and S. J. Burges (1994), A simple hydrologically based model of land surface water and energy fluxes for general circulation models, *J. Geophys. Res.*, 99(D7), 14415, doi:10.1029/94JD00483.

Liston, G. E., and Elder (2006), A Meteorological Distribution System for High-Resolution Terrestrial Modeling (MicroMet), *J. Hydrometeorol.*, 7, 217–234.

Livneh, B., Y. Xia, K. E. Mitchell, M. B. Ek, and D. P. Lettenmaier (2010), Noah LSM Snow Model Diagnostics and Enhancements, *J. Hydrometeorol.*, 11(3), 721–738, doi:10.1175/2009JHM1174.1.

Lundquist, J. D., and D. R. Cayan (2007), Surface temperature patterns in complex terrain: Daily variations and long-term change in the central Sierra Nevada, California, *J. Geophys. Res.*, 112(D11), 1–15, doi:10.1029/2006JD007561.

Lundquist, J. D., P. J. Neiman, B. Martner, A. B. White, D. J. Gattas, and F. M. Ralph (2008a), Rain versus Snow in the Sierra Nevada, California: Comparing Doppler Profiling Radar and Surface Observations of Melting Level, *J. Hydrometeorol.*, 9(2), 194–211, doi:10.1175/2007JHM853.1.

Lundquist, J. D., P. J. Neiman, B. Martner, A. B. White, D. J. Gattas, and F. M. Ralph (2008b), Rain versus Snow in the Sierra Nevada, California: Comparing Doppler Profiling Radar and Surface Observations of Melting Level, *J. Hydrometeorol.*, 9(2), 194–211, doi:10.1175/2007JHM853.1.

Lundquist, J. D., J. R. Minder, P. J. Neiman, and E. Sukovich (2010), Relationships between Barrier Jet Heights, Orographic Precipitation Gradients, and Streamflow in the Northern Sierra Nevada, *J. Hydrometeorol.*, 11(5), 1141–1156, doi:10.1175/2010JHM1264.1.

Lundquist, J. D., N. E. Wayand, A. Massmann, M. P. Clark, F. Lott, and N. C. Cristea (2015a), Diagnosis of insidious data disasters, *Water Resour. Res.*, 51(5), doi:10.1002/2014WR016585.

Lundquist, J. D., M. Hughes, B. Henn, E. D. Gutmann, B. Livneh, J. Dozier, and P. Neiman (2015b), High-elevation precipitation patterns: using snow measurements to assess daily gridded datasets across the Sierra Nevada, California, *J. Hydrometeorol.*, 150508072628008, doi:10.1175/JHM-D-15-0019.1.

Magnusson, J., and N. Wever (2015), Evaluating snow models with varying process representations for hydrological applications, *Water Resour.*, 1–17.

Marks, D., J. Kimball, and D. Tingey (1998), The sensitivity of snowmelt processes to climate conditions and forest cover during rain-on-snow: a case study of the 1996 Pacific Northwest flood, *Hydrol. Process.*, 1587(March).

Marks, D., T. Link, A. Winstral, and D. Garen (2001), Simulating snowmelt processes during rain-on-snow over a semi-arid mountain basin, edited by K. Hutter, *Ann. Glaciol.*, 32(1), 195–202, doi:10.3189/172756401781819751.

Marks, D., A. Winstral, M. Reba, J. Pomeroy, and M. Kumar (2013), An evaluation of methods for determining during-storm precipitation phase and the rain/snow transition elevation at the surface in a mountain basin, *Adv. Water Resour.*, 55, 98–110.

Marsh, P., and M.-K. Woo (1984), Wetting Front Advance and Freezing of Meltwater Within a Snow Cover 1. Observations in the Canadian Arctic, *Water Resour. Res.*, 20(12), 1853–1864.

Marty, C., R. Philipona, C. Fröhlich, and A. Ohmura (2002), Altitude dependence of surface radiation fluxes and cloud forcing in the alps: results from the alpine surface radiation budget network, *Theor. Appl. Climatol.*, 72(3), 137–155.

Mass, C. F. et al. (2003), Regional environmental prediction over the pacific northwest, *Bull. Am. Meteorol. Soc.*, 84(10), 1353–1366+1328, doi:10.1175/BAMS-84-10-1353.

Mauger, G. S., J. H. Casola, H. a. Morgan, R. L. Strauch, B. Kones, B. Curry, T. M. Busch Isaksen, L. Whitely Binder, and A. K. Snover (2015), State of Knowledge: Climate Change in Puget Sound.

Maurer, E. P., and C. Mass (2006), Using Radar Data to Partition Precipitation into Rain and Snow in a Hydrologic Model, *J. Hydrol. Eng.*, 11(3), 214–221, doi:10.1061/(ASCE)1084-0699(2006)11:3(214).

Maurer, E. P., A. W. Wood, J. C. Adam, D. P. Lettenmaier, and B. Nijssen (2002), A Long-Term Hydrologically Based Dataset of Land Surface Fluxes and States for the Conterminous United States*, *J. Clim.*, 15(1993), 3237–3251.

Mazurkiewicz, A. B., D. G. Callery, and J. J. McDonnell (2008), Assessing the controls of the snow energy balance and water available for runoff in a rain-on-snow environment, *J. Hydrol.*, 354(1-4), 1–14, doi:10.1016/j.jhydrol.2007.12.027.

McCabe, G. J., M. P. Clark, and L. E. Hay (2007), Rain-on-Snow Events in the Western United States, *Bull. Am. Meteorol. Soc.*, 88(3), 319–328, doi:10.1175/BAMS-88-3-319.

Meek, D. W., and J. L. Hatfield (1994), Data quality checking for single station meteorological databases I, *Agric. For. Meteorol.*, 1923(93).

Minder, J. R., Durran, D. R., Roe, G. H. and Anders, A. M. (2008), The climatology of small-scale orographic precipitation over the Olympic Mountains: Patterns and processes. *Q.J.R. Meteorol. Soc.*, 134: 817–839. doi: 10.1002/qj.258

Minder, J. R. (2010), The Sensitivity of Mountain Snowpack Accumulation to Climate Warming, *J. Clim.*, 23(10), 2634–2650, doi:10.1175/2009JCLI3263.1.

Minder, J. R., and D. E. Kingsmill (2013), Mesoscale Variations of the Atmospheric Snow Line over the Northern Sierra Nevada: Multiyear Statistics, Case Study, and Mechanisms, *J. Atmos. Sci.*, 70(3), 916–938, doi:10.1175/JAS-D-12-0194.1.

Minder, J. R., P. W. Mote, and J. D. Lundquist (2010), Surface temperature lapse rates over complex terrain: Lessons from the Cascade Mountains, *J. Geophys. Res.*, 115(D14), doi:10.1029/2009JD013493.

Minder, J. R., D. R. Durran, and G. H. Roe (2011), Mesoscale Controls on the Mountainside Snow Line, *J. Atmos. Sci.*, 68(9), 2107–2127, doi:10.1175/JAS-D-10-05006.1.

Mitchell, K. E. (2004), The multi-institution North American Land Data Assimilation System (NLDAS): Utilizing multiple GCIP products and partners in a continental distributed hydrological modeling system, *J. Geophys. Res.*, 109(D7).

Mizukami, N., V. Koren, M. Smith, D. Kingsmill, Z. Zhang, B. Cosgrove, and Z. Cui (2013), The Impact of Precipitation Type Discrimination on Hydrologic Simulation: Rain–Snow Partitioning Derived from HMT-West Radar-Detected Brightband Height versus Surface Temperature Data, *J. Hydrometeorol.*, 14(4), 1139–1158, doi:10.1175/JHM-D-12-035.1.

Mizukami, N., M. P. Clark, A. G. Slater, L. D. Brekke, M. M. Elsner, J. R. Arnold, and S. Gangopadhyay (2014), Hydrologic Implications of Different Large-Scale Meteorological Model Forcing Datasets in Mountainous Regions, *J. Hydrometeorol.*, 15(1), 474–488, doi:10.1175/JHM-D-13-036.1.

- Morin, S., Y. Lejeune, B. Lesaffre, J.-M. Panel, D. Poncet, P. David, and M. Sudul (2012), An 18-yr long (1993–2011) snow and meteorological dataset from a mid-altitude mountain site (Col de Porte, France, 1325 m alt.) for driving and evaluating snowpack models, *Earth Syst. Sci. Data*, 4(1), 13–21, doi:10.5194/essd-4-13-2012.
- Mote, P. W., A. F. Hamlet, M. P. Clark, and D. P. Lettenmaier (2005), Declining Mountain Snowpack in Western North America, *Bull. Am. Meteorol. Soc.*, 86(1), 39–49, doi:10.1175/BAMS-86-1-39.
- Nearing, G. S., and H. V. Gupta (2014), The quantity and quality of information in hydrologic models, *Water Resour. Res.*, 51, 524–538, doi:10.1002/2013WR014956.Received.
- Neiman, P. J., E. M. Sukovich, F. M. Ralph, and M. Hughes (2010), A Seven-Year Wind Profiler–Based Climatology of the Windward Barrier Jet along California’s Northern Sierra Nevada, *Mon. Weather Rev.*, 138(4), 1206–1233, doi:10.1175/2009MWR3170.1.
- Newell, E. R., N. E. Newell, Y. Zhu, and C. Scott (1992), Tropospheric Rivers? - A Pilot Study, *Geophys. Res. Lett.*, 19(24), 2401–2404, doi:doi:10.1029/92GL02916.
- Newman, A. J., M. P. Clark, J. Craig, B. Nijssen, A. Wood, E. Gutmann, N. Mizukami, L. Brekke, and J. R. Arnold (2015), Gridded Ensemble Precipitation and Temperature Estimates for the Contiguous United States, *J. Hydrometeorol.*, 16(6), 2481–2500, doi:10.1175/JHM-D-15-0026.1.
- Nolin, A., and C. Daly (2006), Mapping “at risk” snow in the Pacific Northwest, *J. Hydrometeorol.*, 1164–1171.
- Oleson, K., D. Lawrence, and B. Gordon (2010), Technical description of version 4.0 of the Community Land Model (CLM), Boulder.
- Pahaut (1976), *La métamorphose des cristaux de neige (Snow crystal metamorphosis)*.
- Parajka, J., P. Haas, and R. Kirnbauer (2011), Potential of time • lapse photography of snow for hydrological purposes at the small catchment scale, *Hydrol.*, doi:10.1002/hyp.
- Pfister, R., and M. Schneebeli (1999), Snow accumulation on boards of different sizes and shapes, *Hydrol. Process.*, 2355(May 1998), 2345–2355.
- Prata, A. J. (1996), A new long-wave formula for estimating downward clear-sky radiation at the surface, *Q. J. R. Meteorol. Soc.*, 122(533), 1127–1151, doi:10.1002/qj.49712253306.
- Prater, Y. (1981), *Snoqualmie Pass : From Indian trail to interstate*, Mountaineers, Seattle.
- Raleigh, M. S., J. D. Lundquist, and M. P. Clark (2014), Exploring the impact of forcing error characteristics on physically based snow simulations within a global sensitivity analysis framework, *Hydrol. Earth Syst. Sci. Discuss.*, 11(12), 13745–13795, doi:10.5194/hessd-11-13745-2014.

Raleigh, M. S., B. Livneh, K. Lapo, and J. D. Lundquist (2016), How Does Availability of Meteorological Forcing Data Impact Physically Based Snowpack Simulations?*, *J. Hydrometeorol.*, 17(1), 99–120, doi:10.1175/JHM-D-14-0235.1.

Ralph, F. M. et al. (2005), Improving Short-Term (0–48 h) Cool-Season Quantitative Precipitation Forecasting: Recommendations from a USWRP Workshop, *Bull. Am. Meteorol. Soc.*, 86(11), 1619–1632, doi:10.1175/BAMS-86-11-1619.

Rasmussen, R. et al. (2012), How Well Are We Measuring Snow: The NOAA/FAA/NCAR Winter Precipitation Test Bed, *Bull. Am. Meteorol. Soc.*, 93(6), 811–829, doi:10.1175/BAMS-D-11-00052.1.

Reba, M. L., T. E. Link, D. Marks, and J. Pomeroy (2009), An assessment of corrections for eddy covariance measured turbulent fluxes over snow in mountain environments, *Water Resour. Res.*, 45(April), 1–15, doi:10.1029/2008WR007045.

Reba, M. L., D. Marks, M. Seyfried, A. Winstral, M. Kumar, and G. Flerchinger (2011), A long-term data set for hydrologic modeling in a snow-dominated mountain catchment, *Water Resour. Res.*, 47(7), W07702, doi:10.1029/2010WR010030.

Rice, R., R. C. Bales, T. H. Painter, and J. Dozier (2011), Snow water equivalent along elevation gradients in the Merced and Tuolumne River basins of the Sierra Nevada, *Water Resour. Res.*, 47(8), 1–11, doi:10.1029/2010WR009278.

Riesboll, H., L. Hunsaker, and D. Mahoney (1965), Role of Snowmelt and Snowpack storage in production of Runoff on Feather River Basin during December 1955 Flood, in *Proceedings of the 33rd Annual Western Snow Conference*, Colorado Springs, Colorado.

Roebber, P. J., S. L. Bruening, D. M. Schultz, and J. V. Cortinas (2003), Improving snowfall forecasting by diagnosing snow density, *Weather Forecast.*, 18, 264–287.

Roos, M. (2007), A Half Century of Watching California Floods, *Calif. Dep. Water Resour. News*, Summer, 16–22.

Rössler, O., P. Froidevaux, U. Börsch, R. Rickli, O. Martius, and R. Weingartner (2014), Retrospective analysis of a nonforecasted rain-on-snow flood in the Alps – a matter of model limitations or unpredictable nature?, *Hydrol. Earth Syst. Sci.*, 18(6), 2265–2285, doi:10.5194/hess-18-2265-2014.

Schmid, L., A. Heilig, C. Mitterer, J. Schweizer, H. Maurer, R. Okorn, and O. Eisen (2014), Continuous snowpack monitoring using upward-looking ground-penetrating radar technology, *J. Glaciol.*, 60(221), 509–525, doi:10.3189/2014JoG13J084.

Serreze, M. C., M. P. Clark, R. L. Armstrong, D. a. McGinnis, and R. S. Pulwarty (1999), Characteristics of the western United States snowpack from snowpack telemetry (SNOTEL) data, *Water Resour. Res.*, 35(7), 2145–2160, doi:10.1029/1999WR900090.

Sevruk, B. (1983), Correction of Measured Precipitation in the Alps Using the Water Equivalent of New Snow, *Weather*, 14(2), 49–58.

Sharp, J., and C. F. Mass (2004), Columbia gorge gap winds: Their climatological influence and synoptic evolution, *Weather Forecast.*, 19(6), 970–992, doi:10.1175/826.1.

Sims, E. M., and G. Liu (2015), A Parameterization of the Probability of Snow–Rain Transition, *J. Hydrometeorol.*, 16(4), 1466–1477, doi:10.1175/JHM-D-14-0211.1.

Singh, P., G. Spitzbart, H. Hubl, and H. Weinmeister (1997), Hydrological response of snowpack under rain-on-snow events: a field study, *J. Hydrol.*, 202, 1–20.

Skamarock, W., and J. Klemp (2008), A time-split nonhydrostatic atmospheric model for weather research and forecasting applications, *J. Comput. Phys.*, 227(7), 3465–3485, doi:10.1016/j.jcp.2007.01.037.

Steenburgh, W., C. F. Mass, and S. A. Ferguson (1997), The influence of terrain-induced circulations on wintertime temperature and snow level in the Washington Cascades, *Weather Forecast.*, 12, 208–227.

Stimberis, J., and C. Rubin (2011a), Glide avalanche response to an extreme rain-on-snow event, Snoqualmie Pass, Washington, USA, *J. Glaciol.*, 57(203), 468–474.

Stimberis, J., and C. M. Rubin (2011b), Glide avalanche response to an extreme rain-on-snow event, *J. Glaciol.*, 57(203), 468–474.

Siler, N. and D. Durran (in review), What causes weak orographic rain shadows?—Insights from case studies in the Cascades and idealized simulations, *J. Atmos. Sciences*.

Storck, P. (2000), Trees, snow and flooding: An investigation of forest canopy effects on snow accumulation and melt at the plot and watershed scales in the Pacific Northwest, University of Washington.

Storck, P., and L. Bowling (1998), Application of a GIS-based distributed hydrology model for prediction of forest harvest effects on peak stream flow in the Pacific Northwest, *Hydrol. Process.*, 12, 889–904.

Sturm, M., J. Holmgren, and G. Liston (1995), A seasonal snow cover classification system for local to global applications, *J. Clim.*, doi:http://dx.doi.org/10.1175/1520-0442(1995)008<1261:ASSCCS>2.0.CO;2.

Sturm, M., B. Taras, G. E. Liston, C. Derksen, T. Jonas, and J. Lea (2010), Estimating Snow Water Equivalent Using Snow Depth Data and Climate Classes, *J. Hydrometeorol.*, 11(6), 1380–1394, doi:10.1175/2010JHM1202.1.

Sui, J., and G. Koehler (2001), Rain-on-snow induced flood events in Southern Germany, *J. Hydrol.*, 252.

Thomas, C. K., B. E. Law, J. Irvine, J. G. Martin, J. C. Pettijohn, and K. J. Davis (2009), Seasonal hydrology explains interannual and seasonal variation in carbon and water exchange in a semiarid mature ponderosa pine forest in central Oregon, *J. Geophys. Res.*, 114(G4), G04006, doi:10.1029/2009JG001010.

Thompson, G., R. M. Rasmussen, and K. Manning (2004), Explicit Forecasts of Winter Precipitation Using an Improved Bulk Microphysics Scheme. Part I: Description and Sensitivity Analysis, *Mon. Weather Rev.*, 132(2), 519–542, doi:10.1175/1520-0493(2004)132<0519:EFOWPU>2.0.CO;2.

Thornton, P., and S. Running (1999), An improved algorithm for estimating incident daily solar radiation from measurements of temperature, humidity, and precipitation, *Agric. For. Meteorol.*, 93.

USACE (1956), Snow hydrology summary report of the snow investigations., North Pacific Division Portland.

Vano, J. (2015), Seasonal hydrologic responses to climate change in the Pacific Northwest, *Water Resour.*, 51, 1959–1976, doi:10.1002/2014WR015909.Received.

Varhola, A., N. C. Coops, M. Weiler, and R. D. Moore (2010), Forest canopy effects on snow accumulation and ablation: An integrative review of empirical results, *J. Hydrol.*, 392(3-4), 219–233, doi:10.1016/j.jhydrol.2010.08.009.

Vionnet, V., S. Bélair, C. Girard, and A. Plante (2015), Wintertime Subkilometer Numerical Forecasts of Near-Surface Variables in the Canadian Rocky Mountains, *Mon. Weather Rev.*, 143(2), 666–686, doi:10.1175/MWR-D-14-00128.1.

Waichler, S. R., and M. S. Wigmosta (2003), Development of Hourly Meteorological Values From Daily Data and Significance to Hydrological Modeling at H. J. Andrews Experimental Forest, *J. Hydrometeorol.*, 4(2), 251–263, doi:10.1175/1525-7541(2003)4<251:DOHMFV>2.0.CO;2.

Wayand, N. E., A. F. Hamlet, M. Hughes, S. I. Feld, and J. D. Lundquist (2013), Intercomparison of Meteorological Forcing Data from Empirical and Mesoscale Model Sources in the N.F. American River Basin in northern Sierra Nevada, California, *J. Hydrometeorol.*, 14(3), 677–699, doi:10.1175/JHM-D-12-0102.1.

Wayand, N. E., A. Massmann, C. Butler, E. Keenan, and J. D. Lundquist (2015a), A Meteorological and Snow observational data set from Snoqualmie Pass (921 m), Washington Cascades, U.S., *Water Resour. Res.*, doi:10.1002/2015WR017773.

Wayand, N. E., J. D. Lundquist, and M. P. Clark (2015b), Modeling the influence of hypsometry, vegetation, and storm energy on snowmelt contributions to basins during rain-on-snow floods, *Water Resour. Res.*, 51, 8551–8569, doi:10.1002/2014WR016576.

Wayand, N. E., M. P. Clark, and J. D. Lundquist (*in review*), Diagnosing Snow Accumulation Errors in a Rain-Snow Transitional Environment with Snow Board Observations, *Hydrological Processes*.

Westrick, K. (2001), An evaluation of a high-resolution hydrometeorological modeling system for prediction of a cool-season flood event in a coastal mountainous watershed, *J. Hydrometeorol.*, 161, 161–180.

Westrick, K., and P. Storck (2002), Description and evaluation of a hydrometeorological forecast system for mountainous watersheds, *Weather Forecast.*, 250–262.

Wever, N., L. Schmid, a. Heilig, O. Eisen, C. Fierz, and M. Lehning (2015), Verification of the multi-layer SNOWPACK model with different water transport schemes, *Cryosph. Discuss.*, 9(2), 2655–2707, doi:10.5194/tcd-9-2655-2015.

White, A. B., D. J. Gattas, E. Strem, F. M. Ralph, and P. J. Neiman (2002), An automated brightband height detection algorithm for use with Doppler radar spectral moments, *J. Atmos. Ocean. Technol.*, 19(5), 687–697.

White, A. B., D. J. Gattas, A. F. Henkel, P. J. Neiman, F. M. Ralph, and S. I. Gutman (2010), Developing a Performance Measure for Snow-Level Forecasts, *J. Hydrometeorol.*, 11(3), 739–753, doi:10.1175/2009JHM1181.1.

Wigmosta, M. S., L. W. Vail, and D. P. Lettenmaier (1994), A distributed hydrology-vegetation model for complex terrain, *Water Resour. Res.*, 30(6), 1665–1679, doi:10.1029/94WR00436.

Williams, M. W., T. a. Erickson, and J. L. Petzelka (2010), Visualizing meltwater flow through snow at the centimetre-to-metre scale using a snow guillotine, *Hydrol. Process.*, 24(15), 2098–2110, doi:10.1002/hyp.7630.

Wood, A. W., T. Hopson, A. Newman, L. Brekke, J. Arnold, and M. Clark (2015), Quantifying Streamflow Forecast Skill Elasticity To Initial Condition and Climate Prediction Skill, *J. Hydrometeorol.*, (OCTOBER), 151030135123004, doi:10.1175/JHM-D-14-0213.1.

Yang, D., and B. Goodison (1998), Accuracy of NWS 8" standard nonrecording precipitation gauge: Results and application of WMO intercomparison, *Atmos.*, 54–68, doi:10.1175/1520-0426(1998)015<0054:AONSNP>2.0.CO;2.

Curriculum Vitae

NICHOLAS E. WAYAND

University of Washington, Box 352700, Seattle, WA 98195-2700 USA
nicway@u.washington.edu | +1 360 265 7720 | Skype: nicwayand
Website: <http://students.washington.edu/nicway> | Github: NicWayand

ACADEMIC SUMMARY

University of Washington, Dept. of Civil & Environmental Engineering

Candidate for Doctor of Philosophy (Degree anticipated March 2016)

Dissertation Title: *Observation, Simulation, and Evaluation of Snow Dynamics in the Transitional Snow Zone*

Dissertation Committee: Jessica D. Lundquist, Martyn Clark, Bart Nijssen, Chris Bretherton

University of Washington, Dept. of Civil & Environmental Engineering

Master of Science in Civil Engineering, with an emphasis on Hydrology (June 2012)

Thesis Title: *Intercomparison of Meteorological Forcing Data from Empirical and Mesoscale Model Sources in the N.F. American River Basin in Northern California*

University of Washington, Dept. of Atmospheric Sciences

Bachelor of Science in Atmospheric Sciences, Minor in Applied Mathematics (March 2010)

PROFESSIONAL MEMBERSHIPS

American Geophysical Union member, 2010 – present

UW Panel on Climate Change member, 2010 – present

EMPLOYMENT HISTORY

Graduate Student Research Assistant, 2010 to present

Civil and Environmental Engineering Dept., University of Washington

Graduate Instructor, CEE 573 Snow Hydrology, Winter Quarter 2015

Civil and Environmental Engineering Dept., University of Washington

NCAR Graduate Visitor, September 2012 – June 2013

National Center for Atmospheric Research, Boulder, CO

Valle Scholar, September 2011– June 2012

Universitetet i Bergen, Bergen, Norway

Undergraduate Research Assistant, 2007 – 2009
Atmospheric Science Dept., University of Washington

PUBLICATIONS

Wayand, N. E., A. Massmann, C. Butler, E. Keenan, and J. D. Lundquist, 2015: A Meteorological and Snow observational data set from Snoqualmie Pass (921 m), Washington Cascades, U.S., *Water Resour. Res.*, doi:10.1002/2015WR017773.

Wayand, N. E., J. D. Lundquist, and M. P. Clark, 2015: Modeling the influence of hypsometry, vegetation, and storm energy on snowmelt contributions to basins during rain-on-snow floods, *Water Resour. Res.*, 51, 8551–8569, doi:10.1002/2014WR016576.

Lundquist, J. D., **N. E. Wayand**, A. Massmann, M. P. Clark, F. Lott, and N. C. Cristea, 2015: Diagnosis of insidious data disasters, *Water Resour. Res.*, 51, 3815–3827, doi:10.1002/2014WR016585.

Wayand, N. E., A. F. Hamlet, M. Hughes, S. I. Feld, and J. D. Lundquist, 2013: Intercomparison of Meteorological Forcing Data from Empirical and Mesoscale Model Sources in the North Fork American River Basin in Northern Sierra Nevada, California, *J. Hydrometeor.*, 14, 677–699. doi: <http://dx.doi.org/10.1175/JHM-D-12-0102.1>

Wayand, N. E., and Lundquist J., 2013: Observing the Elusive Intermittent Snow using Traffic Camera Images. 81st Annual Western Snow Conference.
<http://www.westernsnowconference.org/sites/westernsnowconference.org/PDFs/2013Wayand.pdf>

Wayand, N. E., Lundquist J., Hughes M., and Hamlet A. Supplementing Sparse Observations of Temperature and Precipitation with a High Resolution Atmospheric Model. Western Snow Conference, South Lake Tahoe, April 18-21st, 2011. In: Freeman, Gary, *Proceedings of the 79th Annual Western Snow Conference*.
<http://www.westernsnowconference.org/sites/westernsnowconference.org/PDFs/2011Wayand.pdf>

Forsyth, J., Lundquist J., and **Wayand N. E.** An Experimental and Modeling Investigation of the Impact of Silvicultural Manipulation on Snow Hydrology in the Cedar River Watershed, WA. Western Snow Conference, Logan, UT, April, 2010. In: Freeman, Gary, *Proceedings of the 78th Annual Western Snow Conference*.
<http://www.westernsnowconference.org/sites/westernsnowconference.org/PDFs/2010Forsyth.pdf>

CONFERENCE PRESENTATIONS

Wayand, N. E., Lundquist J., and Clark, M. Is snowmelt important for runoff during rain-on-snow floods over the Western U.S. Mountains? American Geophysical Union Fall Meeting, San Francisco, California, December 15-18th, 2014.

Wayand, N E., Massmann A., Clark, M, and Lundquist J. Constraining snow model choices in a transitional snow environment with intensive observations. American Geophysical Union Fall Meeting, San Francisco, California, December 15-18th, 2014.

Wayand, N. E. and Lundquist J. Constraining snow model choices in a transitional and intermittent snow environment with intensive observations. The 71st Annual Eastern Snow Conference. Boone, North Carolina, June, 2014.

Wayand, N E., Lundquist J., and Clark, M. Is snowmelt important for runoff during rain-on-snow floods over the Western U.S. Mountains? European Geophysical Union conference Fall Meeting, Vienna, Austria, April 2014.

Wayand, N. E., Lundquist, J., Hamlet, A. A Distributed Hydrological model Forced by DIMP2 Data and the WRF Mesoscale model. American Geophysical Union Fall Meeting, San Francisco, California, December 5-9th, 2010.

Wayand, N. E., Lundquist, J., Hamlet, A. The Applicability of Regional Climate Models for Distributed Hydroclimate Simulations of Snowpack. Graduate Climate Conference, Pack Forest Conference Center, Eatonville, Washington, October 26-28th, 2010.

Wayand, N. E., Minder, J., Durran, D., and Roe, G. The effects of a Warming Climate on snowpack accumulation in the Northern Cascades. Pacific Northwest Weather Workshop, NOAA Western Regional Campus, Seattle, March 20-21st, 2009.

FELLOWSHIPS AND AWARDS

UW Panel on Climate Change Certificate, 2016

Distributed Research Infrastructure for Hydro-Meteorology Certificate, 2014

NASA Earth and Space Science Fellowship, 2013 - 2016

To support three years of PhD research on remote sensing of the Cryosphere.

National Science Foundation Grant, 2013 - 2015

To support three years of PhD research related to study of the Transitional Snow Zone.

Valle Scholarship, 2010 – 2011

To support research and education placement at the Universitetet i Bergen, Norway.

Graduate Student Panel on Climate Change Fellow, 2009 – 2010

Funded research on the suitability of meteorological forcing for hydrological models.

Atmospheric Sciences Richard J. and Joan M. Reed Endowed Scholarship, 2009

To support undergraduate study and research in atmospheric sciences.

MEDIA AND OUTREACH

1. High school module on Rain-on-snow flooding - Inglemoor High School.
<http://www.uwpsc.washington.edu/outreach/tertiary.jsp?entity=RSF&action=GetEntity&title=Rain%20on%20Snow%20Flooding%20Module> March 2015.
2. AGU Press release – *Improving forecasts for rain-on-snow flooding*.
<http://fallmeeting.agu.org/2014/press-item/improving-forecasts-for-rain-on-snow-flooding/> December 2014.

3. Seattle Science Fellow – K-12 hands on activity: *How much water is contained in snow?*
<http://www.pacificsciencecenter.org/Articles/meet-nic-wayand> 2010 - 2013.

SKILLS AND COMPETENCIES

Computer Languages

Proficient: Matlab, ArcGIS, Python, Bash, HTML

Familiar with: IDL, FORTRAN, C, Java

Geophysical Models

Proficient: Distribution Hydrology Soil and Vegetation Model (DHSVM)

Structure for Unifying Multiple Modeling Alternatives (SUMMA)

Snow Accumulation and Ablation Model (SNOW-17)

Familiar with: The Weather and Research Forecasting (WRF) Model

The Variable Infiltration Capacity (VIC) Model